MT-CWJCR-099-032

GLOBAL – JIP

PHASE II
FINAL REPORT

Submitted by:
Mark Rowe and Stephen Liu

Submitted to:
JIP – Technical Activities Committee
Global Industries, Inc.
Lafayette, Louisiana

December 1999

ABSTRACT

Underwater wet welding with covered electrodes has proven to be a valuable repair technique on offshore platforms, piers, ships, and nuclear power plants. Wet welding is selected over other repair options because it can be quickly mobilized with relatively simple equipment, thereby dramatically reducing repair cost and downtime. However, the mechanical properties are not equal to those exhibited by dry welds. Ductility and toughness of wet welds are reduced due to porosity, as well as changes in the chemical composition and microstructure caused by the wet environment.

Due to the profound effect of increasing depth on weld quality, no one electrode formulation can be expected to produce quality wet welds at all depths. The objective of the present investigation is to mitigate the adverse effects of increasing depth by optimizing the ferro-alloy content of a rutile-base shielded metal arc welding electrode at selected test depths. A second, and equally important, objective is to gain a better understanding of the factors which control the quality of underwater wet welds.

The present investigation is organized into three tasks to address the problems associated with increasing underwater depth. Task I involves increasing additions of ferro-manganese to the coating. Weld metal manganese content decreases with depth. The coating ferro-manganese content was increased in an effort to compensate for the loss of manganese with depth. Task II involves addition of titanium and boron to the electrode coatings. Titanium and boron in the proper amounts are known to produce a microstructure high in acicular ferrite. Titanium is a strong deoxidant and should reduce the weld metal oxygen content, which will improve alloying element recovery and increase upper shelf toughness. In Task III, rare earth metals (REM) were added to the

coatings in addition to titanium and boron. REM are strong deoxidants and should reduce weld metal oxygen content. Any porosity that is caused by oxidation should be eliminated by adding strong deoxidants to the weld pool.

Addition of ferro-manganese alone failed to increase the weld metal manganese content due to the strongly oxidizing environment. It was possible to control the weld metal manganese content with addition of a stronger deoxidant, such as titanium, to the system. Addition of REM reduced oxygen content and increased the recoveries of manganese and boron in preliminary tests at a depth of 1.5 ft (0.5 m), but high oxygen contents and low recoveries were observed at greater depths. Addition of REM increased the exposure of the weld pool to oxygen and hydrogen at greater depths. Titanium was more effective than manganese or REM as a deoxidant.

Porosity decreased with increasing ferro-manganese addition, and increased with increasing additions of titanium, boron, and REM. One possible explanation is the effect of slag basicity on absorption of hydrogen into the weld pool, which determines the amount of hydrogen available to form porosity. Chemical analysis of selected slag samples revealed that porosity levels decreased with increasing slag basicity.

The fraction of acicular ferrite (AF) in the as-deposited microstructure was significantly increased through titanium-boron additions in Task II (60-80% AF) over Task I with only ferro-manganese additions (10-20% AF). Microstructures high in acicular ferrite were also produced with formulations containing titanium, boron, and REM additions in Task III.

Significant microstructural refinement was observed in the reheated weld metal as a result of titanium-boron additions. Yield strength exhibited a good correlation with the average ferrite grain size in the reheated weld metal, indicating that reheated weld metal microstructure has a significant influence on the mechanical properties of wet welds.

Titanium-boron additions did not significantly improve Charpy impact toughness values. Upper shelf toughness values for underwater wet welds are most likely determined by defect concentration rather than microstructure. Welds with REM

additions exhibited low toughness values due to higher porosity levels.

The present investigation has demonstrated that ferro-alloy additions to the coatings of SMAW electrodes can effectively control the chemical composition and microstructure of underwater wet welds to a depth of 300 ft (91 m). Interactions between coating additions and weld metal porosity content were also observed, and attributed to variations in slag basicity. The possible relationship between slag basicity and the transfer of hydrogen and oxygen to the weld pool is a topic worthy of further research.

TABLE OF CONTENTS

Page

LIST OF FIGURES

Page

LIST OF TABLES

Page

1 INTRODUCTION

Underwater wet welding with covered electrodes has proven to be a valuable repair process on offshore platforms, piers, ships, and nuclear power plants. Wet welding is selected over other repair options because it can be quickly mobilized with relatively simple equipment, thereby dramatically reducing repair cost and downtime. In the case of offshore platforms and piers, the only way to create a dry environment is to construct an enclosure around the repair and expel the water with pressurized gas, which is known as dry hyperbaric welding. On offshore platforms, repairs made by wet welding require half the time and cost of repairs made with dry hyperbaric welding (Grubbs and Reynolds 1999) (Couch 1997), and require less maintenance than mechanical clamps (Couch 1997). Wet welded repairs on ships save the cost and downtime associated with dry docking (Blackledge 1998). Wet welding has been used in nuclear power plants to make repairs in the reactor pressure vessel (Childs 1991). Wet welding is being used increasingly as an underwater repair technique due to research and development in recent years leading to improved weld quality.

Although the quality of wet welds has improved, the mechanical properties are still not equal to those exhibited by dry welds. There is an increased occurrence of defects, such as porosity and inclusions. Ductility and toughness are not equal to those of dry welds due to porosity as well as changes in the chemical composition and microstructure caused by the wet environment.

Due to the profound effect of increased pressure on weld quality, no one electrode formulation can be expected to produce quality wet welds at all depths. The objective of the present investigation is to improve the quality of wet welds by optimization of the ferro-alloy content of the electrode coating for given depths. The addition certain alloying

elements will counter the oxidizing effects of the water, allowing better control over the oxygen content, alloy element content, and microstructure. By adding increasingly stronger deoxidants to the weld pool, any porosity that is caused by oxidation will be eliminated. An organized, stepwise approach to coating formulation was selected so that the influence of each individual ingredient could be understood.

2 LITERATURE REVIEW

2.1 Effect of The Underwater Environment

When water vapor is exposed to high temperatures in the welding arc, it decomposes into oxygen and hydrogen which dissolve into the weld pool. As molten iron cools, the solubility of oxygen and hydrogen decrease. Oxygen can come out of solution in the form of solid or liquid oxide inclusions, or gases, which can cause porosity. Hydrogen can form pores of molecular hydrogen, react with oxygen to form water vapor, or cause embrittlement and cracking after the metal cools. As underwater depth increases, the hydrostatic pressure increases at a rate of one atmosphere for every 33 ft (10 m). For a given mole fraction, the partial pressure of a gas increases as the total pressure increases. Therefore, for a constant composition of gases in the arc atmosphere, the activities of oxygen and hydrogen above the weld pool increase with depth. The result is a change in chemical composition, microstructure, and porosity content of the weld metal with depth.

2.1.1 Effect of Depth on Chemical Composition.

Elements with an affinity for oxygen are increasingly partitioned from the weld metal to the slag and oxide inclusions with depth. Ibarra et al (1987) have shown that the concentrations of manganese and silicon in the weld metal decrease with depth. It was also shown that the weld metal oxygen content increases with depth. The data from

Ibarra et al is presented in Figures 1 and 2. Snyder and Pense (1982) found that the volume percent of oxide inclusions in weld metal increases with weld metal oxygen content, as seen in Figure 3; therefore, it can be concluded that oxide inclusion content of underwater wet welds increases with depth. The net effect of increasing depth is a decrease in hardenability due to decreasing alloy element content and increasing oxygen content.

2.1.2 Porosity

Porosity in underwater wet welds increases dramatically with depth. According to Suga and Hasui (1986), porosity begins to appear in wet welds at depths greater than 15 ft (4.6 m) and exceeds five pct. at about 150 ft (46 m), as shown in Figure 4. The maximum amount of porosity allowed for an AWS D3.6 Class B weld is five pct.; therefore, it becomes increasingly challenging to meet the Class B specification at greater depths. Class B welds are suitable for limited structural applications.

The composition of the gas contained in underwater wet weld porosity has been analyzed and reported in the literature. Suga and Hasui (1986) found that the composition of gas contained in wet weld porosity is 96 pct. hydrogen with a small amount of carbon monoxide. Ando and Asahina (1983) also analyzed the gas contained within the porosity of underwater wet welds. Deposits from iron oxide/ iron powder, high titanium oxide, and ilmenite electrodes were tested at three different depths. The results of the analyses showed that in all cases the gas composition in the pores was greater than 99 pct. hydrogen. Based on the work of Suga and Hasui, and Ando and Asahina, it can be concluded that porosity in underwater wet welds is caused by hydrogen.

The formation of porosity in underwater wet welds by concentration of hydrogen ahead of the solidification front was modeled by Suga (1987). Several important conclusions were reached from the model developed by Suga:

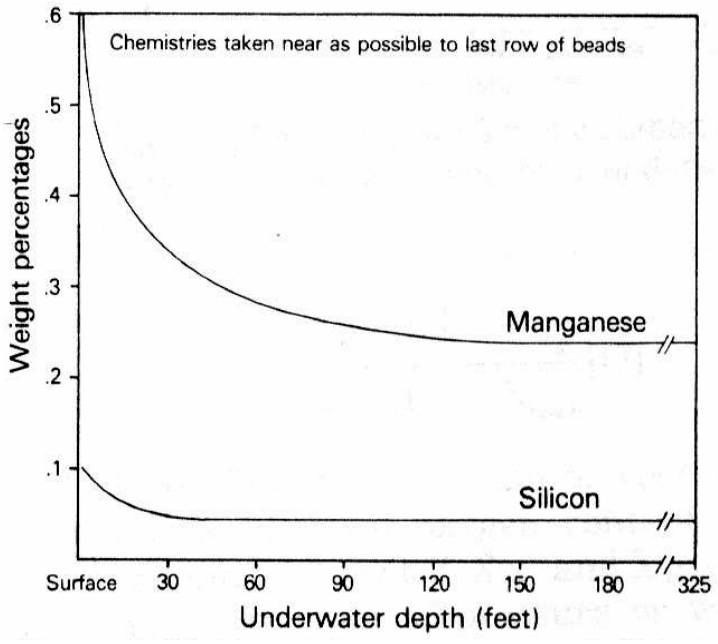

Figure 1: Effect of underwater depth on weld metal composition. (Ibarra et al 1987).

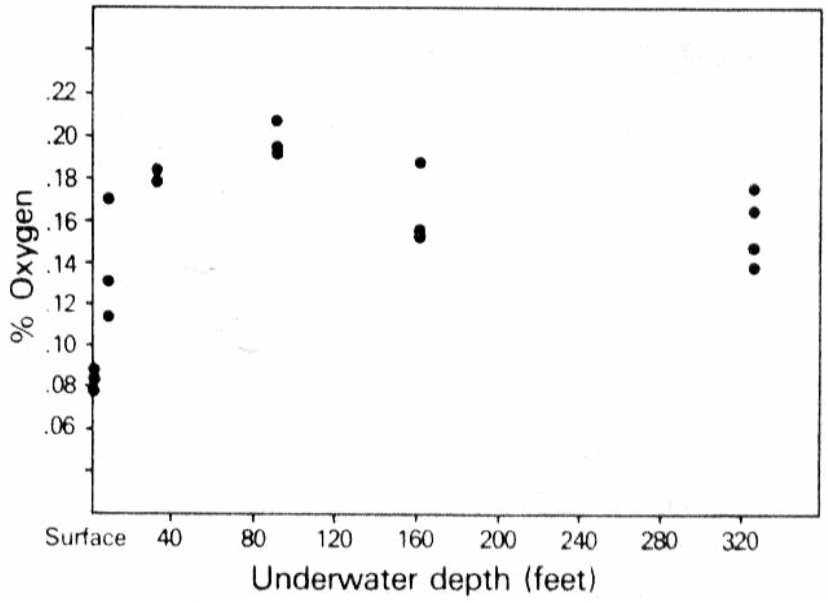

Figure 2: Effect of underwater depth on weld metal oxygen content (Ibarra et al 1987)

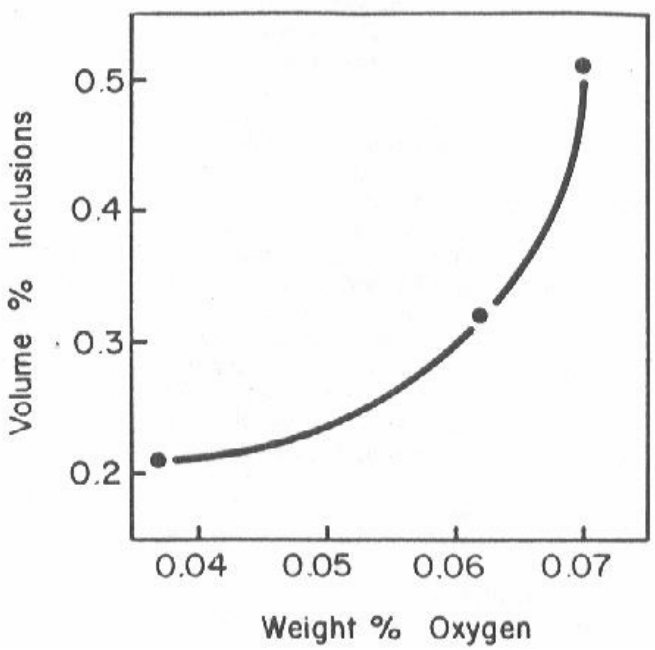

Figure 3: Effect of weld metal oxygen content on volume percent oxide inclusions (Snyder and Pense 1982)

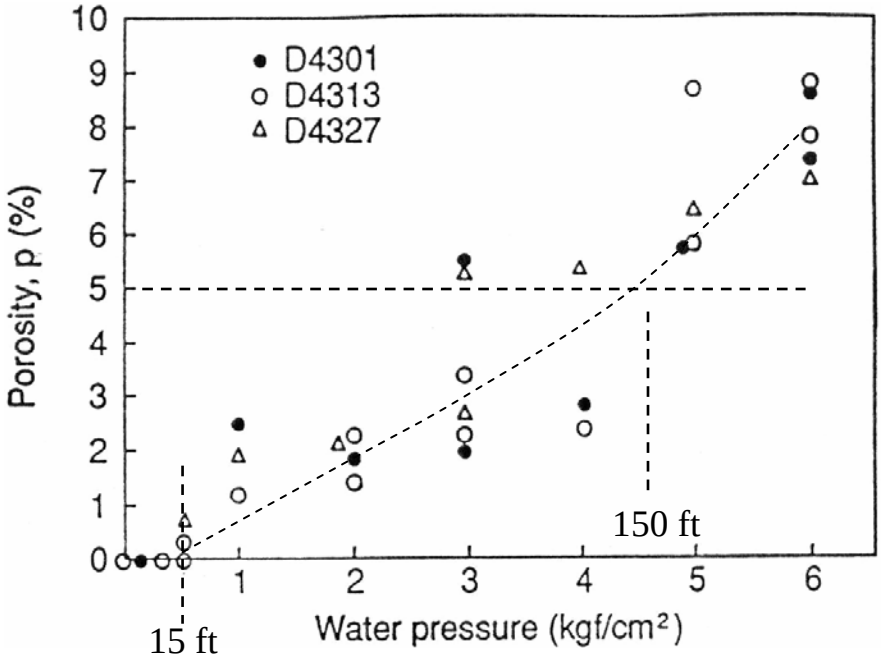

Figure 4: Effect of underwater depth on porosity. (Suga and Hasui 1986)

1. The growth rate of the gas bubble increases and the critical radius decreases with an increasing initial concentration of hydrogen and with a decreasing solidification speed.

2. The growth rate of the gas bubble decreases with pressure for a large bubble but increases with pressure for a small bubble. Thus, the critical radius of the gas bubble decreases with an increasing pressure.

3. The contour of the pore changes from “closed type”, to “cylindrical type”, to “cup type (bubbling type)” as the initial concentration of hydrogen increases, or solidification speed decreases.

The critical radius is the minimum size at which a pore is stable. A smaller critical radius means that pores can nucleate more easily. Suga predicted that the critical radius for pore formation decreases with increasing pressure, which is consistent with the observed increase in porosity content with depth. The model also predicts the change in pore shape which is observed with increasing depth (higher initial concentration of hydrogen). In addition, the model predicts that higher welding travel speeds should reduce porosity, which has yet to be demonstrated experimentally for wet welding.

Other mechanisms for pore formation have been proposed. Based on thermodynamic calculations, Liu et al (1994) proposed that oxygen can react with carbon to produce carbon monoxide porosity, and that oxygen can also react with hydrogen to produce steam porosity in underwater wet welds. Liu et al (1994) went on to suggest that steam in the pores can react with the surrounding iron to form iron oxide and hydrogen, thus explaining the presence of hydrogen, and not water vapor, in the pores. Liu et al (1994) concluded that if the weld pool were sufficiently deoxidized, porosity due to both

carbon monoxide and steam could be prevented.

Based on the assumption that porosity in underwater wet welds is caused by hydrogen, techniques to reduce the hydrogen content of wet welds should also be effective at reducing porosity. Increasing the calcium carbonate content of a rutile-base electrode coating has been shown to reduce porosity in wet welds. Sanchez-Osio et al (1995) increased calcium carbonate from 9 to 12.5 pct., which decreased porosity from 2.2 to 1.0 pct. at a depth of 30 ft (9 m). Carbonates decompose to form carbon dioxide and carbon monoxide in the arc, reducing the partial pressure of hydrogen, and thus reducing the amount of hydrogen absorbed into the weld pool.

In addition to carbonate content, it has been shown that slag basicity can influence the hydrogen content of weld metal. Figure 5 presents data from steelmaking literature (Turkdogan 1983) on the effect of slag basicity on the solubility of water vapor in slags. In many slag systems there is a minimum in water vapor solubility near neutral basicity. Water vapor dissolves in slags according to equation [2.1] in acid melts, and equation [2.2] in basic melts (Turkdogan 1983).

$$(\geqq Si\text{-}O\text{-}Si\leqq) + H_2O = 2(\geqq Si\text{-}OH) \qquad [2.1]$$

$$(O^{2-}) + H_2O = 2(OH^-) \qquad [2.2]$$

Equation [2.1] represents the breakdown of silicate networks by hydroxyl ions in an acid slag. Equation [2.2] represents the reaction of water vapor with free oxygen ions in a basic slag. In a slag of neutral basicity, neither of the above mechanisms is favored, and the solubility of water vapor in the slag is minimized.

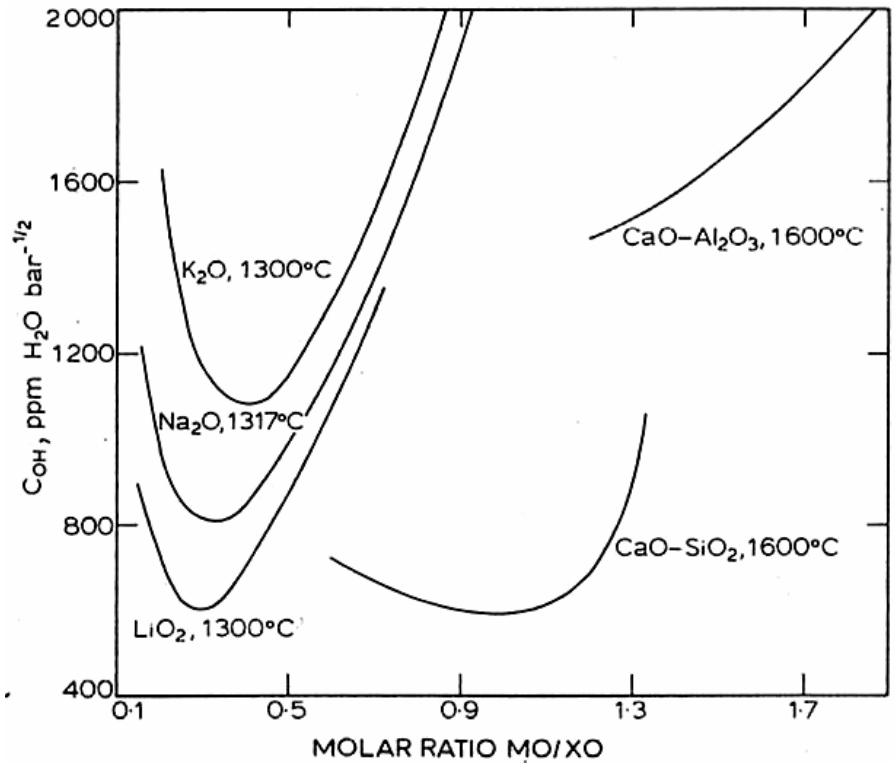

Figure 5: Water vapor solubility (C_{OH}) as a function of slag basicity (increasing basicity to the right) (Turkdogan 1983).

Medeiros (1997) demonstrated that the weld metal hydrogen pickup in underwater wet welding is strongly dependent on water vapor solubility in slags. In welding literature, Terashima and Tsuboi (1982) have shown that increasing slag basicity in a $CaO\text{-}MgO\text{-}Al_2O_3\text{-}SiO_2$ submerged arc welding flux reduces weld metal hydrogen, as seen in Figure 6. Surian (1997) and De Rissone et al (1997) have shown that increasing the slag basicity of rutile-base SMAW electrodes results in lower diffusible hydrogen for similar moisture contents, as seen in Figure 7. Medeiros and Liu (1998) have shown that the diffusible hydrogen content of underwater wet welds goes through a minimum with increasing additions of hematite to an acid electrode coating, as seen in Figure 8. Hematite decomposes to form FeO in the slag, thus increasing slag basicity. Medeiros and Liu noted a similar trend for total hydrogen (diffusible plus residual). If porosity in wet welds is caused by hydrogen and weld metal hydrogen is affected by slag basicity, it can be expected that slag basicity will affect the amount of porosity in underwater wet welds.

2.1.3 Effect of Depth on Microstructure

Ibarra et al (1987) found that weld metal oxygen increases with depth up to about 2000 ppm at 100 ft (30 m) and remains high at greater depths. Weld metal manganese levels were shown to drop significantly from 0.6 to 0.25 wt pct. between 0 and 100 ft due to increased oxidation, then remain fairly constant at greater depths (Ibarra et al 1987). The loss of alloying elements with depth alters the microstructure and causes decreased strength and toughness. The microstructure of wet welds consists mainly of coarse primary ferrite (PF) and ferrite with aligned carbides (FS) (Ibarra 1987). In contrast, surface welds frequently contain large fractions of acicular ferrite, which is preferred due to the resistance of acicular ferrite to cleavage fracture. Addition of titanium and boron to wet welding electrodes has been shown to produce up to sixty pct. acicular ferrite in

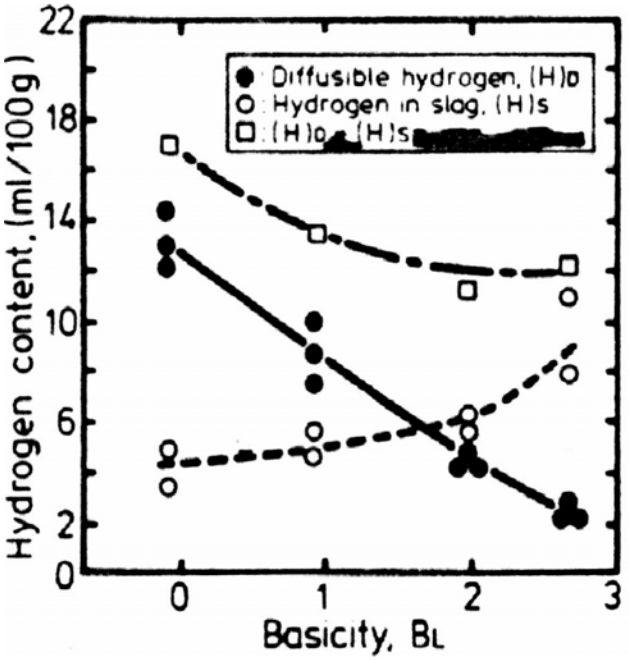

Figure 6: Effect of slag basicity on diffusible hydrogen and slag hydrogen content. (Terashima and Tsuboi 1982).

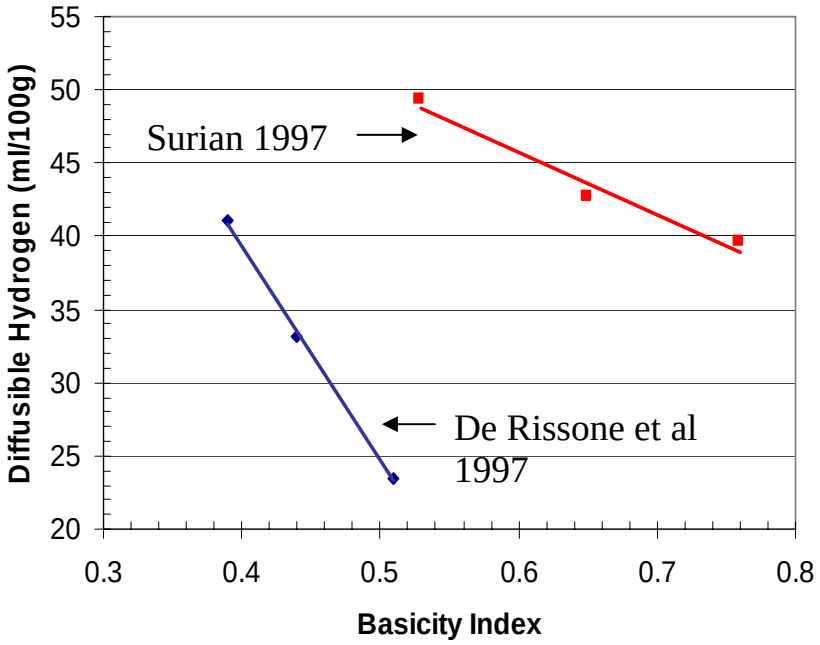

Figure 7: Diffusible hydrogen as a function of slag basicity for a rutile-base electrode deposited in air.

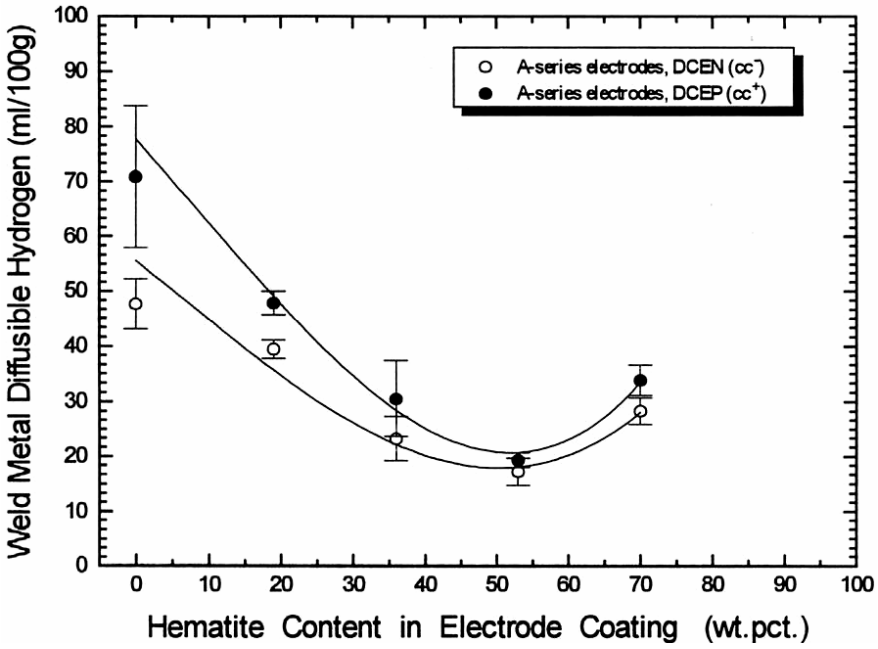

Figure 8: Diffusible hydrogen in underwater wet welds as a function of hematite content of the electrode coating. (Medeiros and Liu 1998).

the microstructure at a depth of 30 ft (9 m) (Sanchez-Osio 1995). It is not known if a microstructure high in acicular ferrite can be produced at greater depths or if microstructural refinement can increase the toughness of underwater wet welds.

2.1.4 Effect of Depth on Mechanical Properties

A comprehensive review of underwater welding literature revealed data on the effect of depth on mechanical properties of wet welds, presented in Table 1. Few investigations have focused on the effect of increasing depth on mechanical properties. The effect of depth on tensile strength and Charpy toughness are presented in Figures 9 and 10. Each set of data points corresponds to welds made with the same type of SMA welding electrode. Tensile strength and toughness decrease in an approximately linear function with depth to 330 ft (101 m). Changes in microstructure, chemical composition, and porosity undoubtedly contribute to the decline in mechanical properties; however, it is not known which factor, if any, is most influential.

2.2 Effect of Alloying Elements on Weld Metal Microstructure and Properties

2.2.1 Effect of Manganese

Increasing the manganese content of low carbon-manganese steel weld metal results in microstructural refinement through an increase in hardenability. Evans (1980) found that increasing the manganese content from 0.65 to 1.8 wt. pct. increased the fraction of acicular ferrite in the as-deposited microstructure, and refined the reheated weld metal microstructure. Surian and Boniszewski (1992) found that increasing the manganese content from 1.45 to 1.7 wt. pct. increased the acicular ferrite content of the as-deposited weld metal; however, no change in the reheated weld metal was noted. Chaveriat et al (1987) investigated manganese contents from 1.0 to 1.7 wt. pct., and

Table 1: Chemical Composition and Mechanical Properties of Steel Wet Welds as a Function of Depth, Reported in the Literature.

Reference	Depth	C	Mn	Other Element		Cross tensile		Weld Metal Tensile			Weld Metal Hard-ness	Charpy Impact Tough-ness @ 28-32 F
	(ft.)	wt. pct.	wt. pct.		wt. pct.	Y.S. (ksi)	Ult. (ksi)	Ult. (ksi)	elong. (pct.)	max (HV)		(ft-lb)
Pope 1997	3	0.05	0.03	Ni	2.00	--	68	--	--	--		37
Szel. 1998	20	--	--	--	--	--	--	83	--	235		33
Grubbs 1998	20	--	--	--	--	--	73	77	13.5	--		31-37
Grubbs 1998	33	--	--	--	--	--	72	74	12	--		32
Pope 1997	40	0.03	0.02	Ni	2.00	--	64	--	--	--		26
Pope 1997	66	0.04	0.02	Ni	2.00	--	65	--	--	--		24
Grubbs 1998	165	--	--	--	--	--	66	63	10	--		23-25
Szel. 1992	181	0.16	0.46	Si	0.42	--	64	--	--	185		21
Szel. 1992	181	0.20	0.18	Si	0.06	--	62	70	--	263		18
Szel. 1992	181	0.15	0.20	Si	0.14	--	56	53	--	236		18
Szel. 1992	181	0.26	0.37	Si	0.27	--	--	60	--	207		24
Szel. 1992	181	0.18	0.33	Si	0.29	--	--	67	--	263		24
Szel. 1998	182	--	--	--	--	--	--	76	--	230		22
Szel. 1990	182	0.27	0.30	Si	0.09	55	60	--	--	228		20
Szel. 1990	182	0.17	0.33	Si	0.11	55	79	--	--	232		18
Szel. 1990	182	0.20	0.48	Si	0.25	53	53	--	--	246		18
Szel. 1990	182	0.21	0.46	Si	0.15	55	69	--	--	286		18
Szel. 1992	201	0.33	0.22	Si	0.11	--	66	63	--	222		15
Szel. 1992	201	0.34	0.29	Si	0.21	--	60	52	--	295		18
Szel. 1992	201	0.27	0.26	Si	0.10	--	64	61	--	252		15
Szel. 1992	201	0.27	0.31	Si	0.18	--	64	53	--	196		16
Szel. 1992	201	0.28	0.23	Si	0.11	--	61	72	--	190		18
Grubbs 1998	325	--	--	--	--	--	62	59	7	--		16-18
Szel. 1998	330	--	--	--	--	--	--	65	--	230		15
Szel. 1990	330	0.13	0.22	Si	0.06	--	--	--	--	226		14
Szel. 1990	330	0.09	0.23	Si	0.06	--	--	--	--	213		20
Szel. 1990	330	0.11	0.50	Si	0.27	--	--	--	--	293		12
Szel. 1990	330	0.12	0.31	Si	0.10	--	--	--	--	245		18

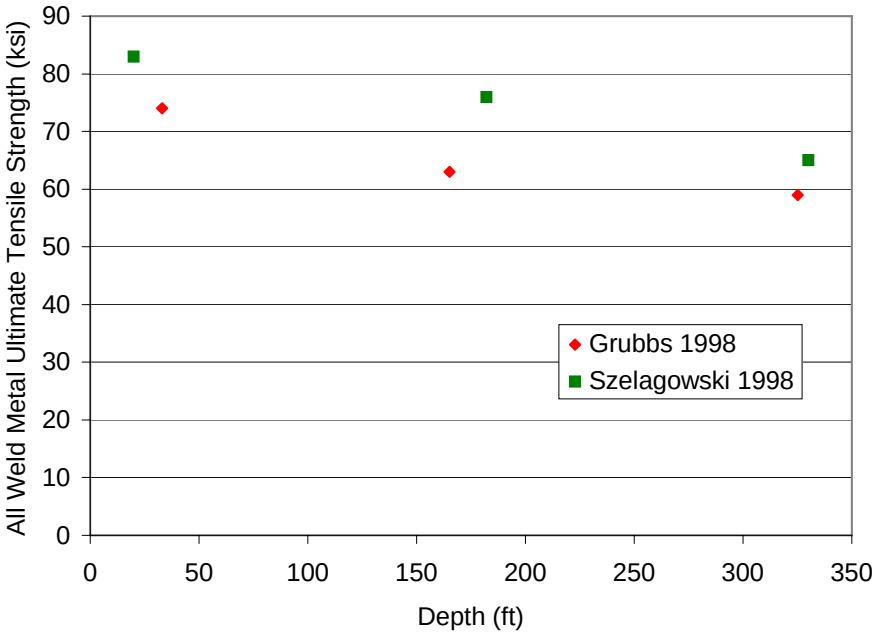

Figure 9: Tensile strength as a function of underwater depth reported in the literature.

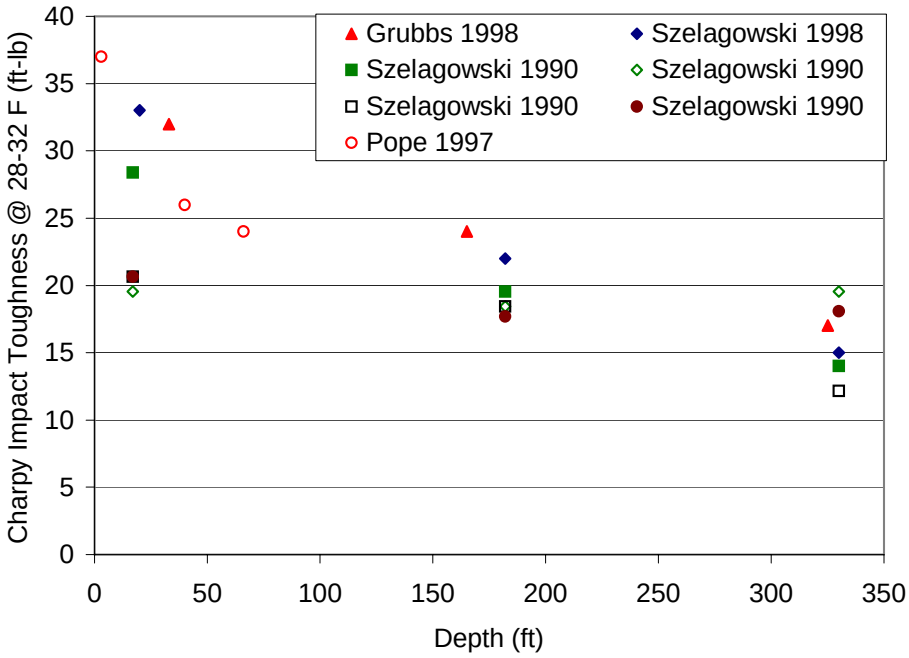

Figure 10: Charpy impact toughness as a function of underwater depth reported in the literature.

observed increasing acicular ferrite with increasing manganese content. Pokhodnya et al (1986) found that a minimum manganese content of 1.0 wt. pct. was necessary for the intragranular nucleation of acicular ferrite. Evans (1993) also noted that a minimum manganese content is necessary for the formation of acicular ferrite in titanium micro-alloyed deposits. The maximum amount of acicular ferrite possible at 0.65 pct. manganese was 35 wt. pct.; however, when the manganese content was increased to 1.8 pct., it was possible to produce up to 70 pct. acicular ferrite.

Manganese contents of underwater wet welds are typically less than 0.5 wt. pct., as seen in Table 1. It can be concluded from the literature that increasing the manganese content will lead to promotion of acicular ferrite in the as-deposited microstructure and refinement in the reheated microstructure by increasing the hardenability.

2.2.2 Effect of Titanium and Boron

Several investigations have shown that it is possible to produce weld metal microstructures high in acicular ferrite by micro-alloying with titanium and boron. Evans (1993, 1992) has shown that it is possible to produce up to 70 pct. acicular ferrite through the addition of titanium alone. Tsuboi and Terashima (1983) reported that when titanium and boron are added together there is an interactive effect which enhances acicular ferrite formation. Titanium protects boron from reacting with oxygen and nitrogen, and forms fine intragranular inclusions of titanium oxide and nitride. Boron is then free to diffuse to austenite grain boundaries, where it reduces the grain boundary energy, and retards the formation of grain boundary ferrite. Finally, the titanium-rich intragranular inclusions provide nucleation sites for acicular ferrite.

Oh et al (1990) demonstrated that microstructures containing greater than 90 pct. acicular ferrite can be produced with 40-45 ppm boron and 400-500 ppm titanium in submerged arc weld metal. Evans (1996) produced up to 85 pct. acicular ferrite with 40 ppm boron and 400 ppm titanium in shielded metal arc weld metal. Sanchez-Osio et al

(1995) found that up to 60 pct. acicular ferrite could be produced in underwater wet welds with a weld metal composition of 10 to 20 ppm boron and 250 to 300 ppm titanium at a depth of 30 ft (9 m). Sanchez-Osio explained the difference in optimum titanium and boron content between wet and dry welds in terms of the higher cooling rate of underwater wet welds. Even though addition of titanium and boron to wet welds has been shown to produce a microstructure high in acicular ferrite at a depth of 30 ft, it is not known if titanium and boron will be effective at producing acicular ferrite at greater depths, where oxidation of the weld pool is more significant.

2.2.3 Effect of Rare Earth Metal Additions

It has been reported in the literature that rare earth metal (REM) additions can reduce the oxygen content of weld metal and improve toughness. REM are some of the strongest deoxidants of all the elements. The thermodynamic stability of REM oxides can be compared to other metal oxides using the Ellingham diagrams in Figure 11 (Efimenko and Kalin 1978). The diagram at bottom shows REM in the cross-hatched area compared to titanium and manganese oxides, pointed out by the arrows. It can be seen that REM form more stable oxides than titanium or manganese. The diagrams at top show a detailed view of the REM region at temperatures representative of the weld pool and droplet transfer stages. The REM oxides retain their stability at high temperatures, and therefore should be effective deoxidants in the weld pool and during droplet transfer.

Slutskaya et al (1978) reported that addition of REM (Cerium and Yttrium) to welding consumables increases the recovery of alloying elements, refines the grain size of the deposit, and improves toughness. Efimenko (1980) found that there was a maximum in room temperature toughness with an addition of 0.2 to 0.4 pct. metallic REM (yttrium) to the coating of welding electrodes. Efimenko also added oxides of REM to the electrode coating and noted an improvement in mechanical properties, but not to the same extent as with metallic REM. An improvement in arc stability and slag

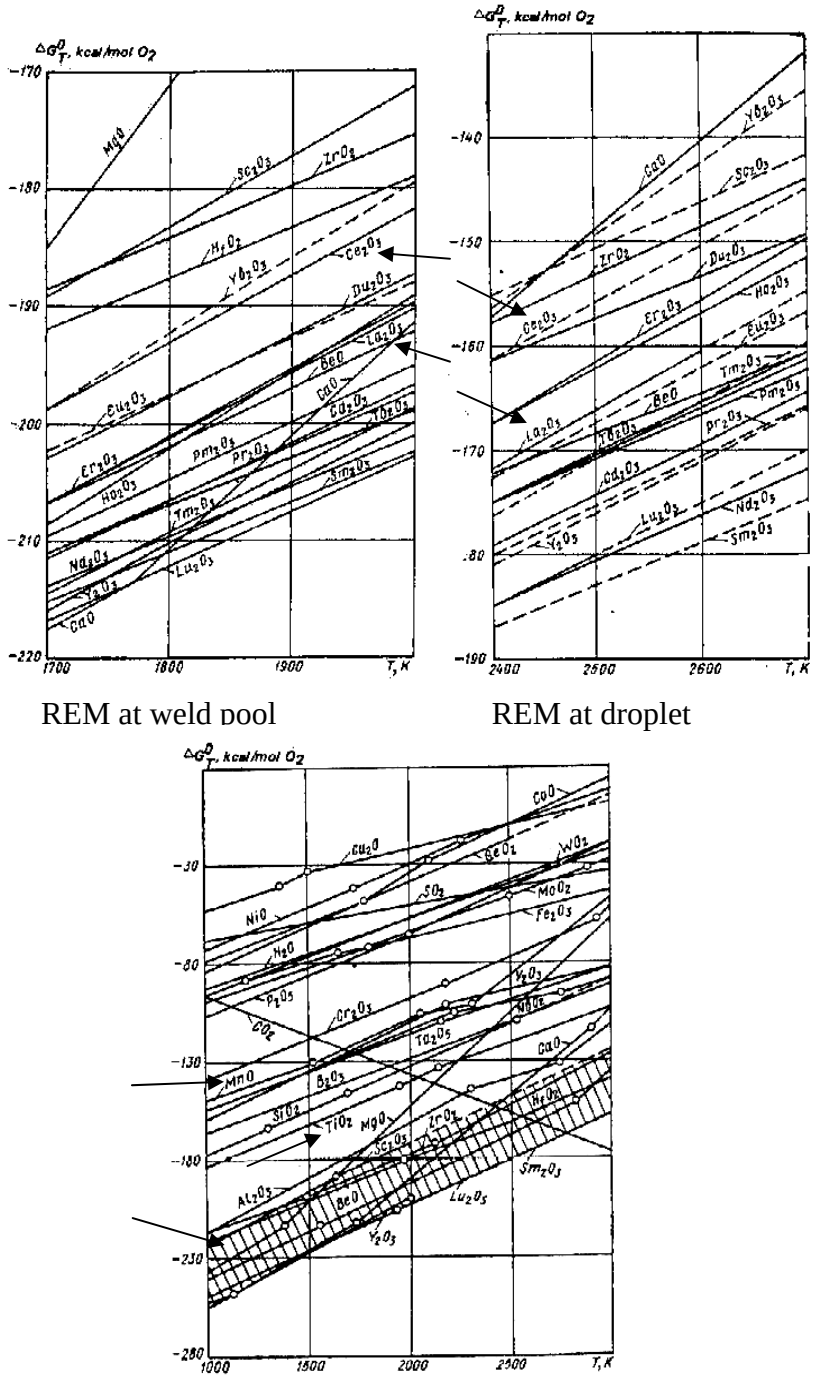

Figure 11: Ellingham diagrams showing the relative thermodynamic stability of the REM oxides compared to other metal oxides. (Efimenko and Kalin 1978)

detachability was also observed by Efimenko with the REM additions. Shiliang et al (1986) observed an improvement in toughness with the addition of metallic REM (yttrium). In contrast to the findings of Efimenko, the improvement was only seen at low temperatures (-40 C), not at room temperature. Shiliang et al showed that addition of REM led to a decrease in the area density and area percentage of oxide inclusions, thereby resulting in improved toughness.

Koukabi et al (1978) investigated the addition of metallic REM (cerium) in submerged-arc welding. A reduction in oxygen content and improvement in impact properties (reduced transition temperature and increased upper shelf toughness) was observed with cerium addition. Reduced oxygen content is expected to result in improved upper shelf toughness, as was reported by the Efimenko and Koukabi et al. The findings of Shiliang et al that upper shelf toughness did not improve, even though the weld metal oxygen was reduced with REM additions, are inconsistent with the findings of other investigators.

Addition of REM to underwater wet welds should improve control over chemical composition by improving recovery of alloying elements. A reduction in oxygen content of wet welds should be beneficial to upper shelf toughness.

2.2.4 Effect of Weld Metal Microstructure on Toughness.

Toughness is a measure of the energy required to fracture a material. Brittle materials have low toughness and are sensitive to the presence of flaws. A material with high toughness can tolerate occasional stresses above the yield stress and the stress concentrations caused by flaws without fracturing. Underwater wet welds contain many flaws, such as pores, oxide inclusions, and micro-cracks; therefore, high toughness is a desirable property for wet welds.

Steels undergo a transition from ductile failure (high toughness) to brittle fracture (low toughness) as the temperature decreases. The transition temperature can vary

widely depending on microstructure and chemical composition. The Charpy test is useful for determining if a material is likely to fail in a ductile or brittle fashion. If the Charpy test is conducted over a range of temperatures, the upper shelf toughness (ductile failure), lower shelf toughness (brittle failure), and the transition temperature can be determined. The transition temperature is usually the most important parameter. A material with a lower transition temperature will be less likely to fail in a brittle manner. Once it is determined that the material will not fail in a brittle manner, a high upper shelf toughness is desirable to maximize the amount of energy required to propagate a crack through the material.

Several authors have presented data on the influence of weld metal microstructure on mechanical properties. Snyder and Pense (1982) found that decreasing the fraction of primary ferrite, and thus increasing the fraction of acicular ferrite, improved room temperature toughness, as seen in Figure 12. Evans (1980) found that the effect of increasing acicular ferrite content by manganese addition was to lower the Charpy transition temperature, but the upper shelf toughness was maximized at the lowest manganese addition and lowest acicular ferrite content. Evans (1996) produced microstructures of up to 85 pct. acicular ferrite by the addition of titanium and boron. The highest acicular ferrite contents had the lowest transition temperature, but not necessarily the best upper shelf toughness. Zhang and Farrar (1997) varied the microstructure of weld metal by adding manganese and nickel, and found that the best toughness was associated with a microstructure of 50 to 75 pct. acicular ferrite with grain boundary pro-eutectoid ferrite.

It can be concluded that a microstructure high in acicular ferrite will produce a low Charpy transition temperature, but may not produce the highest upper shelf toughness. Increasing the acicular ferrite content of underwater wet welds should increase the resistance to cleavage fracture through microstructural refinement.

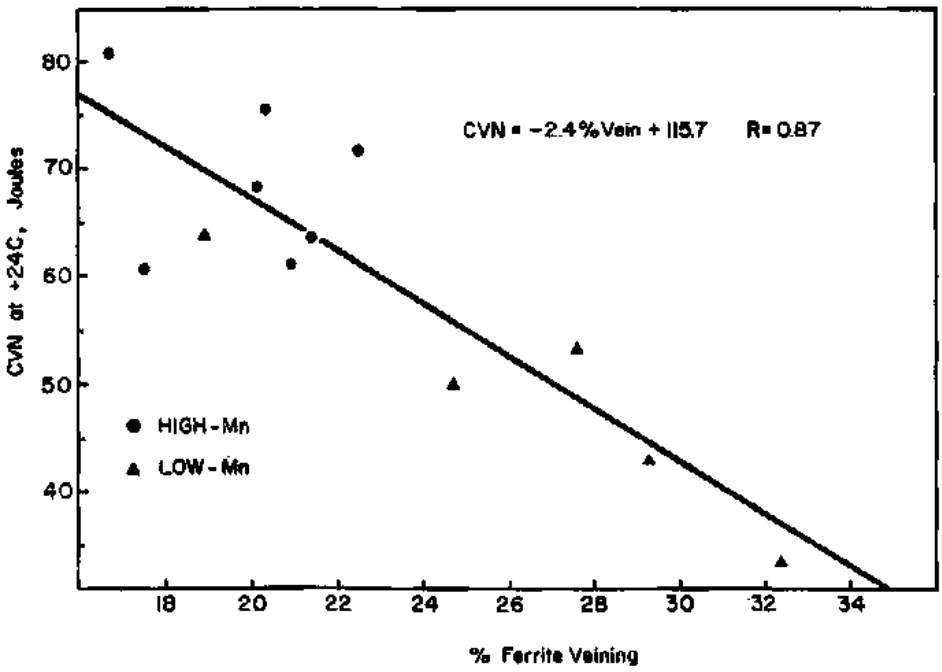

Figure 12: Effect of primary ferrite content (pct. ferrite veining) on toughness (Snyder and Pense 1982).

2.2.5 Effect of Weld Metal Oxygen Content on Toughness.

The effect of oxygen content on weld metal impact toughness can be seen in Figures 13 and 14. Upper shelf toughness decreases as oxygen content increases. Fracture in the upper shelf region occurs by ductile void coalescence. The voids nucleate at oxide inclusions, and it is known that the oxide inclusion content increases with weld metal oxygen content, as shown in Figure 3. In the case of low oxygen content, the voids are fewer and larger, thus, more energy is absorbed in plastic deformation than in the case of many small voids. The oxygen content of underwater wet welds is typically in excess of 1000 ppm; therefore, lowering the oxygen content of wet welds should increase upper shelf toughness.

The Charpy transition temperature goes through a minimum at intermediate oxygen levels, as seen in Figure 14. Onsoien et al (1996) reported that a minimum level of oxygen is necessary to form a microstructure high in acicular ferrite. The minimum in the transition temperature vs. oxygen plot is caused by the promotion of acicular ferrite in the microstructure. High levels of oxygen are detrimental because large oxide inclusions can act as cleavage nucleation sites.

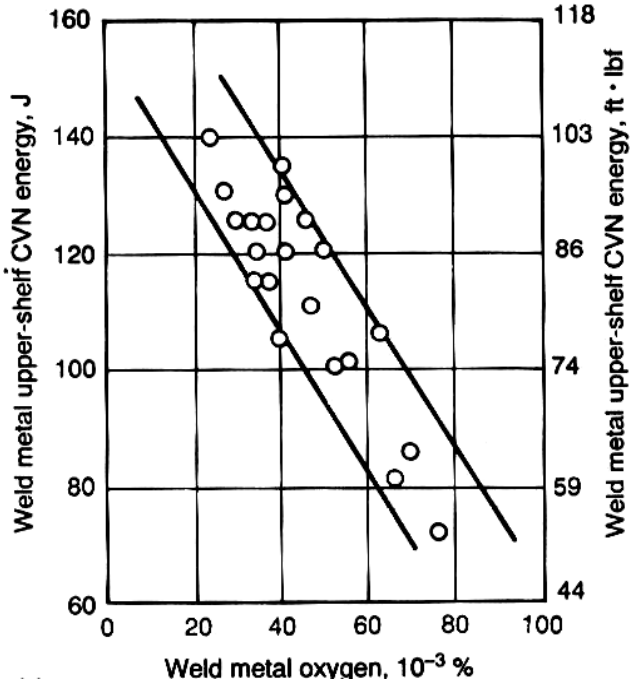

Figure 13: Weld metal upper shelf toughness as a function of weld metal oxygen content. (Ahlblom 1984).

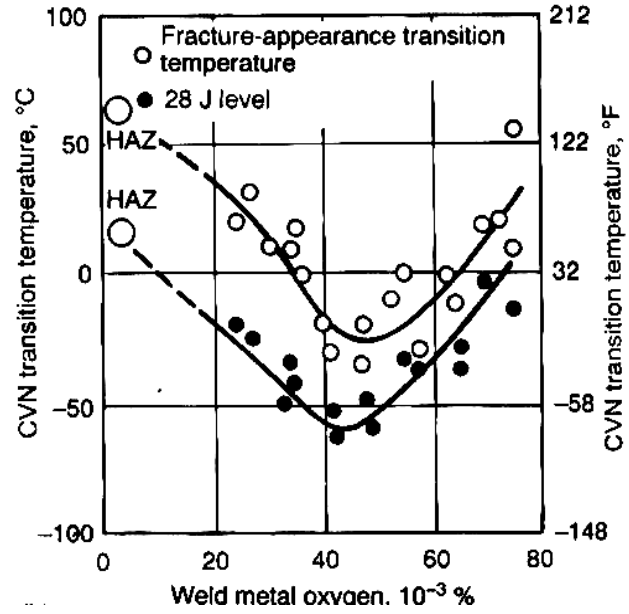

Figure 14: Charpy transition temperature as a function of weld metal oxygen content. (Ahlblom 1984).

3 STATEMENT OF PROBLEMS AND OBJECTIVES

From the literature cited in the introduction and in section 2.1, it is clear that underwater wet welding has the potential to greatly reduce the cost and downtime associated with underwater repair and fabrication over other options, but the quality of wet welds is adversely affected by the underwater environment. As underwater depth increases, changes in chemical composition, microstructure, and porosity content cause mechanical properties to decline. The objective of the present investigation is to mitigate the adverse effects of increasing depth by optimizing the ferro-alloy content of a rutile-base shielded metal arc welding electrode. A second, and equally important, objective is to gain a better understanding of the factors which control the quality of underwater wet welds.

The present investigation is organized into three tasks to address the problems associated with increasing underwater depth:

Task I: Increasing manganese addition.

Weld metal manganese content decreases with depth. The coating ferro-manganese content will be increased to compensate for the loss of manganese with depth. Increasing the weld metal manganese content above the levels commonly found in underwater wet welds is expected to promote microstructural refinement, resulting in improved toughness and increased strength.

Task II: Addition of titanium and boron.

Titanium and boron in the proper amounts are known to promote fine acicular ferrite in the microstructure. Titanium is a strong deoxidant and is expected to reduce the weld metal oxygen content, which will improve alloying element recovery and increase upper shelf toughness.

Task III: Addition of rare earth metals (REM).

REM are strong deoxidants and should reduce weld metal oxygen content. Recovery of alloying elements should increase and upper shelf toughness should improve with a reduction in weld metal oxygen content. Any porosity that is caused by oxidation should be eliminated by adding strong deoxidants to the weld pool.

4 EXPERIMENTAL PROCEDURES

4.1 Electrode Coating Formulation.

4.1.1 Task I: Manganese Addition.

To determine the amount of Fe-Mn to add to the coating, it was necessary to find the recovery rate of manganese as a function of depth. An electrode formulation (LC-2) which was developed in Phase I of the JIP program was used as the baseline formulation*. Test welds were made at the four test depths of 70, 140, 200, and 300 ft (21, 43, 61, 91 m). The manganese recovery at each depth was calculated by dividing the weight percent weld metal manganese content by the Fe-Mn addition to the coating. The result was then used to calculate the manganese addition necessary to produce a weld metal manganese content of 0.5 wt. pct. at each depth. Ferro-manganese additions of +/- 1 wt. pct. from the calculated value were used to complete the matrix of three levels of Fe-Mn addition at each depth. The Fe-Mn addition was made at the expense of rutile, feldspar, and mica in the coating to avoid changing the nature of the slag system. The test matrix and baseline formulation are listed in Table 2.

One formulation at each depth was selected for the production of V-groove welds for mechanical testing. The selection was based on porosity content and bead appearance. Another batch of each selected formulation was extruded in order to produce the V-groove welds.

Table 2: Task I Test Matrix.

Formulation*	Depth (ft)	Fe-Mn (wt. pct.)
1F1	70	12.5
1F2	70	13.5
1F3	70	14.5
2F1	140	13
2F2	140	14.5
2F3	140	16
3F1	200	14
3F2	200	15
3F3	200	16
4F1	300	14
4F2	300	16
4F3	300	16

*Baseline formulation (LC2): 46.5% Rutile, 4.4% quartz, 1.5% iron powder, 6% sodium feldspar, 2% kaolin, 3.5% mica, 6% marflux, 8% zircon, 12% ferro-manganese, 10.1% potassium silicate binder, all ingredients in weight percent.

4.1.2 Task II: Titanium-Boron Addition.

Preliminary steps were necessary to determine the recovery of titanium and boron from the coating to the weld metal in wet welding. Recoveries were initially approximated with data from the thesis of Sanchez-Osio (1994), then four batches of experimental electrodes were produced at CSM. Wet welds were produced at CSM at a depth of 1.5 ft (0.5 m) and evaluated in terms of microstructure and chemical composition. One of the four formulations was selected for further trials. The formulation, referred to as T1B1, was used to produce test welds at 70, 140, 200, and 300 ft (21, 43, 61, 91 m). The data from the T1B1 trial gave recoveries for titanium and boron at the four test depths, and allowed further development of the test matrix.

The preliminary test at CSM, as well as data from Sanchez-Osio, were used to quantify the interactive effect between ferro-titanium addition and the recoveries of manganese and boron. Titanium, being the strongest deoxidant in the system, protects manganese and boron from oxidation, thereby significantly increasing their recoveries to the weld metal significantly. Whenever the ferro-titanium addition to the coating was increased, it was necessary to decrease the ferro-manganese and ferro-boron additions in order to maintain a constant weld metal manganese and boron content. To compensate for the interactive effect, the effect of ferro-titanium addition on the manganese and boron recoveries was determined quantitatively. Recoveries of manganese and boron were plotted as a function of ferro-titanium addition, then a linear regression line was used to extrapolate or interpolate recoveries for ferro-titanium additions which had not yet been tried. Ferro-manganese and ferro-boron additions could then be adjusted to produce a constant weld metal manganese and boron content with increasing ferro-titanium addition.

In the next trial, two additional levels of boron and one increased level of titanium were tested at each depth. The entire remaining test matrix was not formulated at this point because there were only two data points at each depth from which to extrapolate

recoveries, and considering the delicate balance of titanium, boron, and manganese which are required to produce the desired microstructure, it was concluded that an additional iteration would greatly increase the probability of success. Once the twelve experiments were analyzed, there was enough data to complete the test matrix, and the final twenty flux formulations were blended.

Due to the strong effect of titanium addition on the manganese recoveries, it was not possible to use the ferro-manganese additions developed for each depth in Task I. Instead, a weld metal manganese content of 0.6 to 0.7 wt. pct. was selected as the objective, and ferro-manganese additions were adjusted taking the ferro-titanium addition into account to give the desired weld metal manganese content. The weld metal manganese content was selected to give an as-deposited hardness of 200 to 300 HV. Hardness levels in Task I were generally less than 200 HV. A somewhat higher hardness was desirable to increase the strength of the Task II welds over the Task I welds which had rather low tensile strength (71, 65, 53, and 54 ksi). Hardness was limited on the high end by the AWS D3.6 specification, which requires a Class A weld to have a maximum hardness less than 325 HV. It has been reported in the literature that a minimum manganese addition is necessary for the intragranular nucleation of acicular ferrite to occur (Evans 1993). Therefore, the highest weld metal manganese content which would produce an acceptable hardness was selected to produce a high AF content.

The Task II test matrix and recoveries are given in Table 3. Recovery is defined as the alloy content in the weld metal (wt. pct.) divided by the ferro-alloy addition to the coating (wt. pct.) multiplied by 100. The recoveries in Table 3 were calculated from the chemical analyses of the weld metal after the experiments were performed. In some cases, preliminary designations were given to formulations before the matrix was completely developed. Those designations are given in parentheses.

Table 3: Task II Test Matrix and Recoveries

	Fe-Mn		Fe-Ti		Fe-B	
	wt. pct.	Mn recovery (pct.)	wt. pct.	Ti recovery (pct.)	wt. pct.	B recovery (pct.)
1T1B1	14.5	**5.9**	5.0	**0.25**	0.5	**0.38**
1T1B2 (T1B1)	14.5	**5.0**	5.0	**0.62**	0.9	**0.21**
1T1B3	14.5	**6.2**	5.0	**0.30**	1.2	**0.41**
1T2B1	10.5	**5.8**	10.0	**0.17**	0.2	**0.40**
1T2B2(1T2BA)	12.4	**6.7**	10.0	**0.28**	0.4	**0.53**
1T2B3	10.5	**6.4**	10.0	**0.18**	0.6	**0.41**
1T3B1	8.5	**7.7**	15.0	**0.20**	0.2	**0.61**
1T3B2	8.5	**7.8**	15.0	**0.27**	0.4	**0.63**
1T3B3	8.5	**7.8**	15	**0.18**	0.5	**0.58**
2T1B1	16.0	**5.9**	5.0	**0.38**	0.5	**0.44**
2T1B2 (T1B1)	14.5	**4.8**	5.0	**0.66**	0.9	**0.22**
2T1B3	16.0	**6.0**	5.0	**0.30**	1.2	**0.39**
2T2B1	10.6	**6.3**	10.0	**0.72**	0.2	**0.50**
2T2B2 (2T2BA)	13.2	**6.6**	10.0	**0.20**	0.4	**0.54**
2T2B3	10.6	**5.8**	10.0	**0.17**	0.6	**0.33**
2T3B1	12.5	**5.0**	7.5	**0.19**	0.2	**0.30**
2T3B2	12.5	**4.6**	7.5	**0.21**	0.5	**0.28**
2T3B3	12.5	**5.8**	7.5	**0.26**	0.7	**0.40**
3T1B1	15.4	**4.7**	5.0	**0.46**	0.5	**0.23**
3T1B2 (T1B1)	14.5	**4.8**	5.0	**1.60**	0.9	**0.19**
3T1B3	15.4	**4.5**	5.0	**0.23**	1.3	**0.28**
3T2B1	11.3	**4.7**	10.0	**0.28**	0.2	**0.30**
3T2B2 (3T2BA)	13.1	**6.2**	10.0	**0.22**	0.4	**0.50**
3T2B3	11.3	**4.6**	10.0	**0.29**	0.6	**0.28**
3T3B1	12.5	**2.6**	7.5	**0.72**	0.3	**0.28**
3T3B2	12.5	**3.9**	7.5	**0.32**	0.5	**0.24**
3T3B3	12.5	**4.8**	7.5	**0.22**	0.8	**0.29**
4T1B1 (T1B1)	14.5	**4.7**	5	**2.20**	0.85	**0.14**
4T1B2	15	**4.6**	5	**0.48**	1.2	**0.30**
4T1B3	15	**5.1**	5	**0.69**	1.8	**0.26**
4T2B1	13.8	**5.3**	10	**0.21**	0.25	**0.40**
4T2B2 (4T2BA)	13.8	**4.3**	10	**0.13**	0.46	**0.28**
4T2B3	13.8	**7.5**	10	**0.44**	1	**0.30**
4T3B1	15	**3.1**	2.5	**1.30**	0.7	**0.14**
4T3B2	15	**3.8**	2.5	**1.46**	1.4	**0.20**
4T3B3	15	**3.9**	2.5	**0.94**	2.8	**0.27**

One formulation for each depth was selected from the Task II test matrix for the production of V-groove welds. The criteria for the decision were hardness, porosity, and microstructure. First, all formulations which produced excessively hard deposits were eliminated. Maximum hardness is limited to 325 HV according to the AWS D3.6 Specification for Underwater Welding (AWS 1989). Next, the formulations which produced the lowest levels of porosity for a given depth were selected. Finally, among the formulations which produced acceptable hardness and low porosity, the one with the most favorable microstructure was selected. It was not necessary to extrude another batch of electrodes for the V- groove experiments as sufficient leftovers were available from the Task II test welds.

4.1.3 Task III: Rare Earth Metal Addition

An initial level of addition of 0.2 wt. pct. REM to the coating was selected based on the work of Shiliang et al (1986) and Efimenko (1980). Both authors reported an optimum level of addition of 0.2 to 0.3 wt. pct. to the coating. The actual ferro-alloy addition was 0.6 wt. pct. because the alloy used in this investigation contains approximately 30 wt. pct. REM. Two higher levels of addition were selected, and an initial experiment was conducted at CSM to determine the optimum level of addition and the effect of REM addition on recoveries of the other elements. Based on the reduction in weld metal oxygen content, the two higher levels of addition were selected for further trials. The lowest level of addition (0.6 wt. pct. REM) had no effect on weld metal oxygen, and was eliminated. Instead, a higher level of addition was selected to replace the lowest level.

The REM addition had a strong effect on the recoveries of manganese, titanium, and boron. The selected formulations from Task II were used as the baseline. Manganese, titanium, and boron additions had to be re-calculated for each level of REM addition in an effort to give the same weld metal composition as the selected Task II

formulations. The Task III matrix is given in Table 4. Based on the oxygen and porosity results from the test welds, one formulation from each depth was selected for the production of V-groove welds.

4.2 Electrode Production

The coating ingredients were purchased from Cor-Met in Brighton, MI. The composition of the ferro-alloys from the material certification reports is given in Table 5. The exact composition of the Fe-Si-REM was determined by inductively coupled plasma (ICP) analysis, and is presented in Table 5. The Fe-Si-REM was purchased from Jiangsu Metals and Minerals Import and Export Corp. in Nanjing, China. Coating compositions are given throughout the document as weight percent of the ferro-alloy addition. The compositions can be converted to weight percent of the alloy addition using the data given in Table 5.

Coating ingredients were shipped to CSM where the dry mix was made. Mixing was performed in a V-blender with ceramic balls for at least two hours. The dry mix was returned to Cor-Met for extrusion. Cor-Met added approximately 10 wt. pct. potassium silicate as a binder and extruded the flux onto a 1/8 inch (3.2 mm) diameter steel core wire. The composition of the core wire is given in Table 6. The extruded rods were baked at 190 C for one hour to remove moisture. The coating diameter to wire diameter ratio was 1.71 for the extruded electrodes. The weight of the coating was 0.039 g/mm of electrode for the 1F3 formulation after baking. The density of the coating will vary slightly from one formulation to another depending on the proportion of metallic additions. The finished electrodes were shipped to Global Industries Ltd. in New Iberia, LA. Global performed a low temperature bake on the rods to remove any absorbed moisture and applied a water-proof coating.

Table 4: Task III Test Matrix.

	Depth (ft)	Fe-Mn (wt. pct.)	Fe-Ti (wt. pct.)	Fe-B (wt. pct.)	Fe-Si-REM (wt. pct.)
1R1	70	8.8	8.8	0.3	1.0
1R2	70	7.8	7.4	0.3	2.5
1R3	70	6.9	6.4	0.2	4.0
2R1	140	10.0	6.5	0.5	1.0
2R2	140	8.7	5.4	0.4	2.5
2R3	140	7.7	4.6	0.3	4.0
3R1	200	12.0	4.6	0.4	1.0
3R2	200	10.1	4.1	0.2	2.5
3R3	200	8.8	3.7	0.2	4.0
4R1	300	12.8	2.4	0.9	1.0
4R2	300	10.4	2.3	0.6	2.5
4R3	300	8.8	2.3	0.5	4.0

4.3 Welding

One test weld was produced with each of the formulations at the four test depths of 70, 140, 200, and 300 ft (21, 43, 61, 91 m). The welds were produced by Global in a hyperbaric chamber pressurized to simulate the appropriate underwater depth. The Task I test welds and the set of experiments with the T1B1 formulation in Task II were deposited using a gravity-welding apparatus. All other experiments were deposited manually due to difficulties with the mechanical apparatus. Manual welding was performed by qualified professional diver/welders. The base metal is a low carbon-manganese steel, the composition is listed in Table 6. A three-layer deposit scheme was used, consisting of four beads in the first layer, three in the second, and two in the final layer.

After analysis of the test welds, one composition from each of the three tasks was selected for each depth, and V-groove welds were prepared. The base metal was a 1-inch thick API 2W Grade 50 plate. The weld preparation was a 5/8 inch (16 mm) deep V-groove with a 60 degree included angle. Approximately 31 passes in Task I, and 24 passes in Task II were required to complete the weldments. The V-groove welds were completed manually by qualified professional diver/welders in the hyperbaric facility at Global Divers, New Iberia, LA. Finished welds were shipped to Colorado School of Mines for analysis.

4.4 Radiography

Radiography of the V-groove welds was supplied by Global from an independent testing facility. The welds were interpreted according to the AWS D3.6 Specification for Underwater Welding by an ASNT level II inspector.

Table 5: Composition of Ferro-Alloys (wt. pct.)

	Mn	Ti	B	Ce+La	Si	Al	C	P	S	Fe
Fe-Mn	88.95	--	--	--	0.75	--	0.145	0.186	0.008	bal.
Fe-Ti	--	38.14	--	--	0.61	2.93	0.170	0.120	0.027	bal.
Fe-B	--	--	17.50	--	0.80	0.21	0.260	0.018	0.004	bal.
Fe-Si-REM	0.37	0.23	--	39.1	34.80	0.11	0.246	--	0.017	bal.

Table 6: Composition of Steel Base Plates and Core Wire.

	C (wt. pct.)	Mn (wt. pct.)	Si (wt. pct.)	Ti (ppm)	B (ppm)
Test Welds	0.14-0.22	0.6-0.8	0.21	<100	<5
V-Groove	0.05-0.14	1.51	0.4	<100	5
Core Wire	0.01	0.15	0.02	<100	<5

4.5 Metallography

Area fraction of porosity and top bead microstructure were quantified using standard metallographic techniques. Two cross-sections from each weld were examined. Area fraction porosity was measured at 10x magnification by overlaying a transparent grid of 1mm squares on a photomicrograph and counting the number of squares over pores divided by the total number of squares over the weld metal. Four areas were analyzed. The average and 90 pct. confidence interval of the four measurements were reported.

Top bead microstructure was examined at 250x in Task I and at 500x magnification in Task II and Task III. A higher magnification was required in Task II and Task III to resolve the finer microstructure. A 2 pct. nital etch was used. A total of six photomicrographs were examined from each Task I weld, three from each of two cross-sections. A total of ten photomicrographs were examined from each Task II and Task III weld, five micrographs from each of the two cross-sections, so that a larger area was covered to compensate for the higher magnification. The microstructures were classified according to the IIW classification scheme for steel weld metal into PF (primary ferrite), FS (ferrite with second phase aligned or non-aligned), and AF (acicular ferrite) (IIW 1988). A one thousand point count on each weld, based on two cross-sections, was used to quantify the proportions of the different microstructural constituents.

A quantitative survey of the micro-cracking was conducted on the metallographic specimens from selected welds by examining 100 fields at 200x on each cross-section and counting the number of fields containing micro-cracks vs. the number of fields which were free of cracks. Two cross-sections from each weld were examined. The data was reported as a percentage by dividing the number of fields containing cracks over the total number of fields examined.

4.6 Chemical Analysis

Weld metal chemical compositions were measured by an independent lab in Denver, CO using optical emission spectroscopy. It was found that porosity on the surface to be examined significantly influenced the results. A procedure was developed which produces a flat surface on the top bead by peening with a ball-peen hammer, then grinding lightly to clean up the surface. When the flat surface for analysis was produced by grinding alone, the top layer of weld metal was frequently removed completely, and sub-surface porosity was exposed. The peening procedure produced a flat, pore-free surface on the top layer of the deposit, resulting in a more accurate analysis. In addition, a deposit scheme which uses two beads in the top layer was adopted, so that the chemical analysis could more easily be performed on the top layer. In Tasks II and III, two locations from each weld were tested, and the average reported. In Task I, one location from each weld was tested due to a limited amount of material.

Oxygen and nitrogen were measured at Colorado School of Mines by combustion analysis with a Leco oxygen/nitrogen analyzer. Five specimens from each weld were tested to give a reasonable level of confidence. The average and 90 pct. confidence interval were reported.

4.7 Hardness

Vickers microhardness measurements were made to determine the hardness of the top-bead microstructure. A 1-kg load was used to make an indentation that was larger than the individual microstructural constituents and give an average hardness. Five indentations were made on each of the two metallographic mounts from each experiment resulting in a total of ten measurements from each weld. The average, maximum, and 90 pct. confidence interval were reported.

4.8 Mechanical Testing

Results of all-weld-metal tensile tests and Charpy V-notch impact toughness tests were supplied by Global from an independent testing facility. Full size Charpy bars and tensile bars with a 1/4 inch (6.4 mm) round reduced section were used. Five Charpy impact test bars were broken at 28 °F (-2 °C), in accordance with the AWS D3.6 Specification for Underwater Welding (AWS 1989). Percent shear was measured by the testing facility. The area occupied by porosity was not considered in the measurement.

5 RESULTS

The chemical composition, porosity, microstructure, and mechanical property results from steel test welds and V-groove welds are presented in Tables 7-15.

Table 7: Results of Steel Test Welds With Increasing Fe-Mn Additions.

Formulation	Depth	Fe-Mn	C	Mn	Si	O		Porosity		Microstructure		
	(ft)	(wt. pct.)	(wt. pct.)	(wt. pct.)	(wt. pct.)	(ppm)	+/-	(pct.)	+/-	PF	FS	AF
1F1	70	12.5	0.052	0.47	0.24	1174	69	1.8	0.7	31	58	11
1F2	70	13.5	0.035	0.45	0.24	1160	66	2.1	0.2	33	52	15
1F3	70	14.5	0.056	0.42	0.19	1125	60	0.8	0.3	24	53	21
2F1	140	13	0.042	0.40	0.32	1433	93	7.3	3.1	22	63	15
2F2	140	14.5	0.044	0.42	0.16	1264	44	1.3	0.3	27	55	17
2F3	140	16	0.042	0.42	0.22	976	123	1.9	0.9	34	51	15
3F1	200	14	0.049	0.46	0.24	1476	112	3.5	0.4	30	51	19
3F2	200	15	0.037	0.25	0.12	1650	142	3.0	1.3	42	44	14
3F3	200	16	0.040	0.26	0.13	1215	53	2.1	0.6	36	40	20
4F1	300	14	0.055	0.43	0.28	1397	266	5.6	2.3	30	57	12
4F2	300	15	0.060	0.26	0.13	1137	39	5.2	2.6	30	53	17
4F3	300	16	0.045	0.33	0.14	1290	131	4.8	1.8	34	46	21

Table 8: Results of Steel V-groove Welds With Increasing Fe-Mn Additions.

Formulation	Depth	Fe-Mn	C	Mn	Si	O		Porosity	Microstructure		
	(ft)	(wt. pct.)	(wt. pct.)	(wt. pct.)	(wt. pct.)	(ppm)	+/-	(pct.)	PF	FS	AF
1F3	70	14.5	0.036	0.69	0.30	1328	145	2.5	27	58	15
1F3	140	14.5	0.047	0.52	0.21	1492	68	2.9	36	60	4
2F3 (1^{st})	140	16	0.041	0.58	0.23	1437	89	3.9	38	51	11
2F3 (2^{nd})	140	16	0.051	0.49	0.21	1390	176	1.9	45	48	7
3F3	200	16	0.050	0.47	0.26	1470	76	1.5	33	61	5
4F2	300	15	0.053	0.50	0.24	1462	76	2.3	53	42	5

Table 9: Results of Mechanical Testing on Steel V-groove Welds With Increasing Fe-Mn Additions.

		All Weld Metal Tensile			Charpy Toughness @28 F (ft-lb)			
Formulation	Depth (ft)	Yield Stress (psi)	Ultimate Stress (psi)	Elonga-tion (pct.)	Average	Min.	Max.	Shear (pct.)
1F3	70	64,313	71,098	18.6	28.6	28	30	90
1F3	140	57,142	65,429	8.3	24.2	23	26	100
2F3 (1st)	140	54,784	61,451	6.0	22.0	20	24	90
2F3 (2nd)	140	56,440	64,640	11.7	25.2	23	28	100
3F3	200	53,440	58,520	3.6*	17.4 (23)	8 (22)	24	100
4F2	300	53,800	58,800	6.8	18.6	17	20	100
* The tensile bar fractured at a large pore.								
( ) Values in parenthesis only consider the three charpy bars without cracks.								

Table 10: Results of Steel Test Welds With Ti-B Additions.

	Fe-Mn	Fe-Ti	Fe-B	C	Mn	Ti	B	O		Hardness					Porosity			Microstructure
	wt. pct.	wt. pct.	wt. pct.	wt. pct.	wt. pct.	ppm	ppm	ppm	+/-	avg	+/-	max	avg	+/-	PF	FS	AF	
1T1B1	14.5	5.0	0.5	0.060	0.86	125	18	875	7	304	5	322	0.6	0.5	20	3	77	
1T1B2	14.5	5.0	0.9	0.059	0.72	310	18	912	124	301	12	340	1.1	0.5	10	1	90	
1T1B3	14.5	5.0	1.2	0.055	0.91	150	48	887	29	321	7	340	0.8	0.2	5	40	55	
1T2B1	10.5	10.0	0.2	0.050	0.61	165	8	966	76	283	6	302	1.9	0.9	30	10	60	
1T2B2	12.4	10.0	0.4	0.060	0.83	280	20	797	25	305	4	316	0.7	0.2	15	4	81	
1T2B3	10.5	10.0	0.6	0.048	0.67	175	25	1005	46	277	6	297	2.2	0.4	18	2	82	
1T3B1	8.5	15.0	0.2	0.055	0.66	305	11	929	29	296	7	317	3.7	0.8	11	3	86	
1T3B2	8.5	15.0	0.4	0.060	0.66	400	22	911	48	292	7	311	4.7	1.7	10	2	89	
1T3B3	8.5	15.0	0.5	0.060	0.67	265	29	934	35	288	5	302	4.2	2.0	12	2	87	
2T1B1	16.0	5.0	0.5	0.065	0.95	190	21	937	30	329	9	361	1.4	0.6	10	3	87	
2T1B2	14.5	5.0	0.9	0.063	0.70	330	19	1012	38	274	7	290	2.4	0.5	19	2	78	
2T1B3	16.0	5.0	1.2	0.055	0.97	150	46	866	28	362	8	388	1.2	0.6	4	68	28	
2T2B1	10.6	10.0	0.2	0.060	0.67	720	10	1317	95	279	8	297	4.2	0.5	30	12	58	
2T2B2	13.2	10.0	0.4	0.060	0.87	200	21	856	42	320	5	336	1.9	0.6	15	4	81	
2T2B3	10.6	10.0	0.6	0.050	0.62	165	20	1264	54	286	12	311	4.6	0.7	13	1	86	
2T3B1	12.5	7.5	0.2	0.050	0.63	145	7	942	46	258	8	289	2.3	0.3	32	38	31	
2T3B2	12.5	7.5	0.5	0.060	0.58	160	13	1222	28	268	7	300	2.5	0.9	28	10	62	
2T3B3	12.5	7.5	0.7	0.053	0.73	195	27	1086	52	280	9	301	1.7	0.5	23	2	76	
3T1B1	15.4	5.0	0.5	0.070	0.73	230	12	1039	27	288	6	313	1.4	0.4	21	18	62	
3T1B2	14.5	5.0	0.9	0.070	0.70	800	16	1231	32	280	12	316	3.4	1.3	16	1	83	
3T1B3	15.4	5.0	1.3	0.065	0.70	115	36	1003	58	305	12	343	2.1	1.0	7	38	56	
3T2B1	11.3	10.0	0.2	0.058	0.53	275	6	1589	132	266	9	291	4.7	1.0	30	13	57	
3T2B2	13.1	10.0	0.4	0.070	0.81	220	20	1068	81	342	18	401	4.4	1.4	15	9	76	
3T2B3	11.3	10.0	0.6	0.065	0.52	290	17	1348	179	301	6	314	4.5	0.3	17	1	82	
3T3B1	12.5	7.5	0.3	0.060	0.32	540	9	1485	71	268	8	291	3.8	0.7	29	32	37	
3T3B2	12.5	7.5	0.5	0.063	0.49	240	12	1330	98	270	7	297	3.8	1.0	25	7	68	
3T3B3	12.5	7.5	0.8	0.060	0.60	165	24	1411	66	294	13	345	5.4	1.5	17	3	79	
4T1B1	14.5	5.0	0.9	0.072	0.68	1100	12	1969	139	242	9	275	8.0	2.4	31	11	59	
4T1B2	15.0	5.0	1.2	0.070	0.69	240	37	1251	91	309	9	350	2.8	0.7	6	24	70	
4T1B3	15.0	5.0	1.8	0.080	0.77	345	48	2097	756	361	10	386	5.0	0.5	2	85	14	
4T2B1	13.8	10.0	0.3	0.065	0.74	210	10	1173	35	306	14	350	4.3	1.1	11	13	76	
4T2B2	13.8	10.0	0.5	0.070	0.60	125	13	1750	500	329	6	357	9.5	1.2	13	9	78	
4T2B3	13.8	10.0	1.0	0.055	1.03	435	30	1202	81	340	22	380	6.8	2.0	4	43	52	
4T3B1	15.0	2.5	0.7	0.065	0.46	325	10	1366	112	247	8	283	2.7	1.3	30	57	12	
4T3B2	15.0	2.5	1.4	0.060	0.57	365	29	1327	221	275	11	311	3.2	0.6	34	21	45	
4T3B3	15.0	2.5	2.8	0.060	0.59	235	77	1317	243	314	9	343	4.8	1.2	2	94	4	

Table 11: Results of Steel V-groove Welds With Ti-B Additions.

	Fe-Mn	Fe-Ti	Fe-B	C	Mn	Ti	B	O		Hardness					Porosity			Microstructure
	wt. pct.			wt. pct.	wt. pct.	ppm	ppm	ppm	+/-	avg	+/-	max	avg	+/-	PF	FS	AF	
1T2B2	12.4	10.0	0.4	0.052	1.03	330	22	818	19	296	13	325	0.8	0.3	12.2	0.3	87.8	
2T3B3	12.5	7.5	0.7	0.052	0.51	95	14	1119	9	260	9	289	3.5	1.6	28.5	4.9	66.8	
3T1B1	15.4	5.0	0.5	0.054	0.60	75	8	1180	70	286	9	308	1.8	0.4	18.1	7.9	73.8	
4T3B2	15.0	2.5	1.4	0.056	0.48	145	20	1223	63	226	8	251	4.0	1.6	33.6	9.7	56.5	

Table 12: Results of Mechanical Testing on Steel V-groove Welds With Ti-B Additions.

		All Weld Metal Tensile			Charpy Toughness @28 F (ft-lb)			
Formul-ation	Depth (ft)	Yield Stress (psi)	Ultimate Stress (psi)	Elonga-tion (pct.)	Average	Min.	Max.	Shear (pct.)
1T2B2	70	66,692	71,231	4.2	22	21	24	90-100
2T3B3	140	77,698	80,038	3.7	26	24	30	100
3T1B1	200	63,750	67,500	6.4	22	22	22	100
4T3B2	300	56,830	60,189	8.7	20	19	20	100

Table 13: Results of Steel Test Welds With REM Additions.

	Fe-Mn	Fe-Ti	Fe-B	Fe-Si-REM	C	Mn	Si	Ti	B	O		Hardness					Porosity			Microstructure		
	wt. pct.	wt. pct.	wt. pct.	wt. pct.	wt. pct.	wt. pct.	wt. pct.	ppm	ppm	ppm	+/-	avg	+/-	max	avg	+/-	PF	FS	AF			
1R1	8.8	8.8	0.33	1.0	0.046	0.45	0.45	175	11	1310	139	275	4	291	4.5	1.4	22	1	77			
1R2	7.8	7.4	0.26	2.5	0.050	0.39	0.48	325	8	1509	117	271	7	283	5.6	1.7	18	4	79			
1R3	6.9	6.4	0.21	4.0	0.048	0.36	0.54	355	8	1657	203	262	6	280	4.2	0.3	18	3	79			
2R1	10.0	6.5	0.53	1.0	0.040	0.39	0.35	180	10	1937	90	255	10	289	5.0	1.5	19	25	55			
2R2	8.7	5.4	0.40	2.5	0.043	0.16	0.19	175	6	2556	72	260	9	285	7.7	0.7	16	34	50			
2R3	7.7	4.6	0.32	4.0	0.040	0.27	0.34	215	5	2394	319	248	10	277	8.3	2.5	43	21	36			
3R1	12.0	4.6	0.35	1.0	0.064	0.55	0.39	330	11	1841	162	241	9	271	5.5	0.5	29	15	56			
3R2	10.1	4.1	0.24	2.5	0.056	0.17	0.30	300	5	2211	273	235	15	286	6.7	1.6	46	25	29			
3R3	8.8	3.7	0.18	4.0	0.051	0.26	0.30	230	5	2476	98	221	12	262	6.0	0.3	54	31	15			
4R1	12.8	2.4	0.92	1.0	0.050	0.47	0.36	375	14	1816	102	255	7	276	4.8	1.7	28	10	62			
4R2	10.4	2.3	0.59	2.5			Did not produce a deposit															
4R3	8.8	2.3	0.45	4.0			Did not produce a deposit															

Table 14: Results of Steel V-groove Welds With REM Additions.

	Fe-Mn	Fe-Ti	Fe-B	Fe-Si-REM	C	Mn	Si	Ti	B	O		Hardness			Porosity			Microstructure
	wt. pct.	wt. pct.	wt. pct.	wt. pct.	wt. pct.	wt. pct.	wt. pct.	ppm	ppm	ppm	+/-	avg	+/-	max	avg	+/-	PF	FS	AF
1R1	8.8	8.8	0.33	1.0	0.050	0.50	0.48	240	16	1565	179	248	5	262	5.3	0.8	17	5	78
2R1	10.0	6.5	0.53	1.0	0.050	0.23	0.40	260	14	2533	239	237	9	265	9.1	1.1	30	13	57
3R1	12.0	4.6	0.35	1.0	0.050	0.62	0.36	600	12	2010	285	249	7	272	7.1	0.7	34	6	59
4R1	12.8	2.4	0.92	1.0	0.060	0.37	0.25	250	14	2088	90	258	9	280	8.3	1.3	24	14	62

Table 15: Results of Mechanical Testing on Steel V-groove Welds With REM Additions.

		All Weld Metal Tensile			Charpy Toughness @28 F (ft-lb)			
Formulation	Depth (ft)	Yield Stress (psi)	Ultimate Stress (psi)	Elongation (pct.)	Average	Min.	Max.	Shear (pct.)
1R1	70	69,729	75,436	6.8	24	20	27	90-100
2R1	140	56,725	60,695	5.0	14	12	16	80-100
3R1	200	56,541	62,603	5.0	18	16	19	100
4R1	300	54,867	59,042	4.25	17	16	20	80-100

6 DISCUSSION

6.1 Electrode Weldability

6.1.1 Task I: Increasing Ferro-Manganese Addition

Comments on electrode performance were provided in work reports from Global Divers. In Task I, the electrode performance was generally acceptable to the diver/welders; however, there were some negative remarks. It was noted that the slag was excessively fluid, especially at higher ferro-manganese additions and at greater depths. Some difficulty in slag detachability was noted. Wire brushing and light grinding were required to clean between passes. Experiments at CSM revealed a thin, crumbly slag layer, which required heavy wire-brushing for removal.

The excessive fluidity may have been caused by oxidation of manganese resulting in increased MnO content in the slag. Chemical analysis by EDS of slag samples from the 1F3 and 2F3 formulations at 140 ft (43 m) gave contents of 17 and 19 weight percent manganese respectively. X-ray diffraction showed the primary crystalline constituent of the slag to be $(Fe,Mn)TiO_3$, which made up about 40 pct. of the slag. The other major constituent of the slag was amorphous. Iron and manganese oxides were not present in the electrode coating; therefore, it is apparent that much of the iron and ferro-manganese added to the coating are partitioned to the slag as oxides. The manganese oxide, in excessive quantities, had an adverse effect on the slag behavior. Greater amounts of MnO would be transferred to the slag with increasing depth and ferro-manganese

additions. MnO is a basic oxide, which will break up silicate and titanate networks, thus increasing slag fluidity (Bodsworth and Bell p. 81). Comments from the diver/welders indicated that slag behavior was worse with increasing depth and ferro-manganese additions.

6.1.2 Task II: Titanium-Boron Addition

The comments of the diver/welders regarding the behavior of the Task II electrodes were mostly positive. Observations of the Task II experiments indicated that slag removal was easy, and slag fluidity was not mentioned as a problem. Experiments at Colorado School of Mines revealed a significant difference in the slag characteristics between Task I and Task II formulations. The Task I electrodes produced a thin, crumbly slag which required wire-brushing for removal. Task II electrodes produced a thick, coherent slag layer which detached easily in large pieces. Increasing ferro-titanium addition increased recovery of manganese to the weld metal; therefore, less MnO is expected to have transferred to the slag. If the problems with the Task I slag behavior were caused by excessive MnO content in the slag, then it is consistent that ferro-titanium addition would improve slag behavior.

6.1.3 Task III: Rare Earth Metal Addition

The comments of the diver/welders regarding the performance of the Task III electrodes were positive. The electrodes started easily. The slag was somewhat friable and detached easily from the deposited weld metal. The molten slag was not excessively fluid, as in the case of Task I with greater levels of ferro-manganese addition. Experiments at Colorado School of Mines revealed that the slag appearance and detachability of the Task III consumables with additions of titanium, boron, and REM was similar to the Task II consumables with titanim-boron additions.

6.2 Chemical Composition of Welds

6.2.1 Task I: Increasing Manganese Addition

The weld metal chemical compositions for Task I are given in Tables 7 and 8. Weld metal composition remained approximately constant over the range of ferro-manganese addition tested. The effect of the increased ferro-manganese in the coating on weld metal manganese content is shown in Figure 15. The increase in ferro-manganese addition from 12.5 (1F1) to 14.5 wt. pct. (1F3) gave a 0.3 wt. pct. increase in manganese content for welds made in air, but no increase in manganese content for wet welds. A further increase to 16 pct. ferro-manganese failed to produce any increase in the manganese content of the underwater wet welds.

The effect of increasing ferro-manganese addition on weld metal oxygen content is shown in Figure 16. Manganese has a higher affinity for oxygen than iron, as seen in Figure 11. Increasing manganese additions are expected to decrease the oxygen content of the weld pool. In general, the highest ferro-manganese additions produced lower oxygen contents than the lowest ferro-manganese additions, but there are a few exceptions.

Weld metal oxygen content increased with depth in a somewhat different way than the results presented by Ibarra et al (1987), Figure 2. The oxygen results from Ibarra et al reached a maximum at approximately 100 ft (30 m), then decreased, and finally remained constant with further increases in depth. Ibarra et al explained the initial increase in oxygen content as being controlled by carbon oxidation, and the constant oxygen content at greater depths by water vapor equilibrium. In the present investigation, the baseline data increased continuously to 300 ft (91 m). The Task I data reached a maximum at 200 ft (61 m), then decreased slightly at 300 ft The differences in oxygen content between Task I results and results shown in Figure 2 may be due to

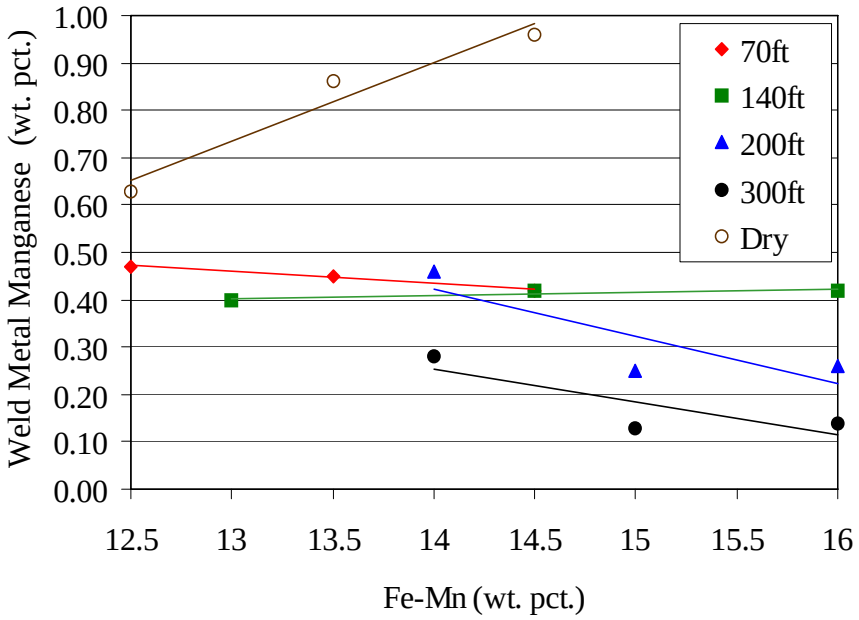

Figure 15: Weld metal manganese as a function of ferro-manganese addition for Task I test welds and dry welds made with 1F1, 1F2, and 1F3 formulations.

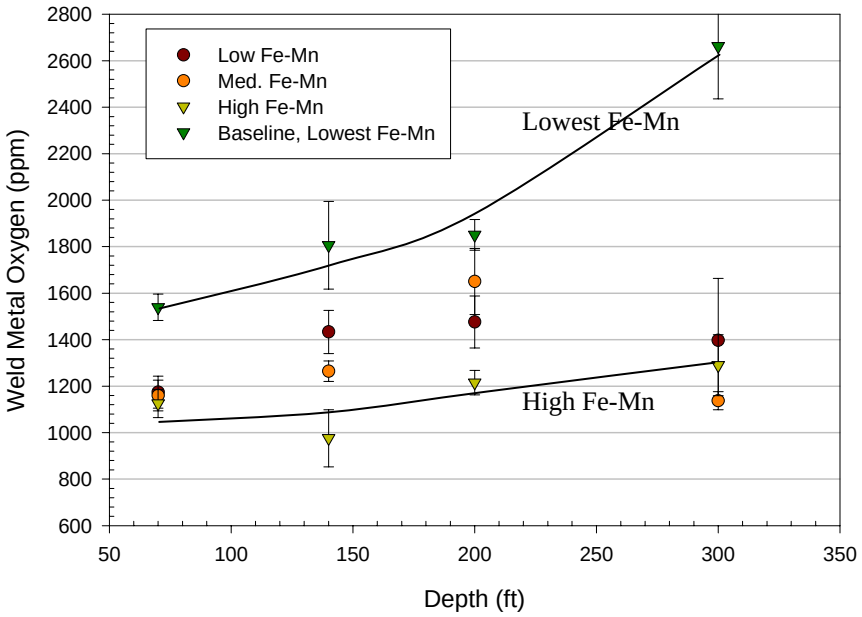

Figure 16: Weld metal oxygen as a function of depth for Task I test welds.

decreasing influence of carbon and hydrogen, and increasing influence of manganese on the weld pool oxygen content.

The trend displayed in Figure 15 of relatively constant weld metal manganese content despite increasing ferro-manganese addition in the coating can be explained by considerations of equilibrium between manganese and oxygen in the weld pool. Thermodynamic calculations indicate that the weld metal manganese and oxygen contents are determined by equilibrium between manganese and oxygen in the weld pool regardless of the initial content of manganese in the coating. The curves plotted in Figure 17 are calculated equilibrium values between manganese and oxygen in the weld pool. Equations [6.1] and [6.2] for the reaction between manganese and oxygen dissolved in iron with pure liquid manganese oxide were used to plot the curves:

$$[Mn] + [O] = (MnO) \qquad [6.1]$$

$$\log K = \log\left(\frac{(a_{MnO})}{[\%Mn][\%O]}\right) = \frac{12670}{T} - 5.62 \qquad [6.2]$$

Source: Bodsworth and Bell (1976)

[X] = X dissolved in liquid iron.

(X) = X dissolved in an oxide melt.

K = equilibrium constant for the reaction.

a_X = activity of X

%X = wt. pct. of X in liquid iron

T = absolute temperature

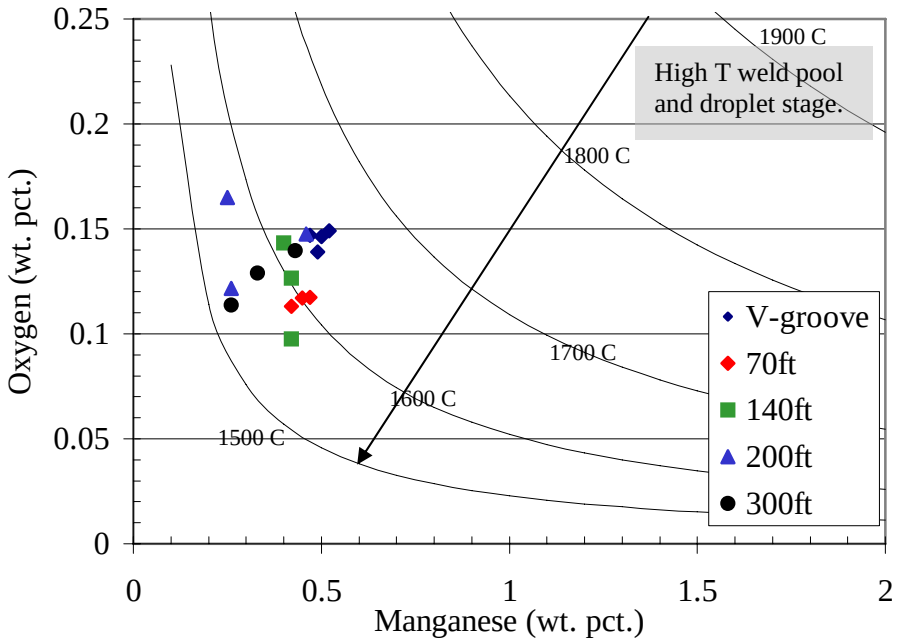

Figure 17: Weld metal oxygen as a function of weld metal manganese for Task I test welds and V-groove welds plotted against lines giving equilibrium values for manganese and oxygen in liquid iron with pure MnO.

It was assumed that the reaction product forms initially as pure MnO inclusions; therefore, the activity of MnO was taken as 1.

When data from the Task I welds are superimposed on the calculated equilibrium lines in Figure 17, it can be seen that the data clusters around equilibrium compositions near 1600 ºC. From Figure 17, it appears that at temperatures below 1600 ºC there is insufficient time for newly formed manganese oxide inclusions to separate into the slag, and they are trapped in the solidified weld metal. Therefore, the final weld metal compositions reflect equilibrium near 1600 ºC.

The equilibrium lines plotted in Figure 17 illustrate the process of inclusion formation in the weld pool. High temperatures (1800 - 1900 ºC) favor higher concentrations of dissolved manganese and oxygen. If all of the manganese added to the coatings of the formulations with higher levels of ferro-manganese addition remained in the weld metal (100 pct. recovery), the weld metal manganese content would be 1.5 to 2 wt. pct. At high temperatures in the weld pool and droplet stage, manganese contents of 1.5 to 2 wt. pct. can co-exist with oxygen contents in the range of 2000 ppm, as indicated by the shaded box in Figure 17. As the temperature drops toward the trailing edge of the weld pool, manganese and oxygen must react to form MnO, which separates into the slag. If the weld pool were a closed system, the composition of the liquid metal would follow the arrow in Figure 17, according to the stoichiometry of the reaction. However, measured weld metal oxygen contents are much higher than what is predicted by this simple approach. The weld pool is not a closed system. Due to the strongly oxidizing environment, additional oxygen can enter the weld pool while MnO is being formed. The result is that the manganese is removed from the weld pool to the slag while the oxygen content remains high due to the free availability of oxygen.

6.2.2 Task II: Titanium-Boron Addition

The chemical compositions of the Task II welds are given in Tables 10 and 11.

Titanium has a stronger affinity for oxygen than iron, manganese, or boron, as indicated in Figure 11. As a result, titanium is expected to increase the recoveries of the weaker oxide formers by combining preferentially with oxygen.

The addition of titanium had a strong effect on the recovery of both manganese and boron, as can be seen in Figures 18 and 19, and in Table 3. At 70 ft (21 m), manganese recovery increased from approximately 3.5 wt. pct. to nearly 8 wt. pct. with an increase in ferro-titanium addition from 0 to 15 wt. pct. Boron recovery nearly doubled with an increase in ferro-titanium addition from 5 to 15 wt. pct. Titanium, being the strongest deoxidant in the system, protects the other elements from oxidation; thus, a greater percentage of the weaker deoxidant remains in the weld metal, rather than being oxidized and partitioned to the slag.

The weld metal oxygen content for Task II (Ti-B) test welds tended to be lower than in Task I (Fe-Mn) for the 70 ft (21 m) test welds, but similar or even higher at greater depths. In contrast to the results of Ibarra et al (1987) presented in Figure 2, the oxygen content for Task II welds increases continuously with depth, as seen in Figure 20. Ibarra et al explained the initial increase in oxygen content as being controlled by carbon oxidation, and the constant oxygen content at greater depths by hydrogen-water vapor equilibrium. With addition of titanium, control of the oxygen content is expected to be determined by titanium oxidation, rather than oxidation of carbon or hydrogen.

Alternatively, Pope (1995) explained the plateau in oxygen content near 2000 ppm, displayed in Figure 2, by referring to the monotectic reaction in the iron-oxygen system. The monotectic point is close to 2000 ppm oxygen. On cooling, an iron-oxygen melt with an oxygen content greater than 2000 ppm will separate into two liquids, a liquid metal and a liquid oxide, before solidification. There is a driving force for the two liquids separate before solidification due to the difference in densities. The solidification product would be a metallic constituent with about 2000 ppm of oxide inclusions and an oxide constituent containing about 22.5 wt. pct. oxygen. According to the lever rule, as the oxygen content of the initial melt increases beyond the monotectic point, the

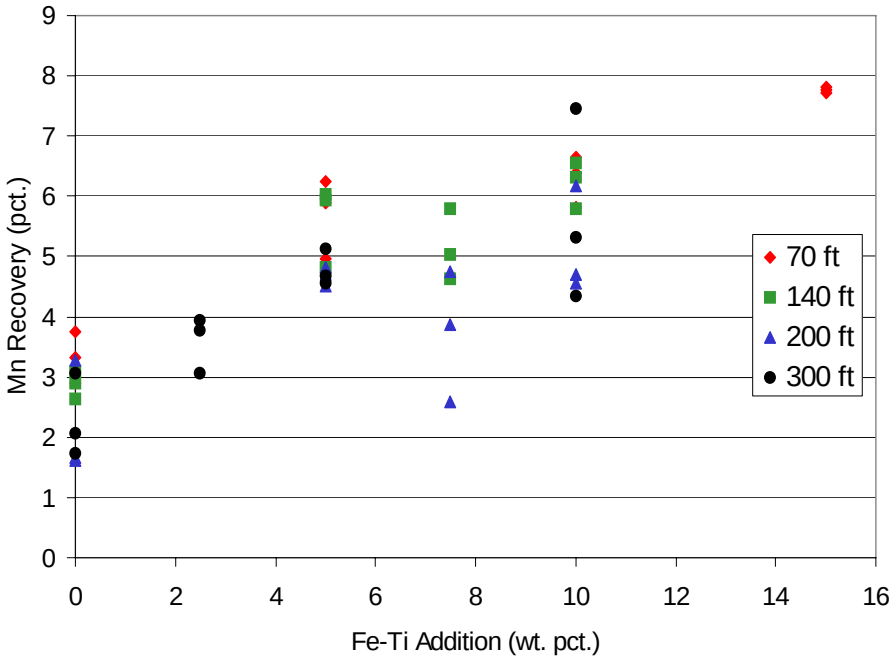

Figure 18: Manganese recovery to the steel weld metal as a function of ferro-titanium addition.

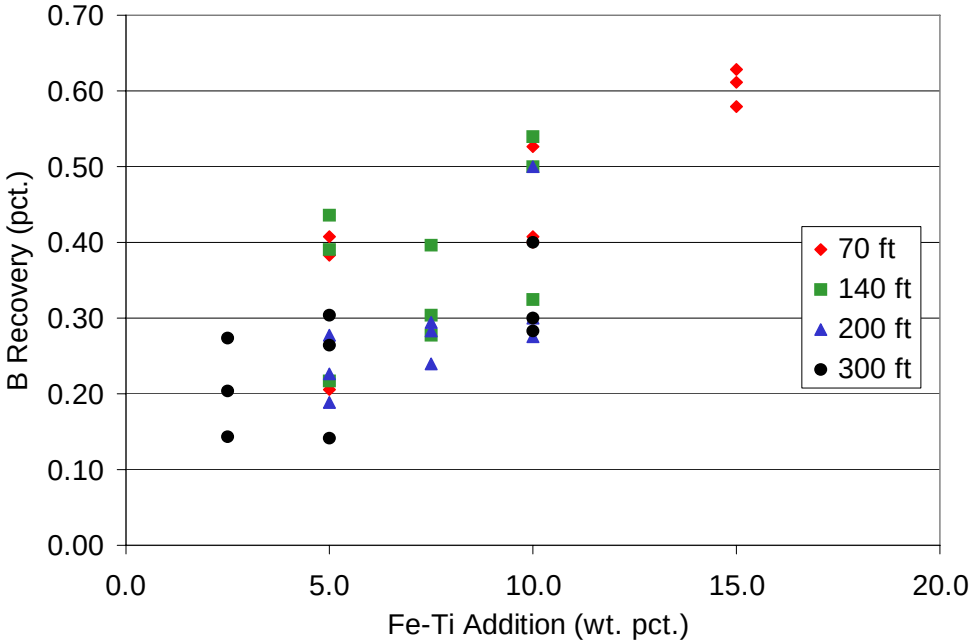

Figure 19: Boron recovery to the steel weld metal as a function of ferro-titanium addition.

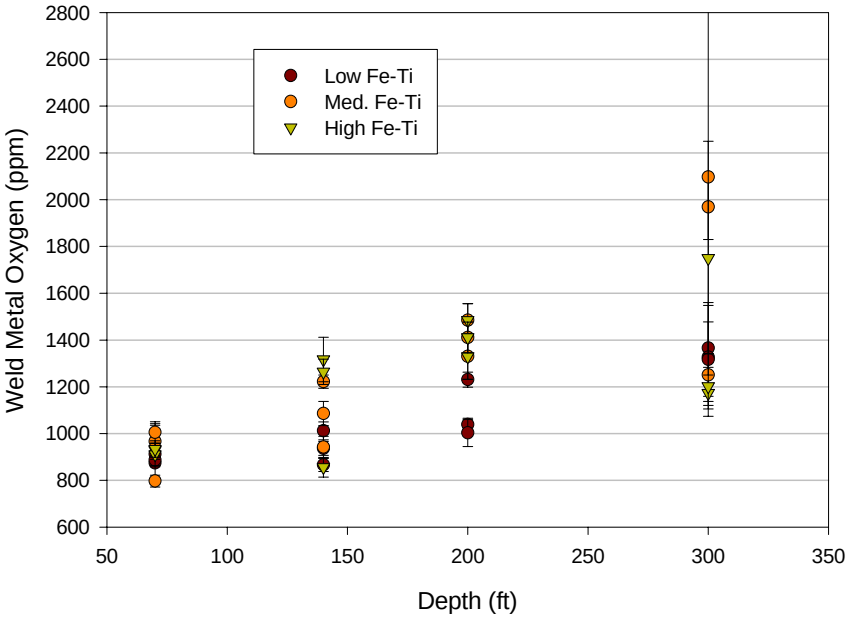

Figure 20: Weld metal oxygen as a function of depth for Task II test welds.

proportion of the oxide constituent increases at the expense of the metallic constituent, but the composition of the metal remains constant near 2000 ppm. Thus, the oxygen content of wet welds is limited to approximately 2000 ppm.

The model developed by Pope assumes that the liquid oxide will have time to separate out from the liquid metal before solidification occurs. Average weld metal oxygen contents well in excess of 2000 ppm were recorded in Tasks I, II, and III. Individual measurements exceeded 3000 ppm in some cases. Wood (1990) reported a weld metal oxygen content of 3560 ppm for a wet weld made at a depth of 560 ft (171 m). It can be concluded that the weld metal oxygen content of wet welds is not absolutely limited to values near 2000 ppm either by hydrogen-water vapor equilibrium or by the monotectic reaction in the iron-oxygen system.

For the V-groove welds, Task II showed significantly lower oxygen contents at all depths than Task I welds, as seen in Figure 21. Although many of the Task II test welds had higher oxygen contents than Task I test welds, it was possible to produce Task II V-groove welds with low oxygen by selecting the best performing formulations from the Task II test welds.

Mixed results in the effectiveness of titanium as a deoxidant may be due to the combined effects of weld pool chemistry and the physical behavior of the electrode. Addition of a strong deoxidant such as titanium is known to decrease the weld metal oxygen content when welding in air (Evans 1992). However, if the addition also influences the arc stability or slag behavior of the electrode in an adverse way, a higher weld metal oxygen content may result due to increased exposure of the weld pool to the surrounding water.

6.2.3 Task III: Rare Earth Metal Addition

Cerium and lanthanum (REM) have a much higher affinity for oxygen than any of the ferro-alloy additions used in this investigation, as shown in Figure 11. The recoveries

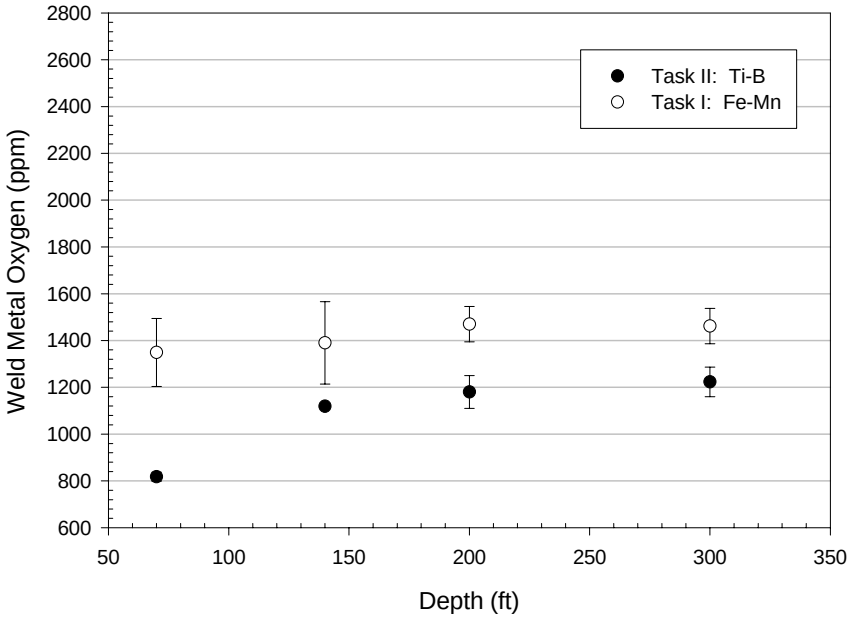

Figure 21: Weld metal oxygen as a function of depth for the Task I and Task II V-groove welds.

of manganese and boron are expected to increase with increasing addition of REM-ferro-silicon. Preliminary test welds produced at a depth of 1.5 ft (0.5 m) produced a significant increase in the recoveries of manganese and boron with the rare earth metal (REM) addition. Subsequent trials at greater depths failed to reproduce the increase in recoveries with REM addition. Results from the preliminary trials at 1.5 ft as well as the test welds at greater depths are presented in Figures 22 and 23.

Due to the high affinity of REM for oxygen, REM additions were expected to reduce the weld metal oxygen content. Strong deoxidants, such as REM, remove oxygen from the weld pool in the form of oxides, which then float out into the slag. The weld metal oxygen results from the preliminary test welds at 1.5 ft are presented in Figure 24. Weld metal oxygen was reduced by 200 ppm over the range of REM additions tested. The reduction in oxygen content was not observed in the test welds produced at greater depths, as seen in Figure 25. In fact the opposite trend occurred; the weld metal oxygen content appeared to increase with increasing levels of REM addition. It is interesting to note that the trend of oxygen as a function of depth displayed by the lowest level of REM addition in Figure 25 is similar to the one reported from Ibarra et al in Figure 2. It is possible that the strong deoxidants were overwhelmed by increased exposure to the oxidizing environment and the consumable behaved similarly to those used by Ibarra et al without addition of strong deoxidants.

Results of the Task III (REM) V-groove welds are presented in Figure 26 along with Task I and Task II results. It can be seen that weld metal oxygen contents produced by the Task III consumables are significantly higher than those produced by Task I and II consumables.

Contrary to expectations based on the thermodynamic stability of REM oxides and preliminary testing at a shallow depth, REM additions were not effective as a deoxidant. The addition of REM to the coating seems to have increased the exposure of the weld metal to the surrounding water, and thus increased oxidation of the weld pool. The REM additions may have adversely effected the behavior of the electrodes to the

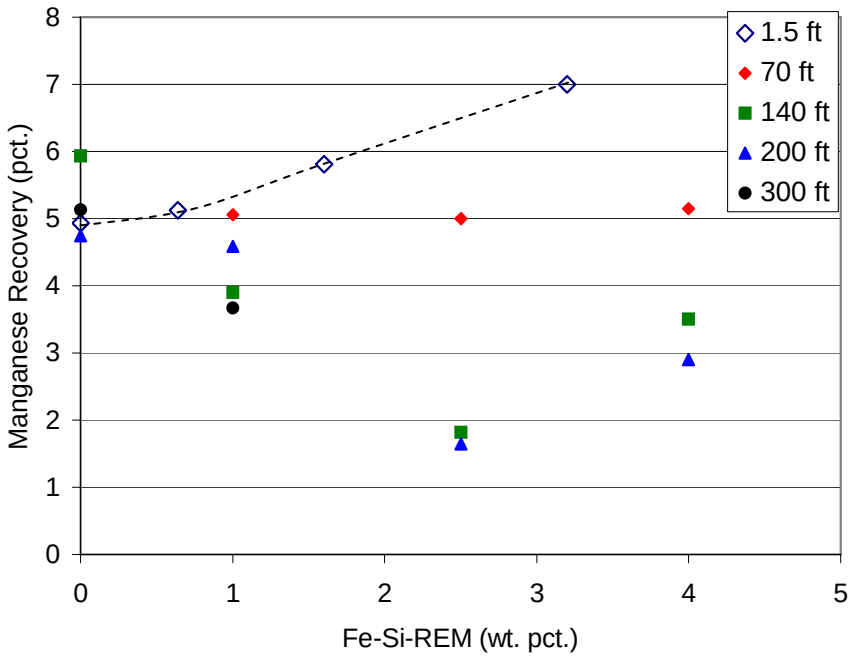

Figure 22: Effect of REM addition on manganese recovery.

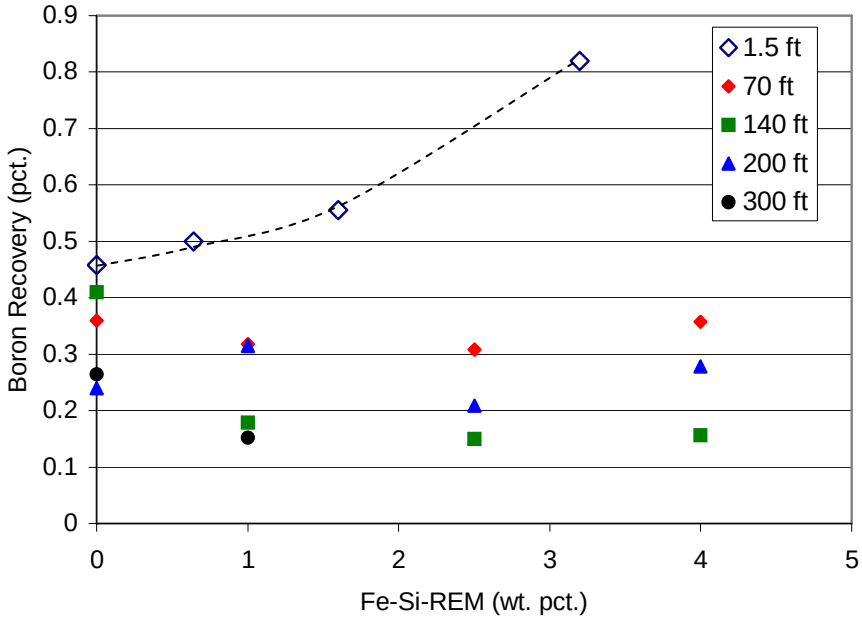

Figure 23: Effect of REM addition on boron recovery.

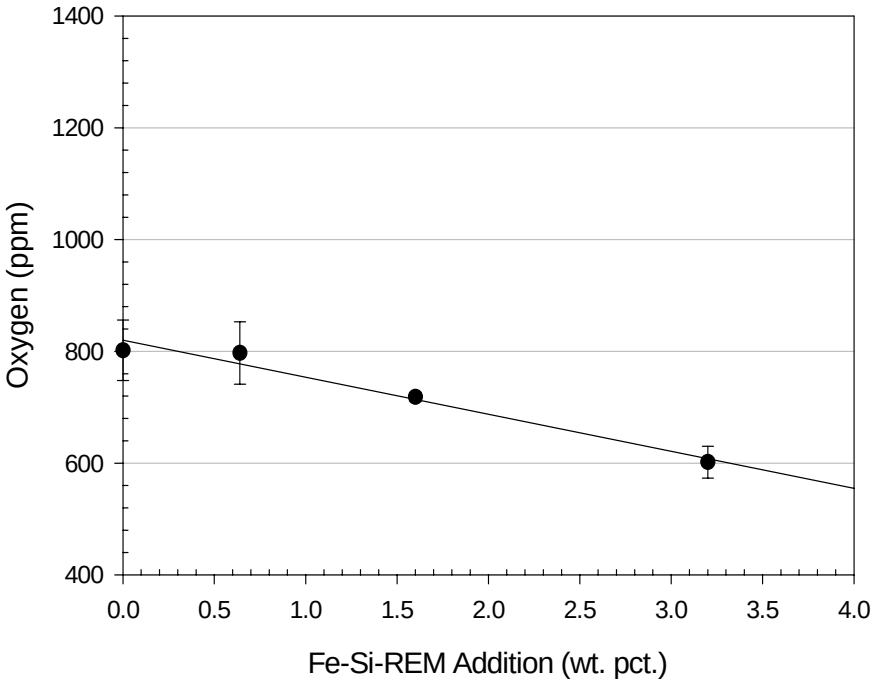

Figure 24: Effect of increasing REM addition on weld metal oxygen in test welds at a depth of 1.5 ft

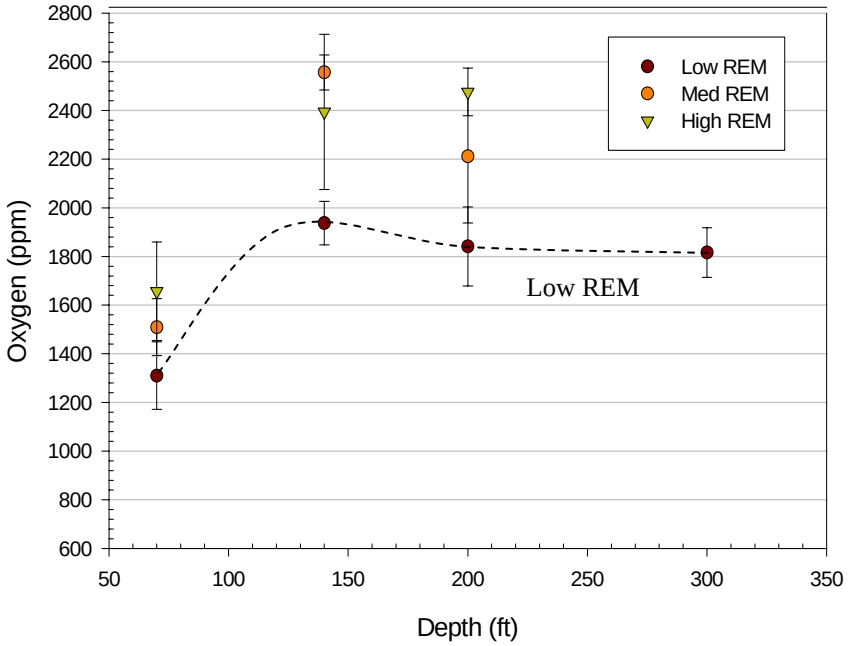

Figure 25: Effect of REM addition on oxygen content of the Task III test welds.

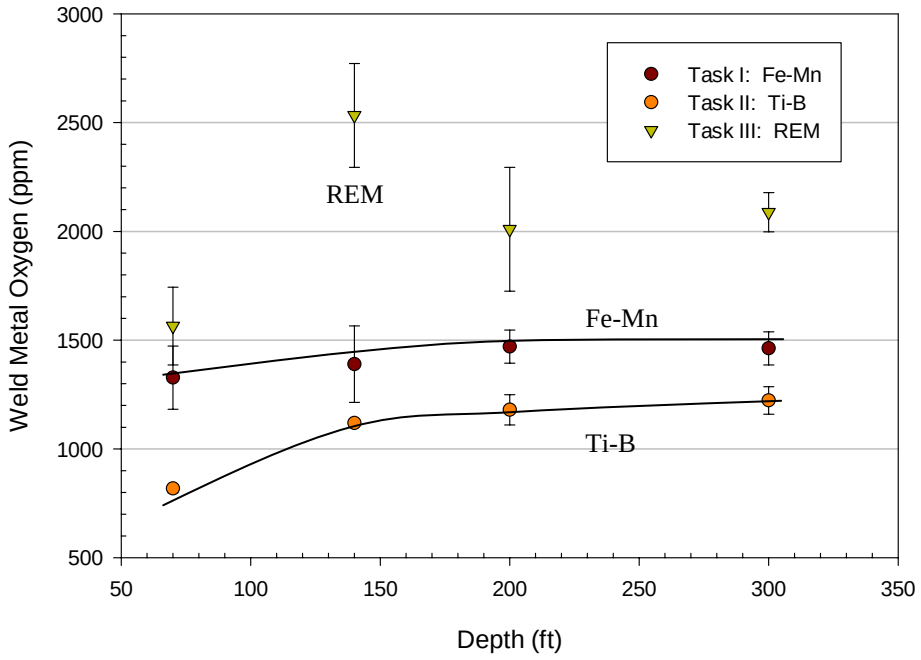

Figure 26: Weld metal oxygen content of Task I, II, and III V-groove welds.

extent that it was difficult for the diver/welders to produce a sound deposit. At the 300 ft (91 m) depth, it was only possible for the diver/welders to produce a deposit with the lowest level of REM addition. However, the comments of the diver/welders regarding the performance of the Task III consumables were positive, as discussed in section 6.1.3. Another possibility is that the slag chemistry was altered in a way that compromised the ability of the slag to shield the weld pool from the surrounding water. The possible effects of slag chemistry will be further discussed in section 6.4.

6.2.4 Weld Metal Nitrogen Content

Weld metal nitrogen content was measured to ensure that the ferro-alloys had not picked up excessive quantities of nitrogen in storage. Both ferro-titanium and ferro-boron can absorb nitrogen from the atmosphere in storage and deliver it to the weld metal. Excessive nitrogen in the weld metal can form porosity and embrittling nitrides. Nitrogen contents were in the range of 50 to 70 ppm for Task I (Fe-Mn) and Task III (REM) and 60 to 110 ppm for the Task II (Ti-B) welds. Nitrogen values were all at low enough levels that nitrogen porosity and nitrides should not pose a problem.

6.3 Porosity

6.3.1 Task I: Increasing Ferro-Manganese Addition

Higher levels of ferro-manganese addition produced lower average values for porosity in most cases, as seen in Figure 27. The reduction in porosity is not greater than the 90 pct. confidence interval on the four areas measured, indicating that there is variation in the amount of porosity from one location in the weld to another. The baseline data was collected by a previous investigator and error bars were not given. The abnormally high value produced by the 2F1 test weld in Figure 27 may have been due to

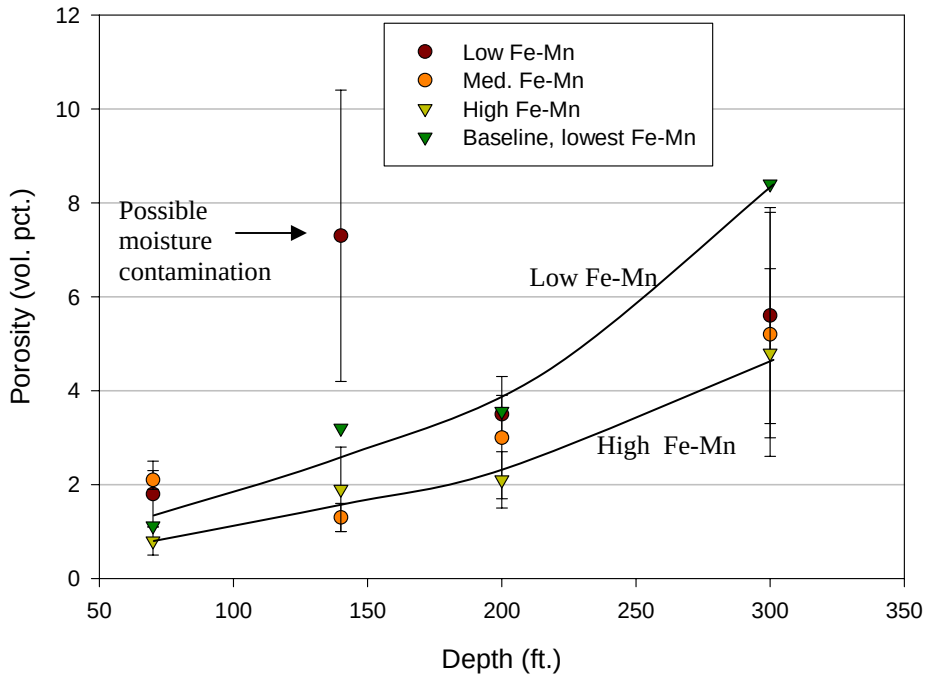

Figure 27: Porosity as a function of depth and ferro-manganese addition for Task I test welds.

contamination of the electrode coating with moisture before welding. A possible mechanism for the reduction in porosity is discussed in section 6.4.

6.3.2 Task II: Titanium-Boron Addition

Porosity had a tendency to increase as a function of increasing titanium and boron additions, as seen in Figure 28. Smaller error bars than in Task I indicate that the pores are smaller and more uniformly distributed. A possible mechanism for the increase in porosity is discussed in section 6.4.

Figure 29 shows calculated values of oxygen dissolved in iron at equilibrium with various deoxidants in the weld pool. It is important to note that the Y-axis indicates oxygen dissolved in the weld metal, and not oxygen in the form of oxide inclusions, which is measured by combustion analysis of the solidified weld metal. As a result, the the range of oxygen contents over which Figure 29 is plotted is much lower than the measured weld metal oxygen contents. Equations [6.1]-[6.6] were used to plot the equilibrium oxygen values.

$$[C] + [O] = CO_{(gas)} \qquad [6.3]$$

$$\log K = \log\left(\frac{P_{CO}}{[\%C][\%O]}\right) = \frac{1168}{T} + 2.07 \qquad [6.4]$$

Source: Bodsworth and Bell (1976)

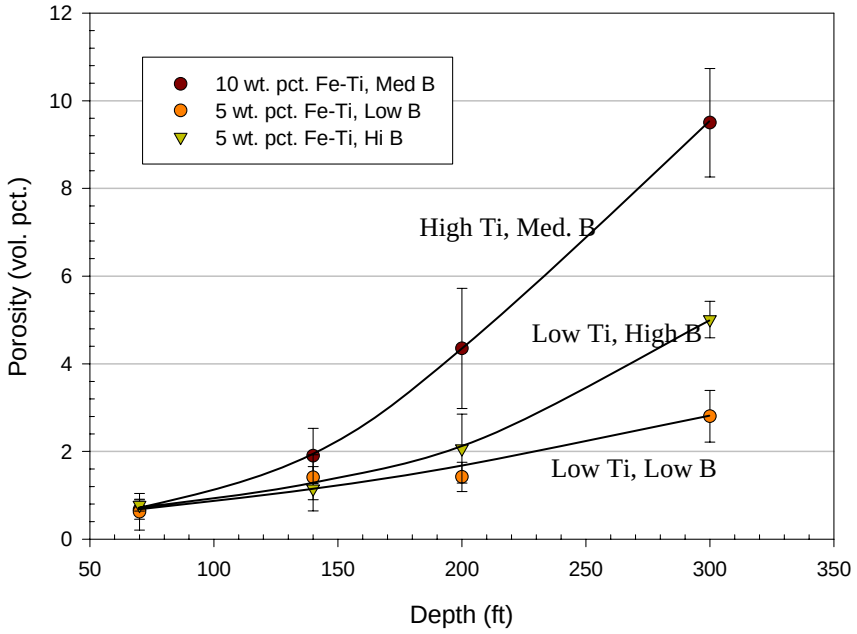

Figure 28: Porosity as a function of depth, titanium, and boron addition for selected Task II test welds.

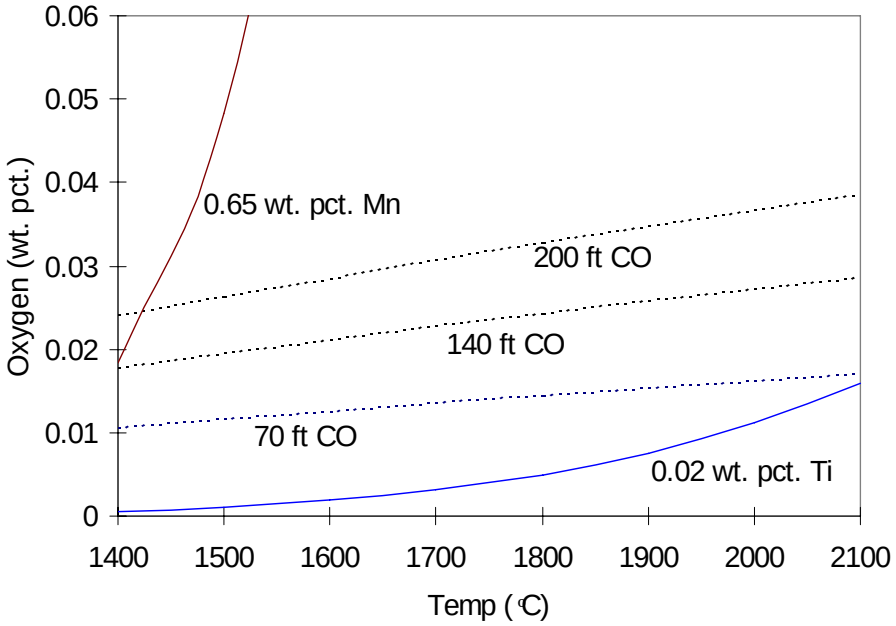

Figure 29: Weld metal oxygen at equilibrium with 0.05 wt. pct. carbon at various depths (assuming a pore gas composition of 90 pct. hydrogen 10 pct. CO), manganese with MnO, and titanium with Ti_3O_5.

$$3\,[Ti] + 5[O] = (Ti_3O_5) \qquad [6.5]$$

$$\log K = \log\left(\frac{\left(a_{Ti_3O_5}\right)}{[\%Ti]^3[\%O]^5}\right) = \frac{41500}{T} - 3.4 \qquad [6.6]$$

Source: Bodsworth and Bell (1976)

[X] = X dissolved in liquid iron.

(X) = X dissolved in an oxide melt.

K = equilibrium constant for the reaction.

a_X = activity of X

%X = wt. pct. of X in liquid iron

P_X = partial pressure of X

T = absolute temperature

It was necessary to make several assumptions in order to plot the equilibrium lines which appear in Figure 29. Activity coefficients for the elements dissolved in liquid iron were assumed to be equal to one, due to the dilute solutions involved. Concentrations of the deoxidants in the weld pool were assumed to be similar to measured weld metal compositions. The partial pressure of carbon monoxide was calculated based on the assumption that dissolved carbon and oxygen would be at equilibrium with the gas contained in porosity. Pore gas compositions have been reported in the literature as approximately 90 pct. hydrogen and 10 pct. carbon monoxide (Ando and Asahina 1983)(Suga 1986). The mole fraction of carbon monoxide was calculated from the pore gas composition and one atmosphere was added to the total pressure for every 33 ft (10 m) of underwater depth. The reaction product for titanium

oxidation is Ti_3O_5 for titanium concentrations from 0.001 to 0.16 wt. pct. Bodsworth and Bell (1976). The product was assumed to be initially in the form of pure Ti_3O_5 inclusions; therefore, the activity coefficient was assumed to be equal to one.

Figure 29 can be used to indicate which deoxidants will limit the oxygen content of the weld pool and which will be protected from oxidation by stronger deoxidants. The oxygen content of the liquid metal is limited by the element which has the lowest equilibrium value of dissolved oxygen. In a system containing only manganese and carbon, the oxygen content is limited by carbon at higher temperatures and by manganese at lower temperatures; therefore, the formation of carbon monoxide would be possible.

The deoxidizing power of carbon is reduced as underwater depth increases because a gaseous product is formed. The activity of carbon monoxide, for a given mole fraction, increases in direct proportion to the total pressure. According to Le Chatelier's principle, if the activity of the product is increased, then the reaction equilibrium will be shifted to favor the reactants. As a result, a higher total pressure favors higher concentrations of dissolved carbon and oxygen and less carbon monoxide.

In a system that includes 200 ppm titanium, oxygen content is limited by the formation of titanium oxide, and carbon monoxide formation is not possible. As was discussed in section 2.1.2, Liu et al (1994) proposed that porosity in wet welds may be caused by oxidation of carbon to form carbon monoxide or oxidation of hydrogen to form water vapor. Based on the relative position of water vapor on the Ellingham diagram in Figure 11, hydrogen is the weakest oxide former in the system and would be protected from oxidation by manganese, carbon, or titanium. If porosity in wet welds were caused by carbon monoxide or water vapor, addition of titanium should reduce porosity by protecting carbon and hydrogen from oxidation. In the present investigation, increasing titanium additions increased the porosity content of wet welds, rather than reducing porosity. As a result, it is most likely that porosity in wet welds is caused by evolution of molecular hydrogen from the weld pool, and not by carbon monoxide formation.

6.3.3 Task III: Rare Earth Metal Addition

The results of porosity measurements on the Task III (REM) test welds are presented in Figure 30. The lowest levels of porosity were produced with the lowest additions of REM. Higher additions of REM produced increased levels of porosity. As was mentioned in section 6.2.3, REM addition seems to have increased the exposure of the weld metal to oxygen and hydrogen.

The results for REM V-groove welds are presented in Figure 31 along with results from Task I and Task II V-groove welds. In accordance with the test weld results, porosity levels in the REM V-groove welds are significantly higher than those produced with ferro-manganese or titanium-boron additions.

6.3.4 Porosity as a Function of Weld Metal Oxygen Content

Porosity and weld metal oxygen content increase and decrease together for all Task I, II, and III test welds, as seen in Figure 32. For any given depth, the lowest levels of both porosity and oxygen can usually be attributed to selected Task II formulations with titanium and boron. Based on the discussion in section 2.1.2 and the discussion presented in 6.3.2, it can be assumed that porosity in wet welds is caused by hydrogen. According to the model developed by Suga (1987), the critical radius for pore nucleation decreases and the growth rate of pores increases with a higher initial concentration of hydrogen in the weld metal. Assuming that the model is correct, one would expect the volume fraction of porosity in the weld metal to be greater with a higher initial concentration of hydrogen in the weld pool and vice-versa. Based on the preceding argument, the porosity content of the weld metal can be taken as an indication of the initial hydrogen content of the weld pool, if all other variables in Suga's model (ambient pressure, welding speed) remain constant. It also must be assumed that the size distribution of porosity does not change with increasing initial hydrogen concentration so

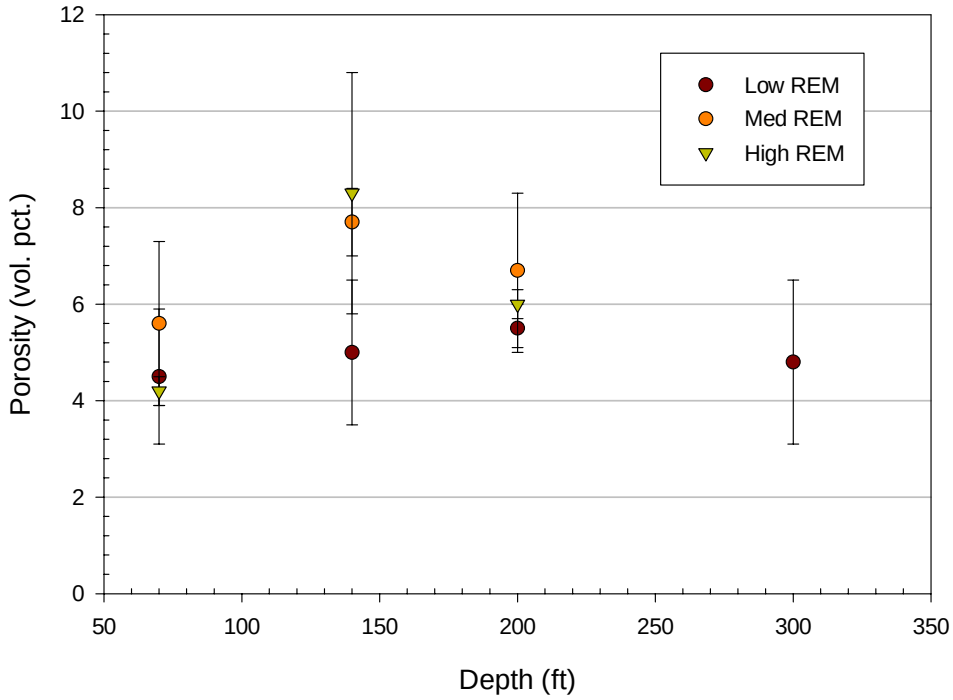

Figure 30: Porosity versus depth for Task III (REM) test welds.

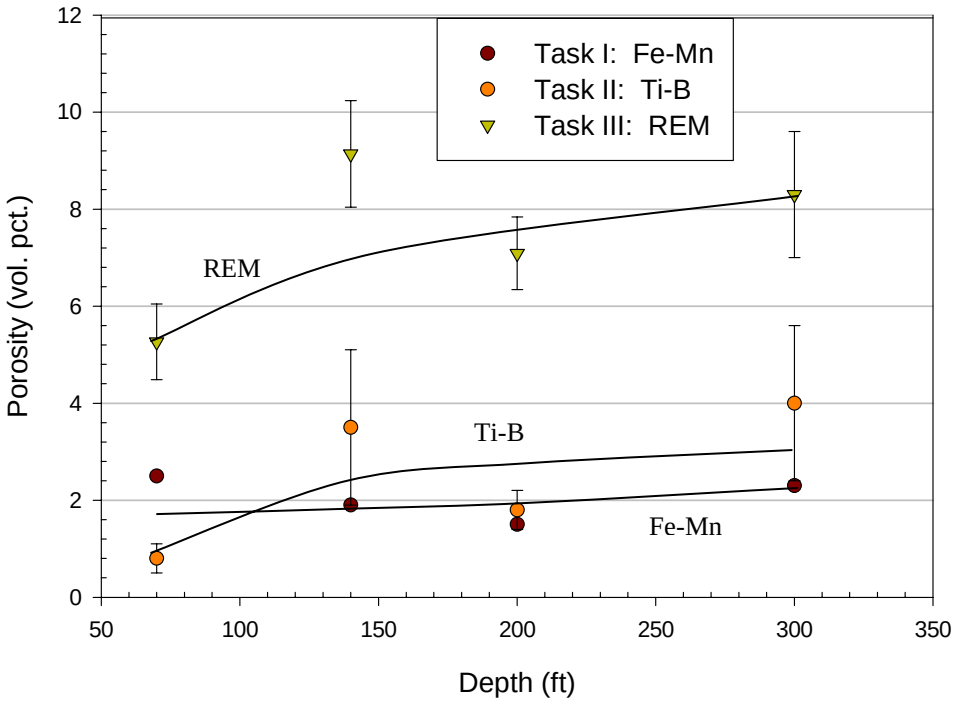

Figure 31: Porosity versus depth for V-groove welds from Task I, II, and III.

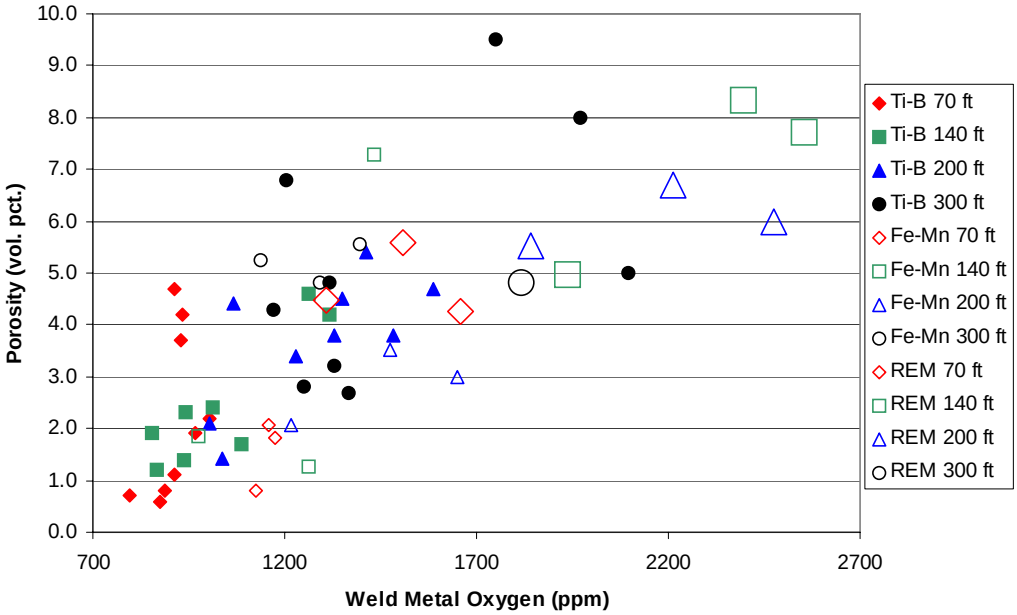

Figure 32: Porosity as a function of weld metal oxygen content for Task I, II, and III test welds. The larger open symbols are for Task III (REM).

as to make a significant fraction of the pores undetectable with the given measurement technique. If porosity is associated with the hydrogen content of the weld pool, Figure 25 indicates that the oxygen and hydrogen contents of the weld pool increase and decrease together.

Hydrogen and oxygen may be transferred directly from the gas to the weld pool as described by equation [6.7].

$$H_2O_{(gas)} = 2[H] + [O] \qquad [6.7]$$

[X] = X dissolved in liquid iron.

Alternatively, the transfer may occur by electro-chemical reactions involving the slag, as proposed by Medeiros (1997).

$$H_2O_{(gas)} + 1/2\ O_{2(gas)} + 2e^- = 2(OH^-) \qquad [6.8]$$

$$(OH^-) = [H] + [O] + e^- \qquad [6.9]$$

[X] = X dissolved in liquid iron.
(X) = X dissolved in an oxide melt.

In both cases, the concentrations of hydrogen and oxygen in the weld pool would increase or decrease together depending on the partial pressure of water vapor to which

the weld pool is exposed. In the case of the latter mechanism, the concentrations of hydrogen and oxygen in the weld pool may be influenced by the solubility and transport of hydroxyl ions in the slag.

According to the law of mass action, equation [6.10] can be written for the water dissociation reaction [6.7].

$$K=[H]^2[O]/P_{H2O} \qquad [6.10]$$

[X] = X dissolved in liquid iron.

K = equilibrium constant for the reaction.

P_{H2O} = partial pressure of water vapor.

The activities of oxygen and hydrogen are assumed to be approximately equal to their concentrations in dilute solution. Equation [6.7] predicts that for a constant P_{H2O}, an inverse relationship between the concentrations of oxygen and hydrogen in the weld pool will exist. However, an increase in P_{H2O} will result in an increase in the concentrations of both oxygen and hydrogen in the weld pool. An inverse relationship between porosity (initial hydrogen concentration) and oxygen is not observed in Figure 25 at any given depth. It can be concluded from Figure 25 that some unknown variable in the electrode formulations produced different concentrations of oxygen and hydrogen in the weld pool at a given depth. The variable must influence either the partial pressure of water vapor to which the weld pool is exposed (P_{H2O}), or the transfer of oxygen and hydrogen to the weld pool. Slag basicity is known to influence the transfer of oxygen to the weld pool, and evidence has been presented in section 2.1.2 that indicates slag basicity can influence the transfer of hydrogen to the weld pool as well.

6.4 Effects of Ferro-Alloy Additions on Slag Composition and Porosity

The concept of slag basicity was originally used to predict the partitioning of sulfur in steelmaking slags. The basicity index has been used in welding literature to correlate weld metal oxygen content to the slag composition. Basicity index has also been used to predict the water vapor solubility in slags. As discussed in section 2.1.2, the water vapor solubility in slags is related to the degree of polymerization of the melt (Turkdogan 1983). Equation [6.11], introduced by Tuliani et al, gives a ratio of network modifiers to network formers, thus giving an approximate numerical value to the degree of polymerization in a complex oxide melt.

$$BI = \frac{CaO + CaF_2 + MgO + K_2O + Na_2O + Li_2O + \frac{1}{2}(MnO + FeO)}{SiO_2 + \frac{1}{2}(Al_2O_3 + TiO_2 + ZrO_2)} \qquad [6.11]$$

Source: Tuliani et al (1969)

Medeiros and Liu (1997) found that the weld metal hydrogen content in underwater wet welds is directly related to the hydrogen content of the slag. Based on the discussions presented in sections 2.1.2 and 6.3.2, it can be concluded that hydrogen is the main source of porosity in underwater wet welds. Slag basicity, which influences the hydrogen content of the slag, may be correlated to the porosity content of underwater wet welds.

In Task I, it was noted that porosity decreased at each depth with increasing ferro-manganese addition, and in Task II, that porosity increased with increasing titanium and boron addition. In Task III, porosity content increased with increasing REM addition. These trends may be explained by the effect of slag basicity on the absorption of hydrogen into the weld pool, as discussed in section 2.1.2. Due to the oxidizing environment, most of the manganese addition partitions to the slag as MnO, a basic oxide

which increases slag basicity. Iron is also oxidized and partitions to the slag in the form of FeO, a basic oxide. Titanium and boron are stronger deoxidants than manganese and iron, and therefore protect manganese and iron from oxidation. When titanium and boron are added, MnO and FeO content of the slag decreases and titanium oxide content of the slag increases, resulting in decreased slag basicity. Ferro-manganese addition increases slag basicity toward a more neutral value, and therefore reduces porosity. Titanium and boron addition reduce slag basicity, and therefore increase porosity.

In order to confirm the concept that slag basicity may have an effect on porosity, slag samples were sent to a commercial lab for chemical analysis so that the basicity index of the slags could be calculated. Due to the expense of the analysis, only four samples were tested: 1T1B2, 3F3, 3T1B2, and 3R2. The two Ti-B slags were selected to show the effect of increasing depth on slag composition. One sample from each of Tasks I, II, and III at 200 ft (61 m) were selected to show the effect of the ferro-alloy additions on slag composition at a given depth. The slags were crushed on a steel plate and metallic particles were removed magnetically before the analysis was performed.

The analysis technique (photo optical emission spectroscopy) detected only the metallic elements, and not the oxygen contained in the slag. The slag composition in wt. pct. of oxides was calculated assuming the oxide stoichiometries given in Table 16. It is reasonable to assume that all of the metallic elements were present in the form of oxides because the coating contained only oxides and metals, the welding environment was strongly oxidizing, and metallic particles were removed from the slag samples before analysis.

Equation [6.11], which is commonly used with welding slags, was employed to calculate the basicity index. All chemical components in are given in weight percent. It was assumed that metallic titanium in the coating that was oxidized and partitioned to the slag added to the TiO_2 content rather than forming a different oxide, such as TiO or Ti_3O_5. It is not clear how other oxides of titanium would contribute to the basicity and slag behavior. Boron was neglected because it was not present in concentrations greater

Table 16: Chemical Analysis of Slags.

	Elements Reported in Slag Analysis (wt. pct.)												
	Al	Si	Zr	K	Na	Ca	Ti	Mn	Fe	B	Ce	La	
3F3	1.99	10.12	5.62	0.37	0.24	3.61	37.38	18.82	21.85	<0.10	--	--	
1T1B2	2.42	10.66	6.83	0.50	0.34	3.89	44.66	18.98	11.72	<0.10	--	--	
3T1B2	2.30	10.83	6.30	0.45	0.21	3.72	42.45	18.94	14.80	<0.10	--	--	
3R2	2.23	10.88	6.42	0.42	0.25	3.86	43.60	12.66	18.49	<0.10	0.67	0.50	
	Calculated Slag Composition in the Form of Oxides (wt. pct.)												
	Al_2O_3	SiO_2	ZrO_2	K_2O	Na_2O	CaO	TiO_2	MnO	FeO	B_2O_3	Ce_2O_3	La_2O_3	BI
3F3	3.22	18.51	6.49	0.38	0.28	4.32	22.01	20.77	24.02	0.00	--	--	0.80
1T1B2	4.03	20.09	8.13	0.53	0.40	4.80	27.12	21.60	13.28	0.00	--	--	0.58
3T1B2	3.78	20.18	7.41	0.48	0.25	4.54	25.48	21.30	16.58	0.00	--	--	0.63
3R2	3.70	20.43	7.60	0.44	0.30	4.74	26.36	14.35	20.87	0.00	0.69	0.52	0.59

than the detectability limit in any of the slag samples. Cerium and lanthanum oxides were also neglected because they do not appear in the standard basicity index formula, and they were present in low concentrations.

Results of the analysis are given in Table 16. The formulations 1T1B2 and 3T1B2 had exactly the same coating composition, but the welds were produced at depths of 70 and 200 ft (21 and 61 m) respectively. The effect of increased depth on the slag composition was mainly an increase in the iron oxide content of the slag, resulting in increased slag basicity. Both slag basicity and total pressure increase with depth. The adverse effect of increased total pressure on porosity content appears to outweigh any beneficial effect of the small increase in slag basicity.

Slag basicity was highest for the Task I (Fe-Mn) formulation, intermediate for the Task II (Ti-B) formulation, and least for the Task III (REM) formulation. The main effect of Ti-B addition was to increase the titanium oxide content and decrease the iron oxide content of the slag, which resulted in decreased slag basicity compared to the Fe-Mn formulation. The effect of REM addition was a further decrease in basicity due to a slightly higher titanium oxide content and slightly lower combined manganese and iron

oxide content compared to the Ti-B formulation. When porosity is plotted as a function of slag basicity, as seen in Figure 32, it can be seen that higher slag basicity is associated with lower levels of porosity. The trend is consistent with those presented in Figures 5-8, assuming that porosity can be taken as an indication of the initial hydrogen content of the weld pool. The data from the present investigation is not sufficient to solidly confirm the effect of slag basicity on porosity in wet welds; however, due to the presence of supporting data from the literature and the importance of porosity to the quality of wet welds, the concept is worthy of further investigation.

6.5 Effect of Deposition Technique on Chemical Composition and Porosity

When the method of depositing the test welds was switched from mechanical

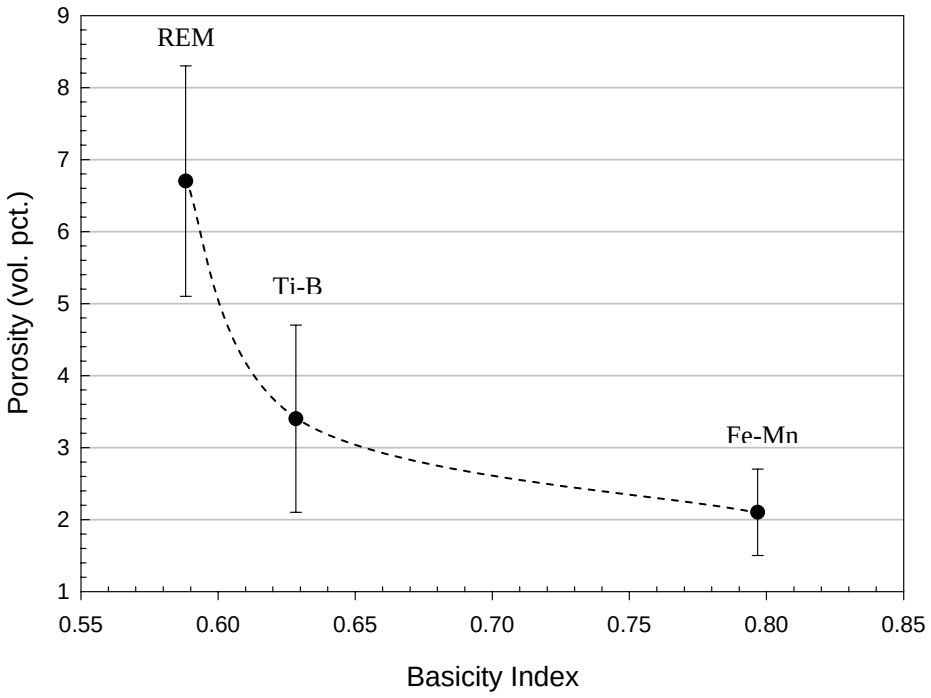

Figure 33: Effect of slag basicity on weld metal porosity content.

(gravity) to manual, a significant effect on the recoveries of boron and manganese was observed. In Table 3, the formulations labeled (T1B1) were deposited mechanically. The next set of formulations, appearing in boldface type, was deposited manually. For the same titanium addition, the boron recovery nearly doubled (approximately 0.2 to 0.4 pct. for 70 and 140 ft (21 and 43 m). The effect was somewhat less significant at 200 ft (61 m), but the boron recovery nearly doubled again at 300 ft (91 m). The manganese recovery at 70 and 140 ft (21 and 43 m) increased by approximately 1 pct. with the switch from mechanical to manual deposition, while the effect was minimal at 200 and 300 ft (61 and 91 m). In Table 10, the effects of the changes in recovery can be seen. For example, at 70 ft (21 m) 1T1B1 and 1T1B3 were formulated to give boron contents of 10 and 25 ppm with a manganese content of 0.7 wt. pct.; however, the result was 18 and 48 ppm boron with 0.86 and 0.91 wt. pct. manganese due to the increased recoveries.

A significant decrease in oxygen content can be seen at 140 and 200 ft (43 and 61 m) with the switch from mechanical to manual deposition. At 70 ft (21 m) there was a reduction in average oxygen, but the reduction was not greater than the 90 pct. confidence interval, and at 300 ft (91 m) there was a significant reduction in 4T1B2, but not in 4T1B3. There was also a tendency for porosity to decrease, especially at greater depths, with the change from mechanical to manual deposition. The increase in recoveries and porosity along with the decrease in oxygen content suggest that the weld pool is better protected from exposure to the water in the case of manual welding.

Porosity had a tendency to be higher for mechanically deposited welds than for manually deposited welds. The same trend was noted in Task I where the porosity levels of the V-groove welds, which were manually deposited, were much lower than the porosity levels of the test weld experiments, which were mechanically deposited, produced with the same formulations. This observation is consistent with increased exposure to the water (oxygen and hydrogen) which leads to lower elemental recovery due to oxidation and higher porosity due to hydrogen. A skilled diver/welder should be able to manipulate the electrode and maintain a short arc length more precisely than a

simple gravitational welding apparatus resulting in less exposure of the weld pool to oxygen and hydrogen.

Other factors that influence the ability of a diver/welder to manipulate the electrode effectively, such as arc stability and slag behavior, may also influence the exposure of the weld pool to water. The effect of increased exposure to the water is to increase the partial pressure of water vapor over the weld pool. The effects of increased partial pressure of water vapor should be similar to the effect of increasing depth. The partial pressure is the product of the mole fraction of water vapor and the total pressure. Partial pressure of water vapor increases with depth due to increasing total pressure, and the partial pressure can increase at a given depth due to increasing mole fraction of water vapor in the gas over the weld pool. The effects of increasing depth on wet welds are: increasing porosity, increasing oxygen content, and increasing slag basicity (due to increasing iron oxide content). It can be assumed that increasing exposure to water (increasing partial pressure of water vapor) at a given depth would have the same effects. The trend displayed in Figure 33 of decreasing porosity with increasing slag basicity is the opposite of what would be expected from increasing exposure to water. Slag basicity and porosity would both be expected to increase with increasing exposure to water. Therefore, the decrease in porosity with increasing slag basicity cannot directly be explained by variations in welder technique, which may lead to increased exposure to water.

6.6 Top Bead Microstructure

6.6.1 Task I: Increasing Ferro-Manganese Additions

Quantitative metallography of the top bead microstructure revealed a fairly constant microstructure as a function of ferro-manganese addition and depth over the range tested. Tables 7 and 8 contain results of the one-thousand point counts. Acicular

ferrite (AF) was typically between 5 and 15 pct., primary ferrite (PF) between 25 and 45 pct. and ferrite with second phase (FS) between 40 and 60 pct.. The constant microstructure with increasing ferro-manganese addition is consistent with the constant chemical composition shown in Figure 15.

In the baseline data there was a trend of increasing PF and decreasing FS with depth, as seen in Figure 34. Figure 35 shows that a more constant microstructure was produced in the Task I V-groove welds with optimized ferro-manganese levels. Macro and micrographs of the V-groove welds made with optimized ferro-manganese addition are shown in Figures 36-39.

6.6.2 Task II: Titanium-Boron Additions

The titanium-boron additions were expected to produce an increase in the acicular ferrite content of the top bead microstructure. Boron retards the nucleation of ferrite on the austenite grain boundaries allowing sufficient undercooling for intra-granular nucleation of ferrite to occur. Titanium protects boron from oxidation and produces a fine distribution of titanium oxide inclusions, which provide sites for the nucleation of acicular ferrite. Results of the quantitative metallography are given in Table 10-11. The typical microstructure of the Task I welds consisted of 25-40 pct. PF, 40-60 pct. FS, and 10-20 pct. AF. In the Task II test welds, microstructures containing 60-80 pct. AF were produced at all four depths.

The top bead microstructures of the Task II V-grrove welds are displayed in Figure 40. The acicular ferrite content of the Task II V-groove welds is significantly greater than the Task I V-groove welds, as seen in Figure 41. A substantial increase in the acicular ferrite content was achieved by adding titanium and boron. Figures 42-45 show the macro-sections and top-bead microstructures from the four V-groove welds. Note the large fraction of acicular ferrite in the top bead microstructures.

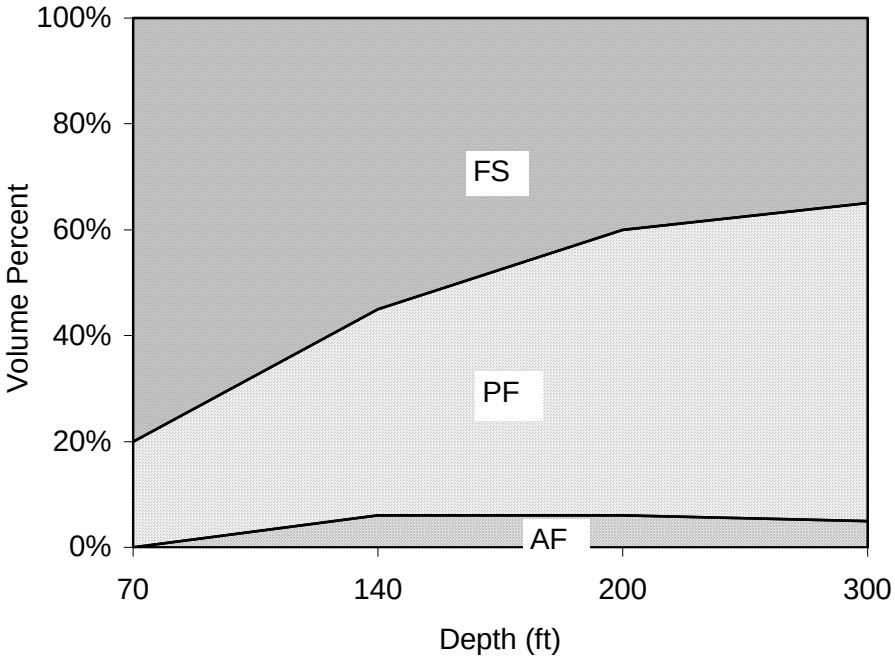

Figure 34: Top bead microstructure of the baseline electrode as a function of depth

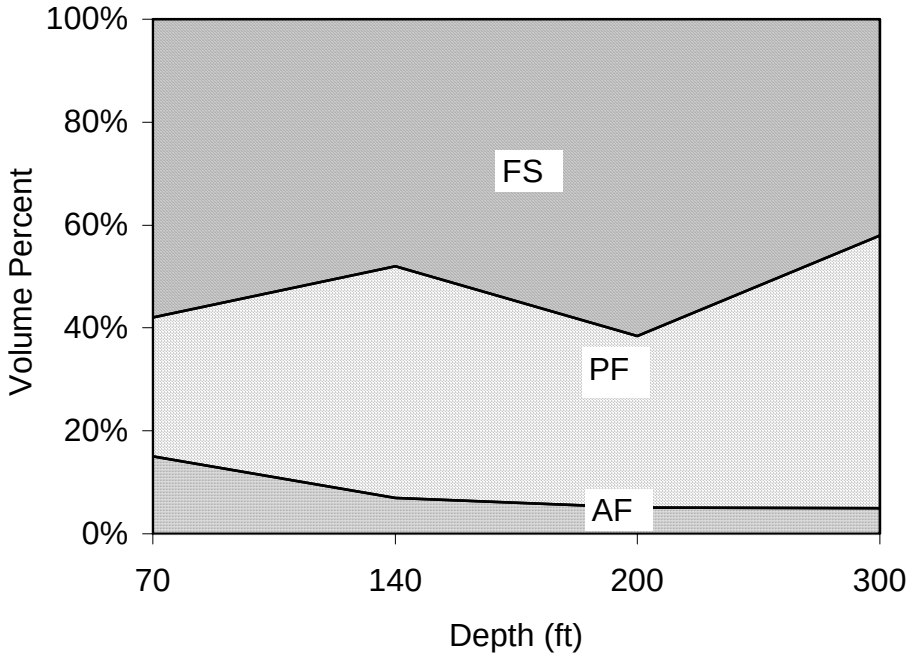

Figure 35: Top bead microstructure of the Task I V-groove welds as a function of depth.

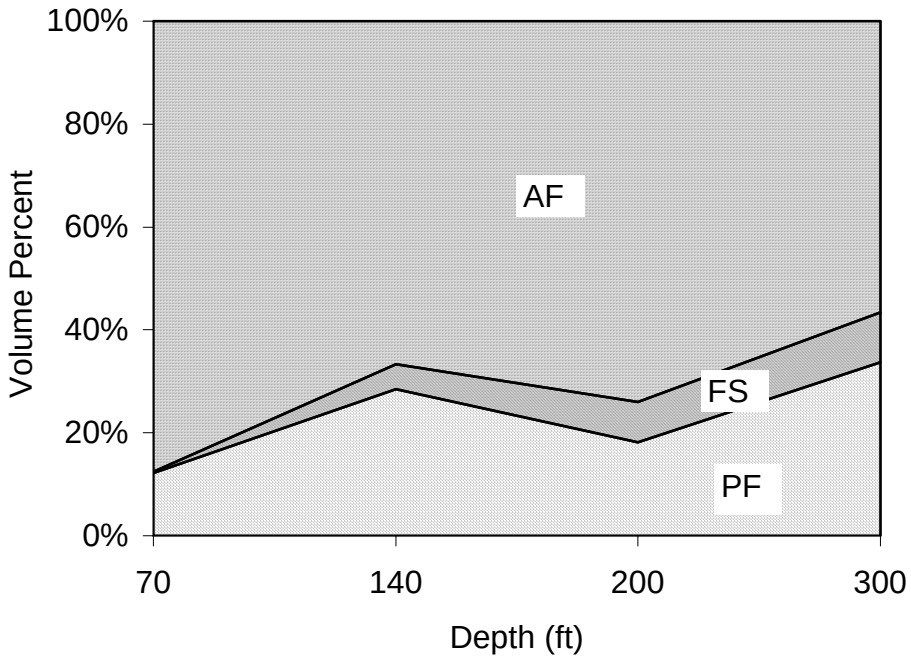

Figure 40: Top bead microstructure as a function of depth for Task II (Ti-B) V-groove welds.

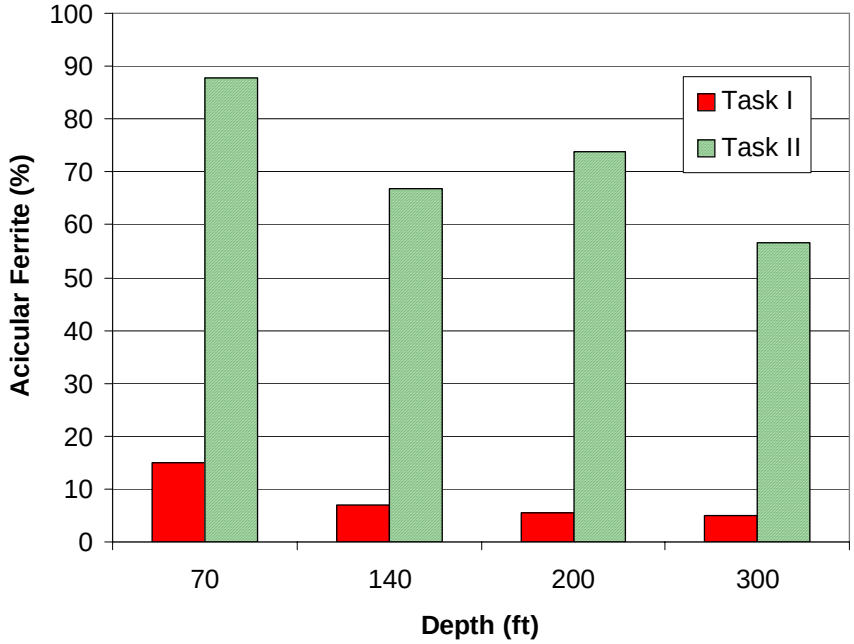

Figure 41: Acicular ferrite content of the top bead microstructure from Task IB and Task IIB V-groove welds.

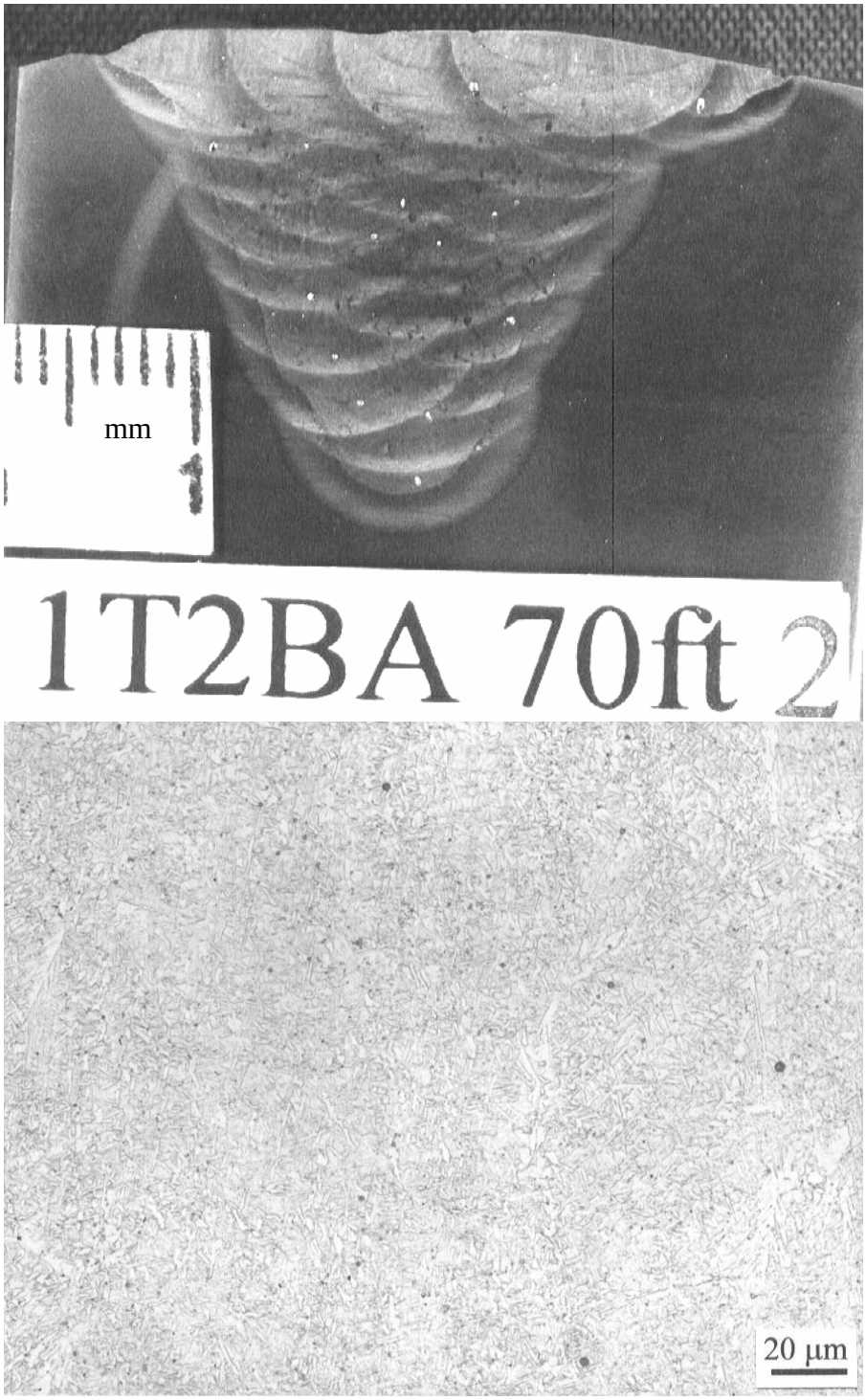

Figure 42: Macro-section and top bead microstructure from 1T2B2 V-groove weld.

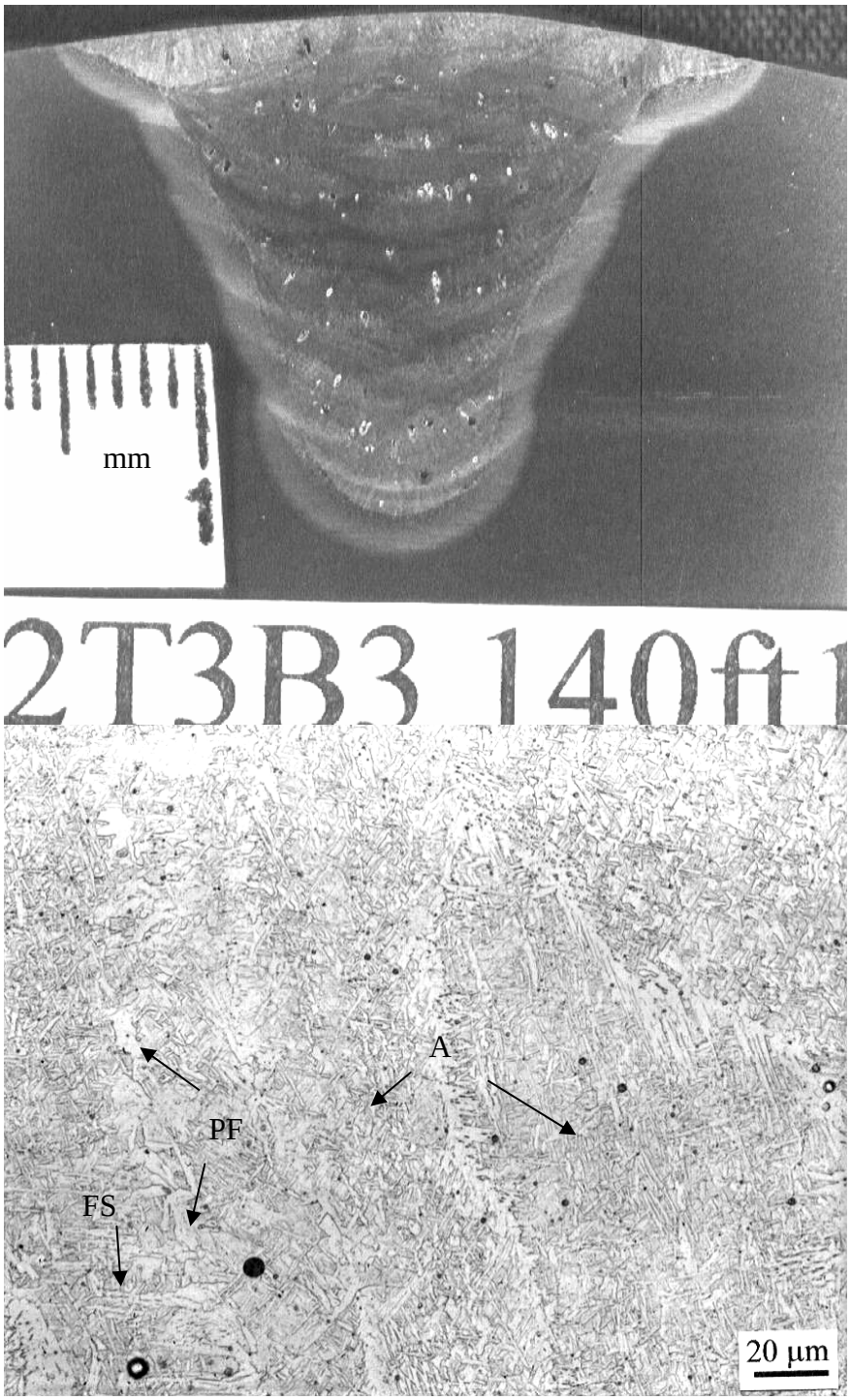

Figure 43: Macro-section and top bead microstructure from 2T3B3 V-groove weld

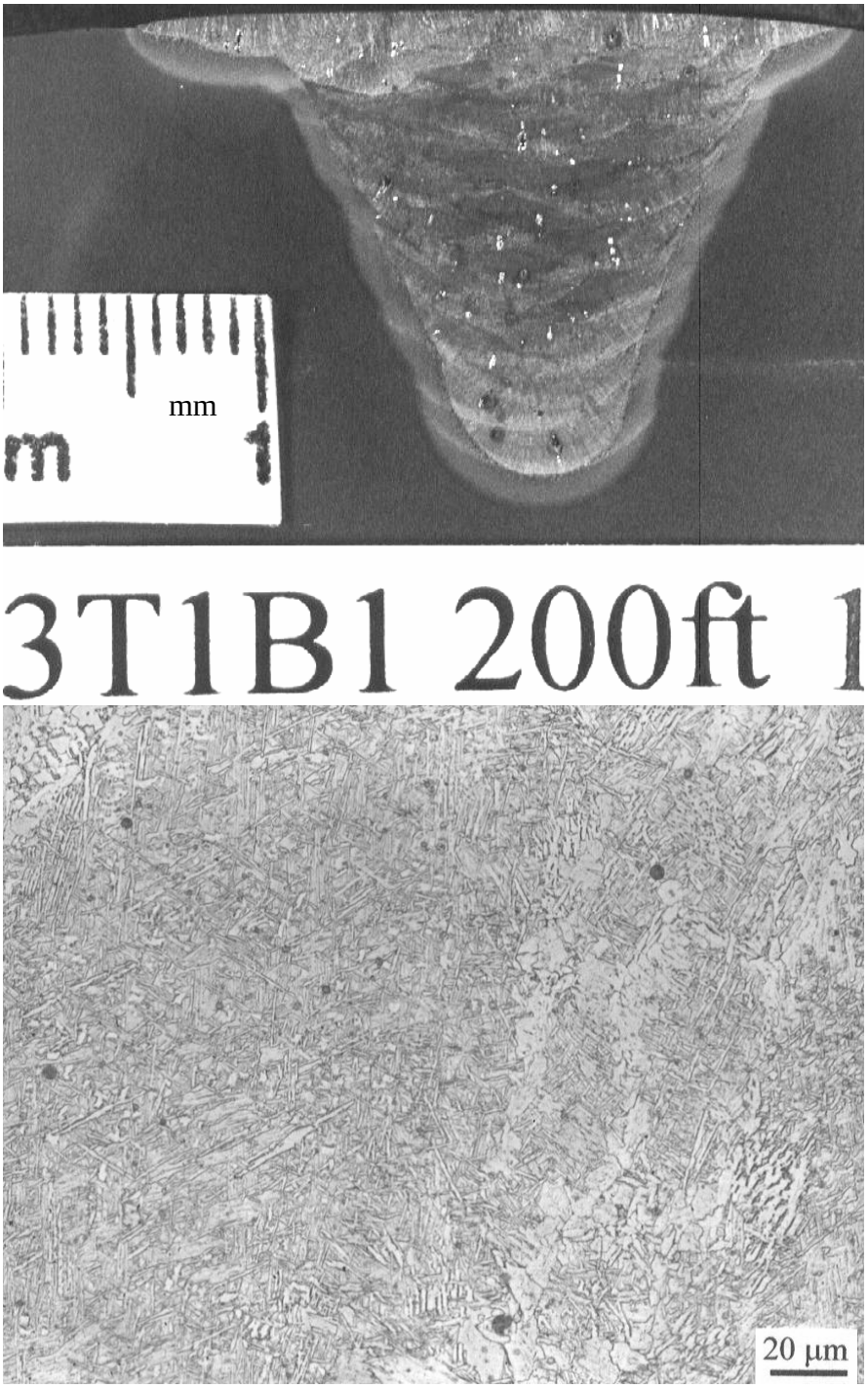

Figure 44: Macro-section and top bead microstructure from 3T1B1 V-groove weld.

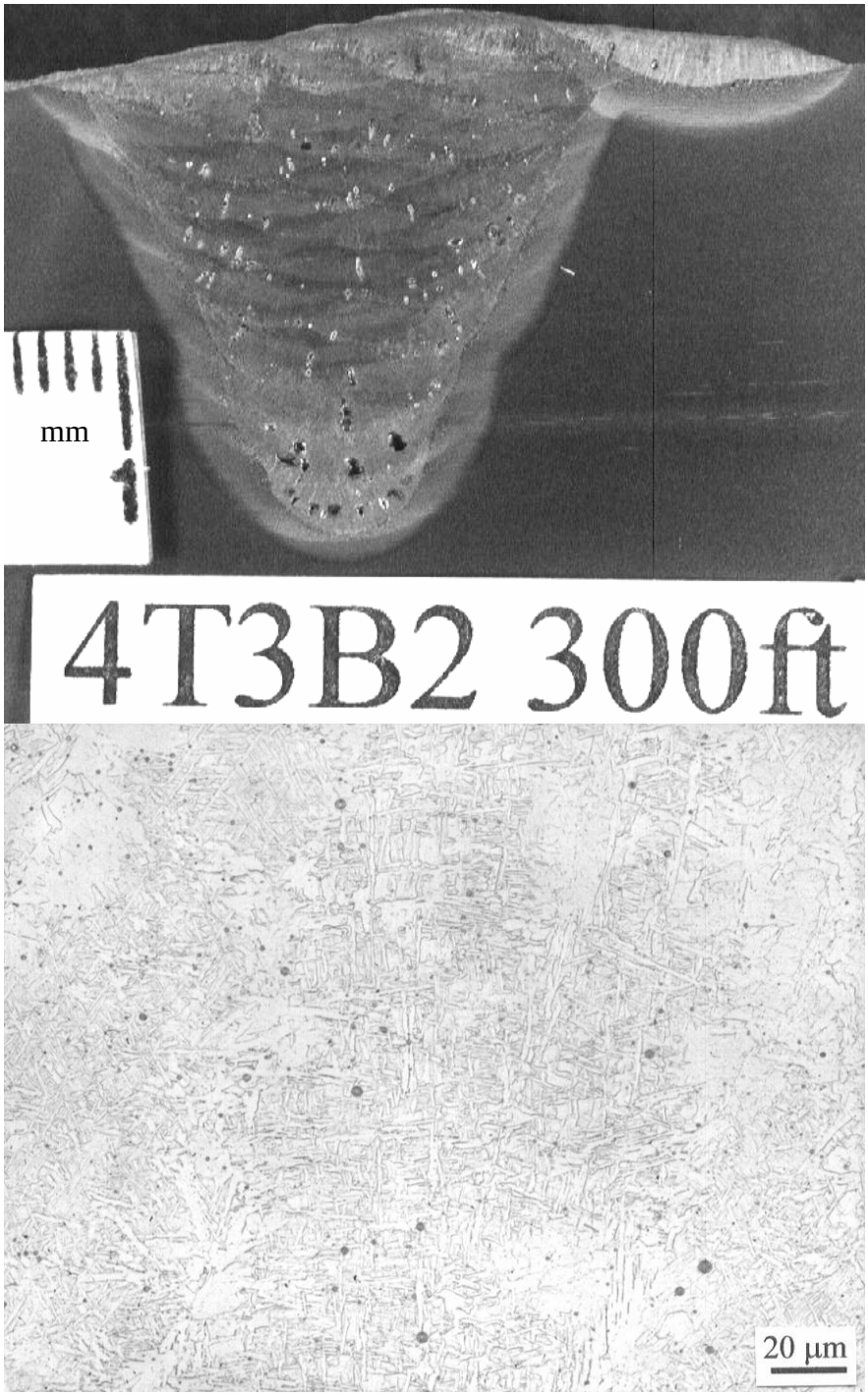

Figure 45: Macro-section and top bead microstructure from 4T3B2 V-groove weld.

6.6.3 Task III: Rare Earth Metal Additions

The REM additions were expected to reduce the weld metal oxygen content and increase the recoveries of the alloying elements. More precise control over the chemical composition should allow more precise control over the microstrucure; however, as was mentioned in section 6.2.3, the REM additions actually produced higher oxygen contents and lower recoveries than the Task I and Task II additions. Furthermore, it was not known if the formation of REM-rich oxide inclusions would interfere with the nucleation of acicular ferrite on titanium-rich inclusions.

The top-bead microstructures of the Task III V-groove welds are given in Figure 46. A microstructure high in AF was produced at depths to 200 ft (61 m) despite the higher oxygen contents and lower alloy recoveries than anticipated. Cross-sections and top bead microstructures of the Task III V-groove welds are presented in Figures 47-50. It is apparent that the AF content of the top bead microstructures is significantly greater than those of the Task I (Fe-Mn) V-groove welds shown in Figures 36-39. The ability of the REM consumables to produce a microstructure high in AF indicates that the microstructure of wet welding consumables with Ti-B additions are fairly tolerant of variations in chemical composition and the degree of oxidation of the weld metal.

6.7 Task IV: Reheated Microstructure

From the macro-sections shown in section 6.6, it can be seen that the fraction of reheated microstructure in the multipass welds is high; therefore, the mechanical properties are expected to be influenced by the reheated microstructure. It is important to determine whether refinement of the as-deposited microstructure leads to refinement of the reheated microstructure through a memory effect.

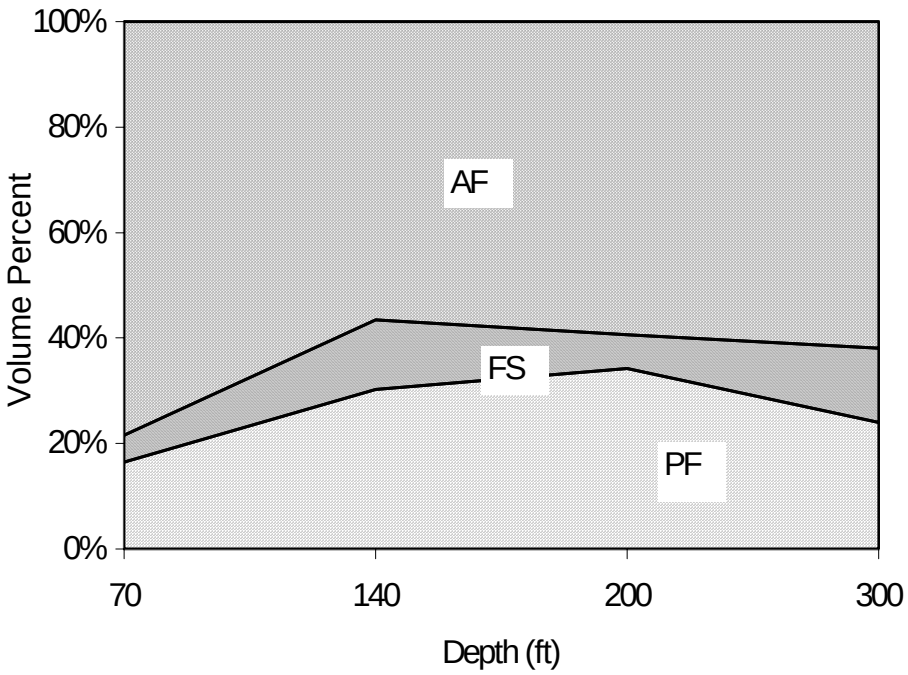

Figure 46: Top bead microstructure as a function of depth for Task III (REM) V-groove welds.

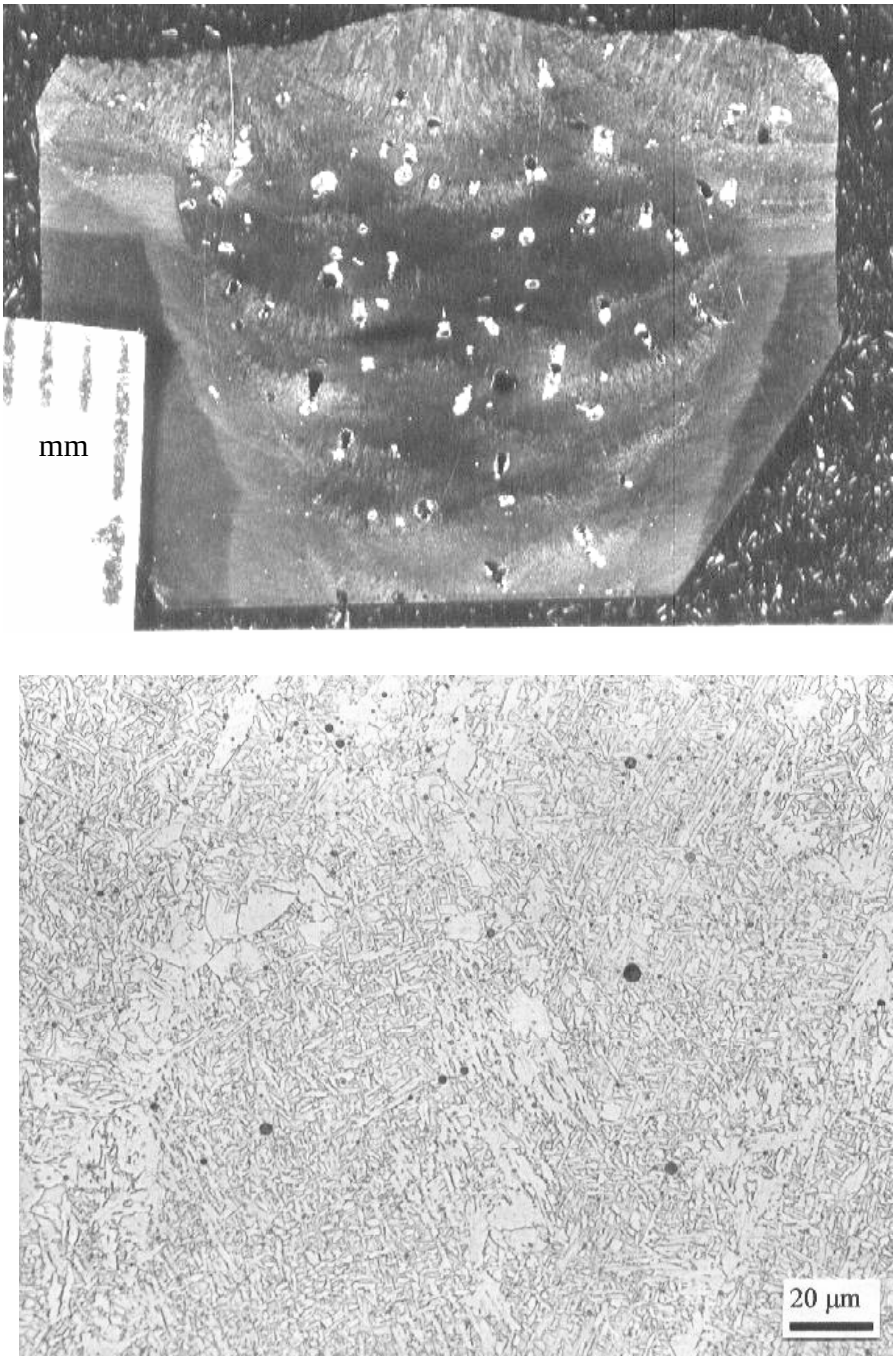

Figure 47: Macro-section and top bead microstructure from 1R1 V-groove weld.

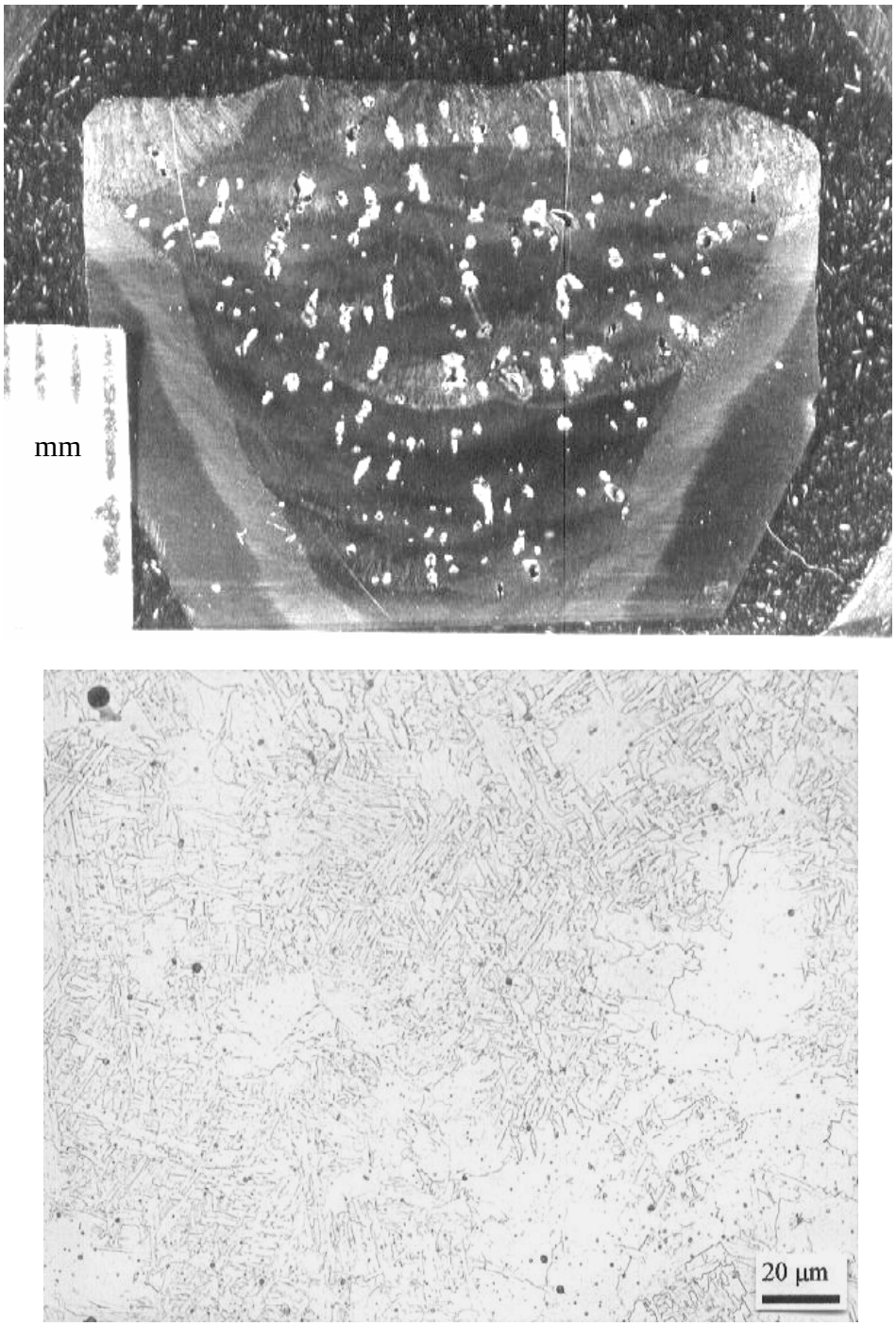

Figure 48: Macro-section and top bead microstructure from 2R1 V-groove weld.

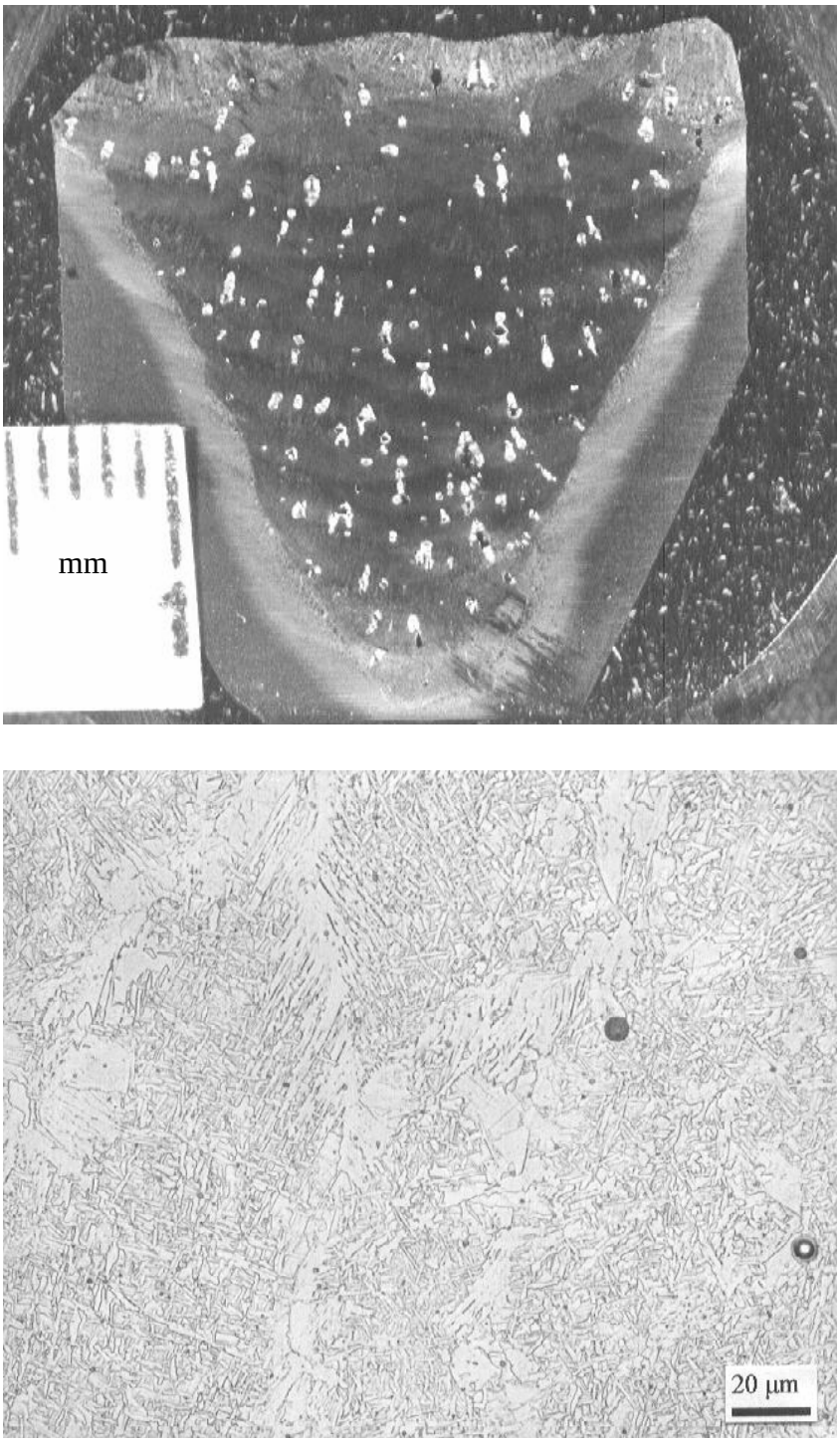

Figure 49: Macro-section and top bead microstructure from 3R1 V-groove weld.

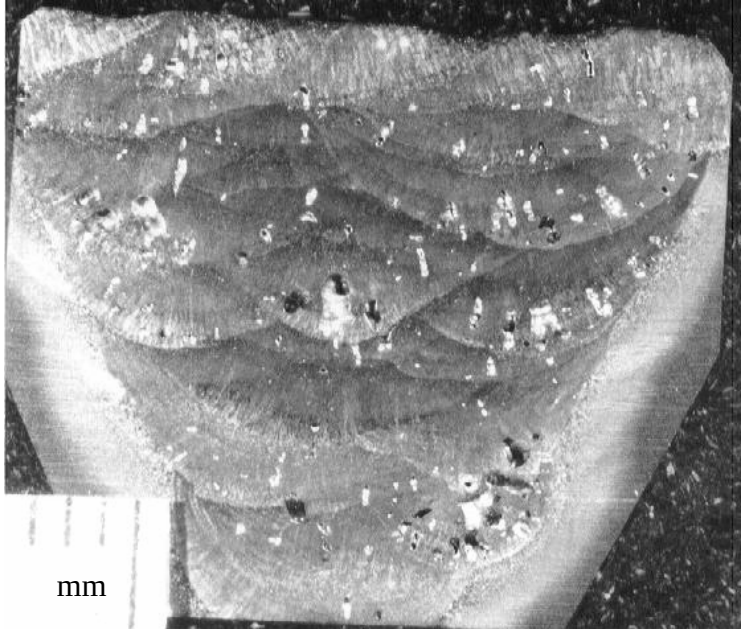

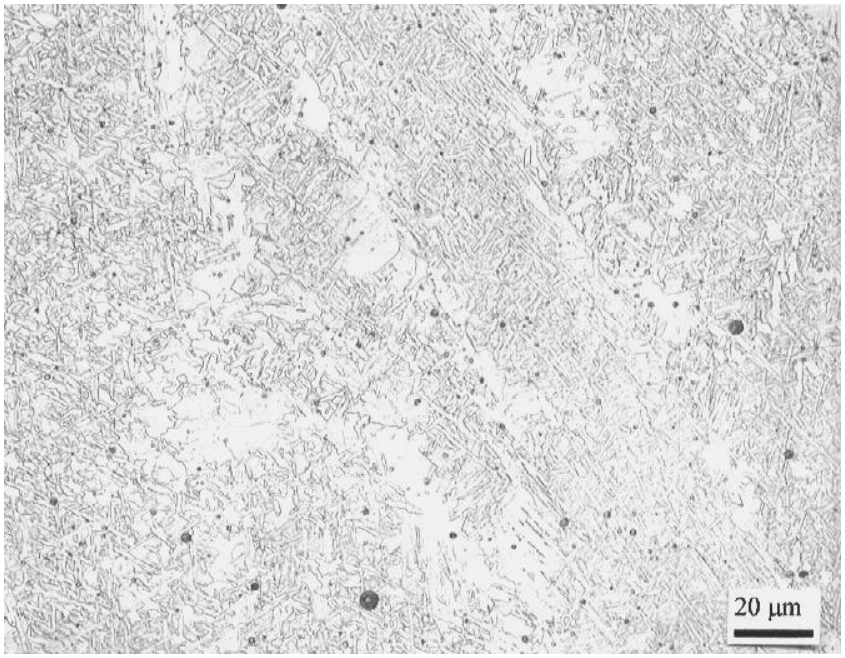

Figure 50: Macro-section and top bead microstructure from 4R1 V-groove weld.

6.7.1 Effect of Titanium-Boron addition on Reheated Microstructures

Significant microstructural refinement occurred in the coarse-grained reheated zone (CGRHZ) due to the titanium-boron additions. The CGRHZ is heated high into the austenite phase field, and significant austenite grain growth results. On cooling, the austenite transforms back to ferrite. In the Task I welds, hardenability was low, and the result was a microstructure of coarse PF with a small amount of FS, as seen in Figures 51-52 in the upper right. In welds with titanium-boron addition, the microstructure in the CGRHZ consisted of a much smaller amount of PF on the prior-austenite grain boundaries, and intragranular AF and FS, as seen in Figures 51-52 in the upper left. Boron inhibited the nucleation of PF at the prior-austenite grain boundaries, while titanium-rich oxide inclusions provided intragranular nucleation sites for AF. Titanium addition also increased the recovery of manganese. Higher manganese contents increase hardenability and promote intragranular nucleation of ferrite. The result was a much finer ferrite microstructure in the CGRHZ for Task II welds with titanium-boron additions compared to Task I welds with ferro-manganese additions only.

Microstructural refinement was also apparent in the fine-grained reheated zone (FGRHZ), although not to the same extent as in the CGRHZ, as seen in Figures 51-52 at bottom. The FGRHZ is heated to low temperatures in the austenite phase field where there is little opportunity for austenite grain growth. The grain size in the FGRHZ is related to the as-deposited microstructure from which it originated. Refinement occurred due to the finer as-deposited microstructure in the titanium-boron welds.

6.7.2 Effect of REM Addition on Reheated Microstructures

Addition of REM to titanium-boron containing formulations reduced the recoveries of alloying elements, as discussed in section 6.2.3. The manganese content of the REM V-groove weld at 70 ft (21 m) was less than that of the titanium-boron

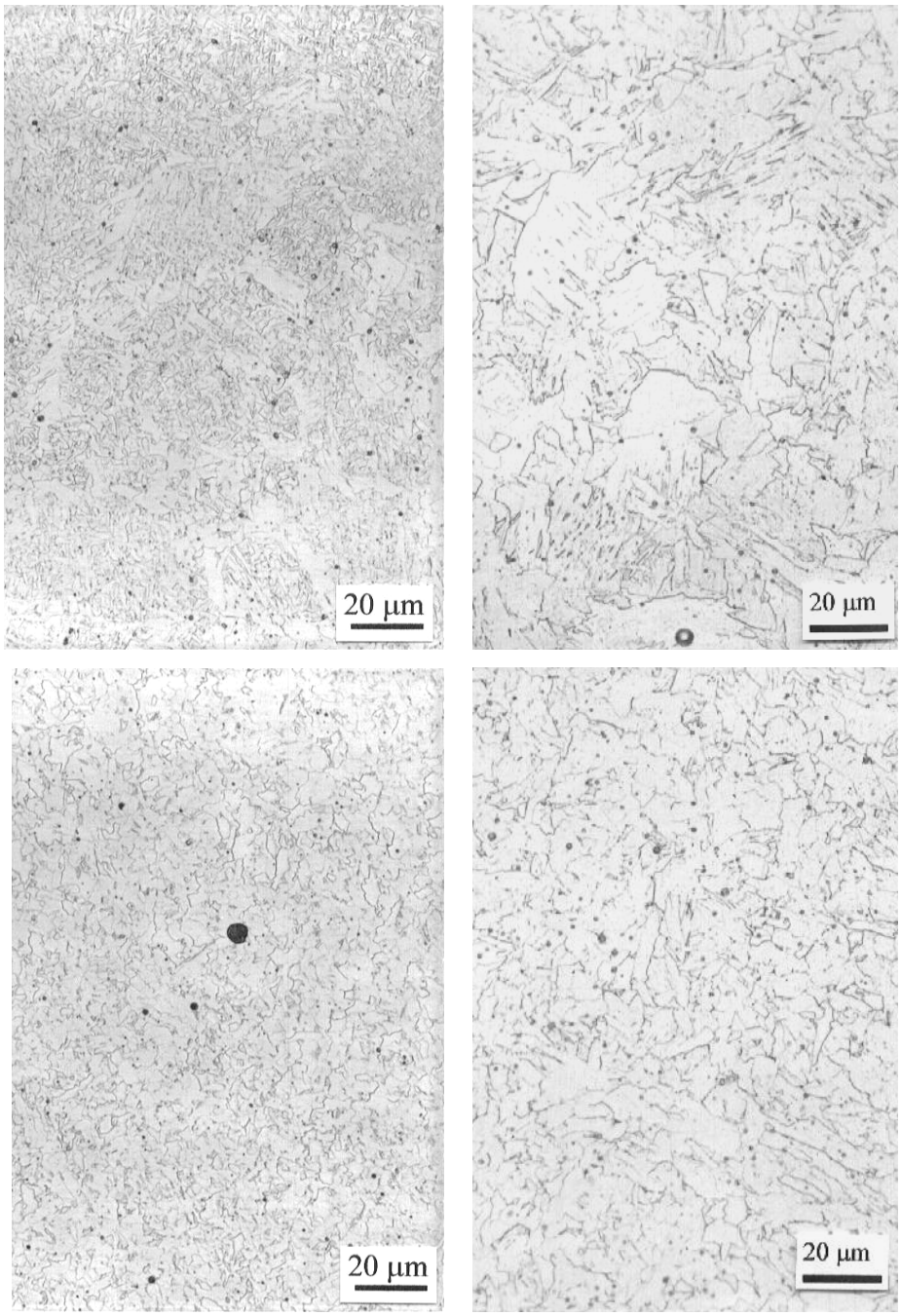

Figure 51: Reheated steel weld metal microstructures from 1T2B2 (left) and 1F3 (right) V-groove welds. The coarse-grained reheated zone appears at top, the fine-grained reheated zone appears in the bottom two photomicrographs.

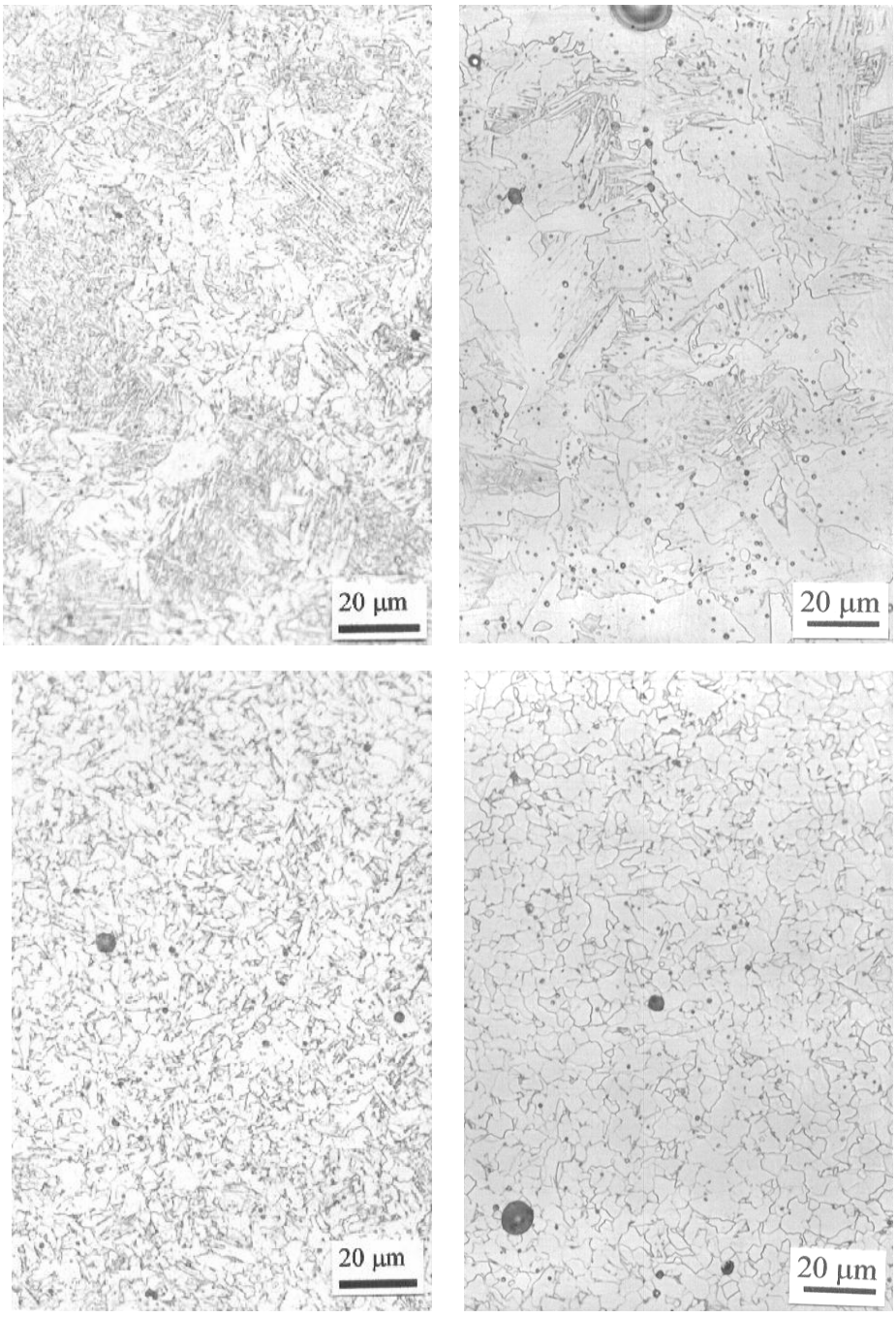

Figure 52: Reheated steel weld metal microstructures from 3T1B1 (left) and 3F3 (right) V-groove welds. The coarse-grained reheated zone appears at top, the fine-grained reheated zone appears in the bottom two photomicrographs.

V-groove weld, as indicated in Tables 11 and 14. The boron content of the REM containing weld was also less. The result is reheated microstructures in the REM welds which appear to have a more coarse ferrite grain size than those of the titanium-boron welds.

Comparing the CGRHZ microstructures shown in Figure 53, there appears to be more coarse primary ferrite in the microstructure from the REM containing weld than in the microstructure from the titanium-boron weld. The FGRHZ ferrite grain size of the REM containing weld also appears to be more coarse than that of the titanium-boron weld.

Figure 54 compares the reheated microstructures of Task II (titanium-boron) and Task III (REM) containing welds at a depth of 200 ft (61 m). The manganese contents of the REM and titanium-boron containing welds shown in Figure 54 are nearly the same. The ferrite grain sizes in both regions of the reheated zone also appear to be similar between the two welds. The boron content of the REM containing weld is slightly less than that of the titanium-boron weld. The difference in boron contents does not appear to have made a significant difference in the ferrite grain size of the two welds.

6.7.3 Ferrite Grain Size of the Reheated Weld Metal

In order to quantify the effect of the ferro-alloy additions on the reheated microstructure, the average ferrite grain size of the reheated weld metal was measured with an image analyzer. The average linear intercept grain size was measured on least fifteen fields from each weld at a magnification of 500x. The grain size varies significantly from the CGRHZ to the FGRHZ within a given weld. The average grain size was measured by making a traverse of five fields from the CGRHZ to the FGRHZ of the top bead. Three such traverses were made for a total of fifteen fields, and the average of the fifteen measurements along with the 90 pct. confidence interval were reported.

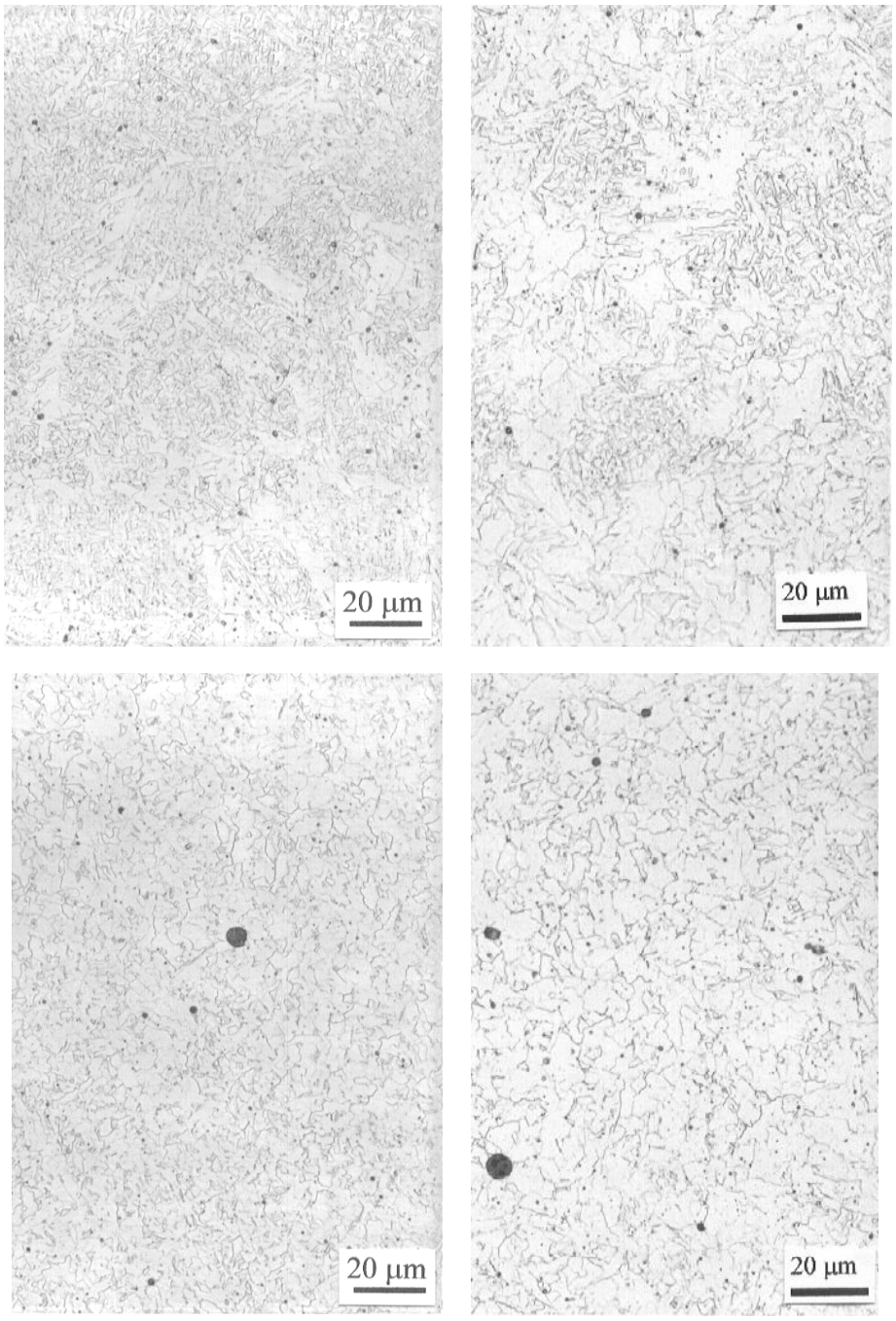

Figure 53: Reheated steel weld metal microstructures from 1T2B2 (left) and 1R1 (right) V-groove welds. The coarse-grained reheated zone appears at top, the fine-grained reheated zone appears in the bottom two photomicrographs.

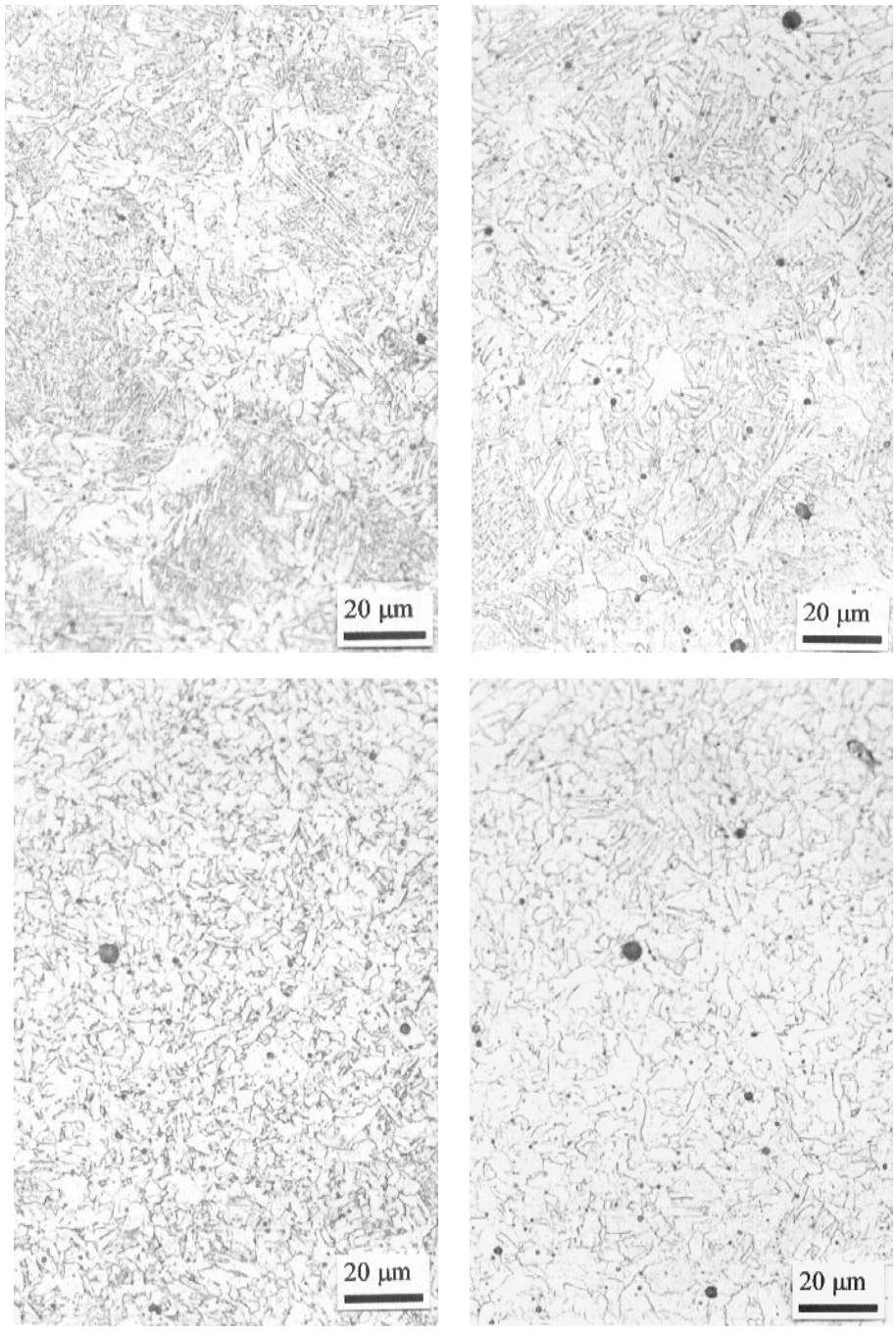

Figure 54: Reheated steel weld metal microstructures from 3T1B1 (left) and 3R1 (right) V-groove welds. The coarse-grained reheated zone appears at top, the fine-grained reheated zone appears in the bottom two photomicrographs.

The results for six selected V-groove welds are presented in Figure 55. The finest ferrite grain size occurred in the titanium-boron containing welds, while the ferro-manganese and REM containing welds had a more coarse ferrite grain size in the reheated weld metal. The grain size data is plotted as a function of hardenability in Figure 56. Higher hardenability promotes a finer ferrite grain size in the reheated weld metal, as discussed in section 2.2.1. A modified version of the Pcm expression, which takes into account the effect of oxygen was proposed by Onsoien et al (1996) for hardenability of steel weld metal. Onsoien et al found that a factor of –0.75 for oxygen gave the best correlation in the range 275-450 ppm oxygen. In the present investigation, weld metal oxygen contents are much higher, and the best correlation occurs with a factor of –0.4 for oxygen.

The Hall-Petch equation [6.12] is commonly used to correlate yield strength to grain size.

$$\sigma_y = \sigma_o + k_y d^{-\frac{1}{2}} \qquad [6.12]$$

σ_y = yield strength

σ_o = frictional stress required to move dislocations through the matrix

k_y = Hall-Petch slope

d = grain diameter

The yield strength of the six V-groove welds is plotted as a function of the inverse square root of the reheated weld metal ferrite grain size in Figure 57. There is an increasing trend in yield strength with the grain size parameter. Higher hardenability produces finer grain size, as indicated in Figure 56, thus the trend of increasing strength

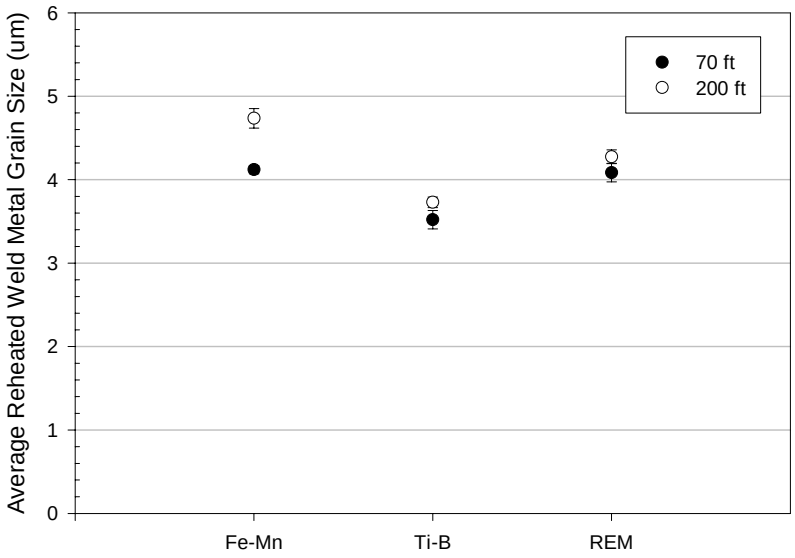

Figure 55: Effect of ferro-alloy addition and depth on ferrite grain size in the reheated weld metal of selected V-groove welds.

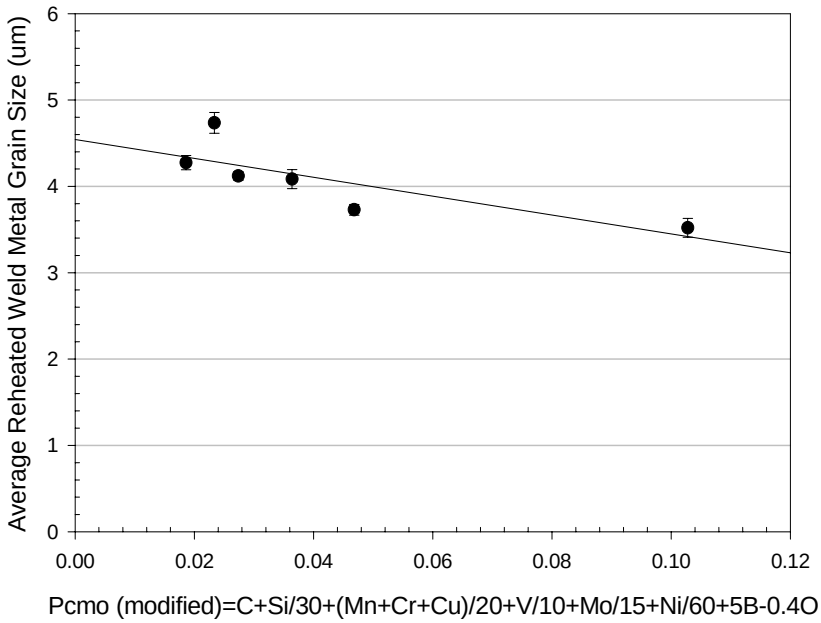

Figure 56: Effect of hardenability, given by a modified form of the Pcmo expression (Onsoien et al 1996), on ferrite grain size in the reheated weld metal for the same six welds presented in Figure 54.

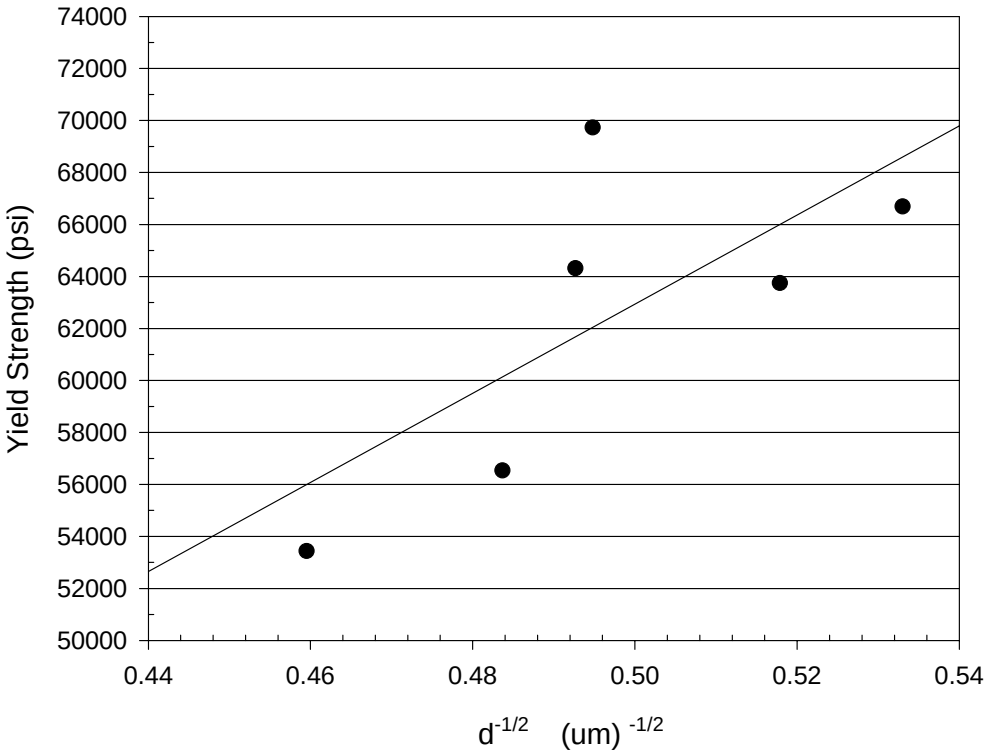

Figure 57: The six V-groove welds from Figure 41 are plotted to show the influence of grain refinement in the reheated weld metal on yield strength according to the Hall-Petch relation. "d" is the average linear intercept grain diameter in microns.

in Figure 57 is a result of the combined effects of reduced grain size and solid solution strengthening. Other factors would also affect the yield strength, such as the fraction of reheated weld metal, the as-deposited microstructure, and the porosity content. The fact that a reasonable trend exists indicates that the ferrite grain size of the reheated weld metal is an important parameter in determining the strength of underwater wet welds.

6.8 Micro-Cracking

Micro-cracking was observed to some extent in all of the Task I, II, and III welds. Examples of micro-cracking can be seen in Figure 58. It is not known how this type of micro-cracking influences the mechanical properties of wet welds.

A similar type of cracking has been reported in the literature by Allen et al (1982) and Mota and Apps (1982). This type of cracking has been referred to as “chevron cracking” in its more severe form, or “micro-fissuring” in its less severe form. The cracking is caused by hydrogen in combination with the residual stress from welding (Allen et al 1982) (Mota and Apps 1982). Mota and Apps reported that the cracking tends to occur when the cooling rate below the transformation temperatures is high, and that the cracking can be eliminated by hydrogen control. It is not surprising that underwater wet welds suffer from this type of cracking due to the high hydrogen content and high cooling rates involved. In contrast to traditional views of hydrogen cracking, micro-fissuring has a tendency to occur in low-hardness microstructures, such as grain-boundary ferrite (Mota and Apps 1982).

Analysis of fracture surfaces from a bend-test specimen and a Charpy bar indicate that micro-cracks may be one of the features limiting the ductility of underwater wet welds. Figure 59 shows a feature from the bend-test fracture surface which strongly resembles the fractographic appearance of the micro-fissuring reported by Allen et al (1982) and Mota and Apps (1982). The central region appears to be a micro-crack which occurred in the primary weld metal, and was then reheated by the subsequent weld pass.

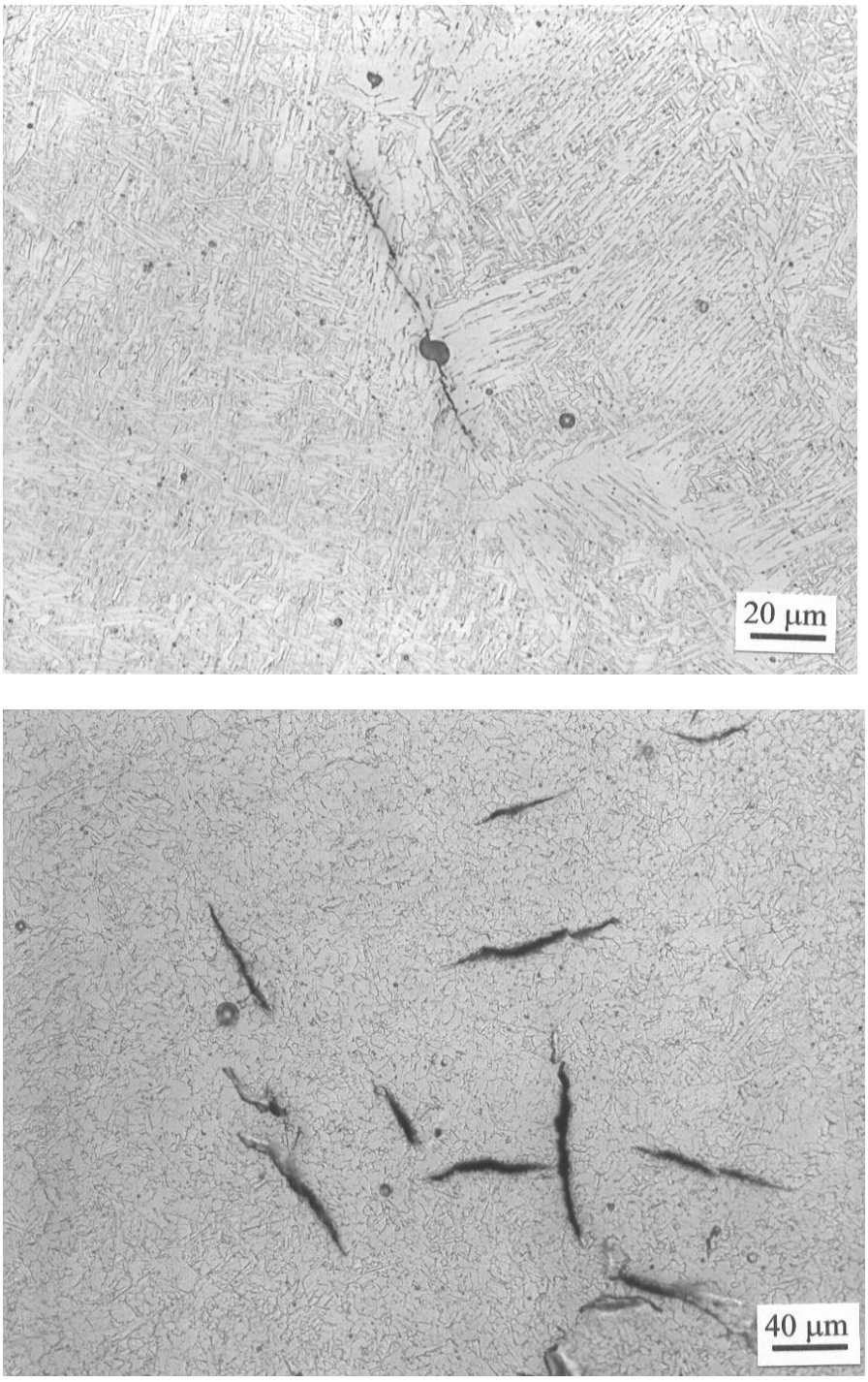

Figure 58: Micro-cracking in 1F3 as-deposited weld metal (top) and 2F3 reheated weld metal (bottom).

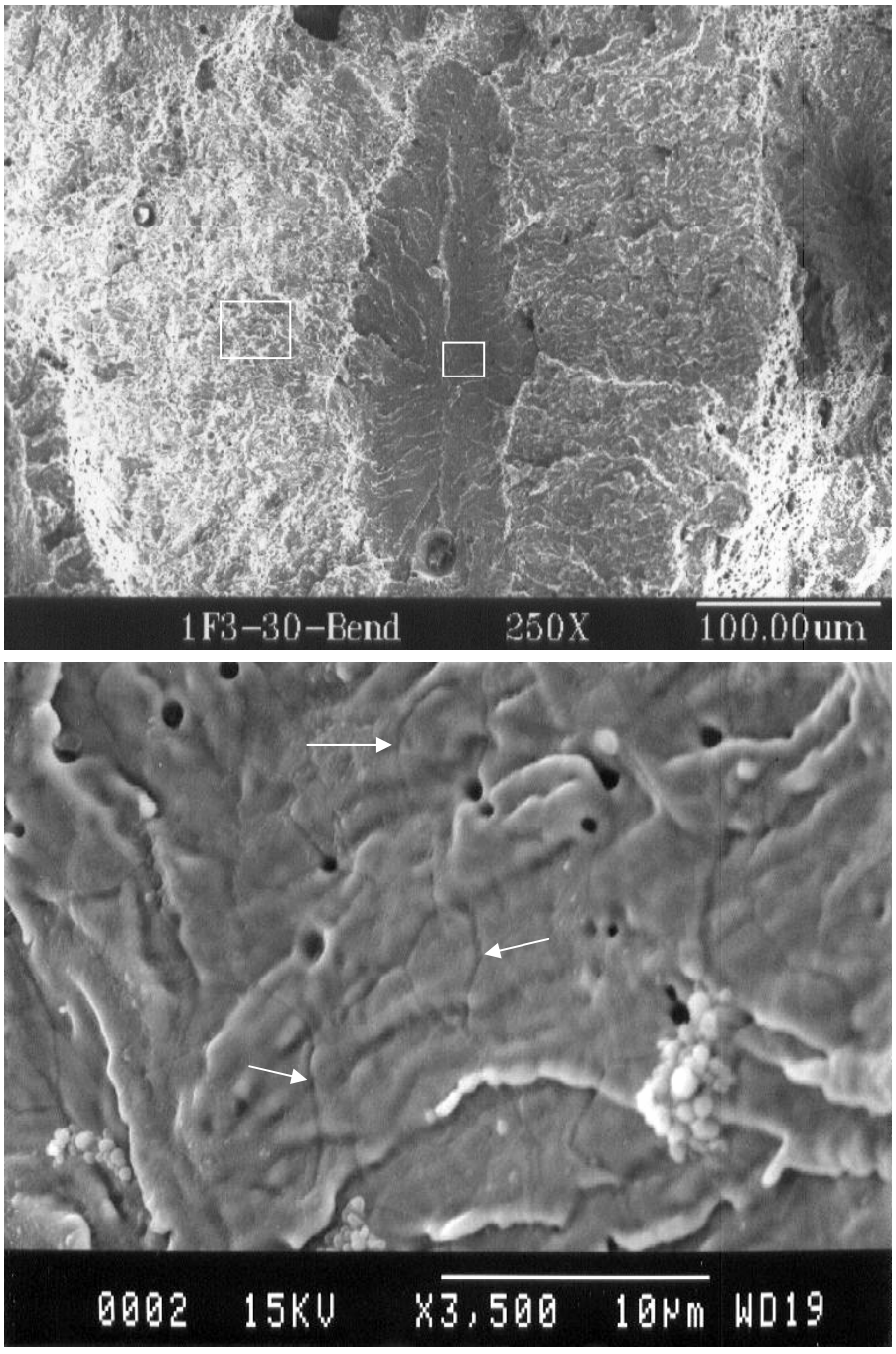

Figure 59: A micro-crack initiated brittle cleavage on the fracture surface of a bend-test specimen from a 1F3 V-groove weld. Top: the micro-crack (central region) propagated initially by brittle cleavage before changing to ductile void coalescence. Bottom: Thermal grooving (arrows) is visible in a high magnification view of the central region from above (white box).

The metallographic appearance of the micro-crack would be similar to the cracks shown in Figure 58. The metallographic appearance would initially resemble the crack in primary weld metal shown in Figure 58, above. After being reheated by the subsequent weld pass, the appearance would be similar to the cracks shown in Figure 58, below.

According to Allen et al (1982), thermal grooving appears on the fracture surface of a micro-crack when it is reheated by a subsequent weld pass. Thermal grooving occurs due to the interaction of grain boundaries with the free surface at high temperatures. Thermal grooving is pointed out by the arrows in Figure 59, below. The presence of thermal grooving on the fracture surface indicates that the central region was present in the primary weld metal and was then reheated by the subsequent weld pass. When the bend-test was performed, the micro-crack propagated initially by a brittle cleavage mechanism, then by ductile void coalescence. A high magnification view of the material which fractured by cleavage can be seen in Figure 60. The cleavage facet size, the thermal groove spacing, and the reheated weld metal grain size are all in the range of 3-5 microns in size, indicating that both phenomena occurred in association with the reheated microstructure. The initial propagation by cleavage may have occurred due to hydrogen embrittlement. The four conditions for hydrogen embrittlement; a sufficient concentration of hydrogen, a susceptible material, tensile stress, and a temperature between –100 and +100 °C should have been satisfied. In addition, a bend test is performed at a relatively slow strain rate, which allows hydrogen embrittlement to occur.

Figure 61 shows another location on the bend-test fracture surface where a micro-crack propagated initially by brittle cleavage. In Figure 61 the initial crack was oriented perpendicular to the bend-test fracture surface. The orientation of the micro-cracks shown in Figures 59 and 61 with respect to the applied stress is shown schematically in Figure 62.

Figure 63 shows a cleavage feature from the fracture surface of a 3F3 Charpy bar. The cleavage feature shown in Figure 63 may be a pre-existing micro-crack, but no evidence of thermal grooving was found. The presence of thermal grooving would

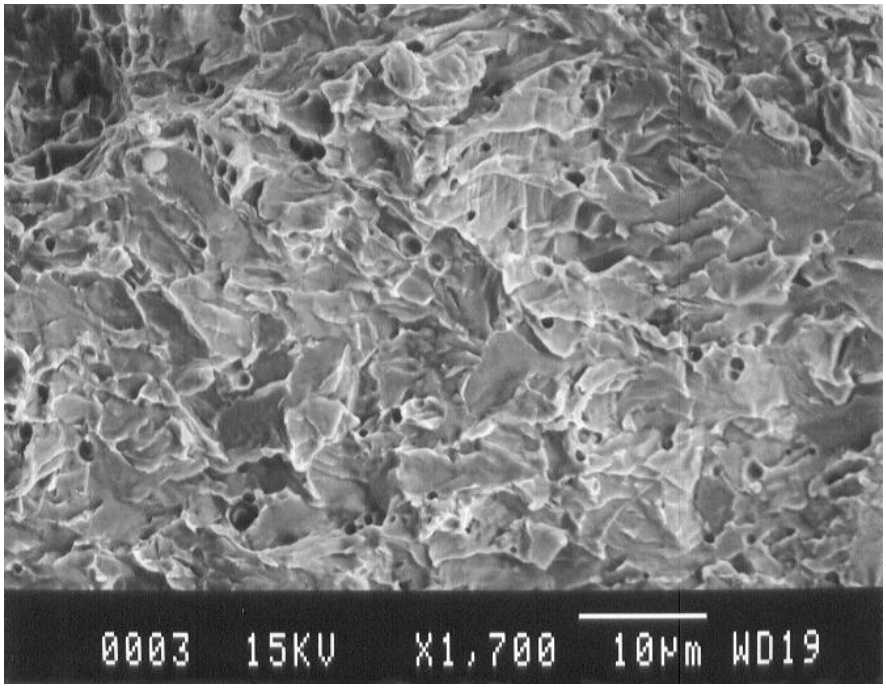

Figure 60: Brittle cleavage in the region adjacent to the central feature in Figure 58 (left box)

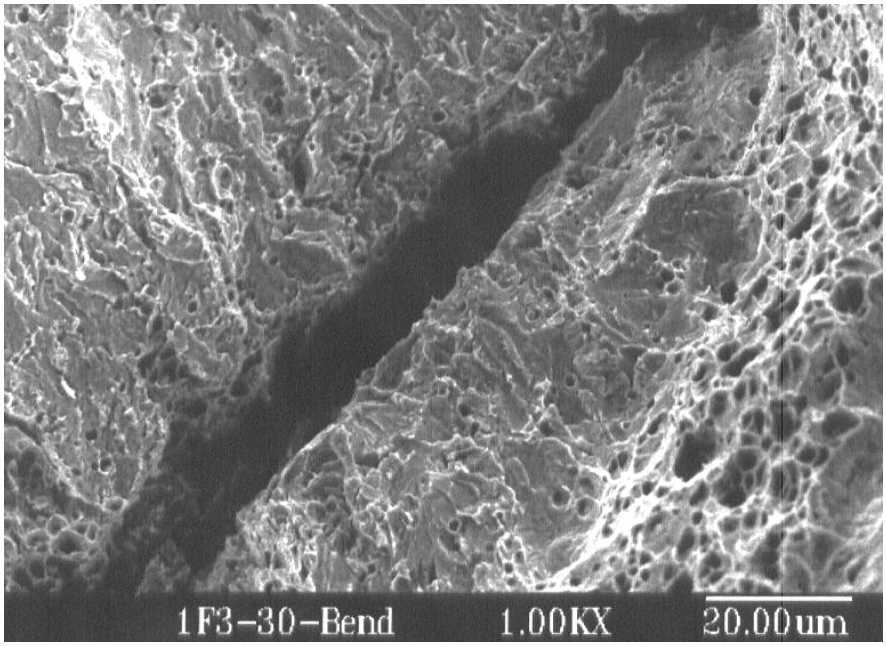

Figure 61: A micro-crack oriented perpendicular to the bend-test fracture surface acting as an initiation point for brittle fracture.

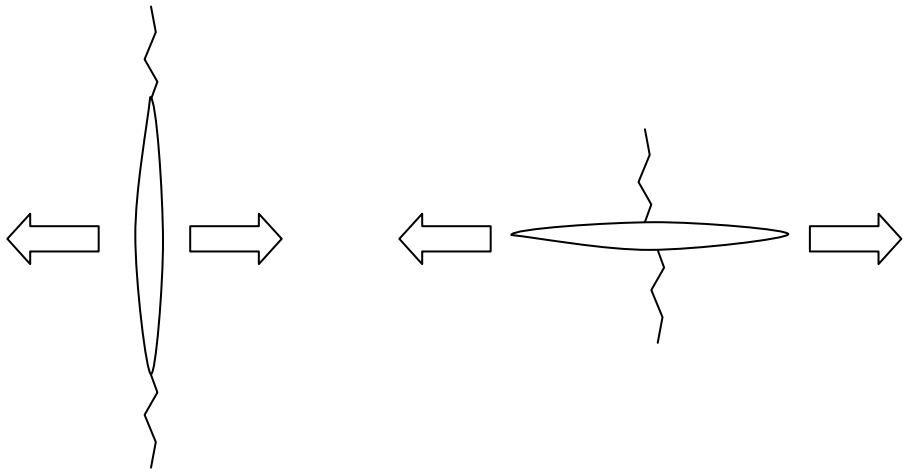

Figure 62: The arrows indicate the direction of applied load in the bend test with respect to the orientation of the pre-existing micro-cracks shown in Figure 58 (left) and Figure 60 (right). The jagged lines indicate the direction of initial propagation by cleavage during the bend test.

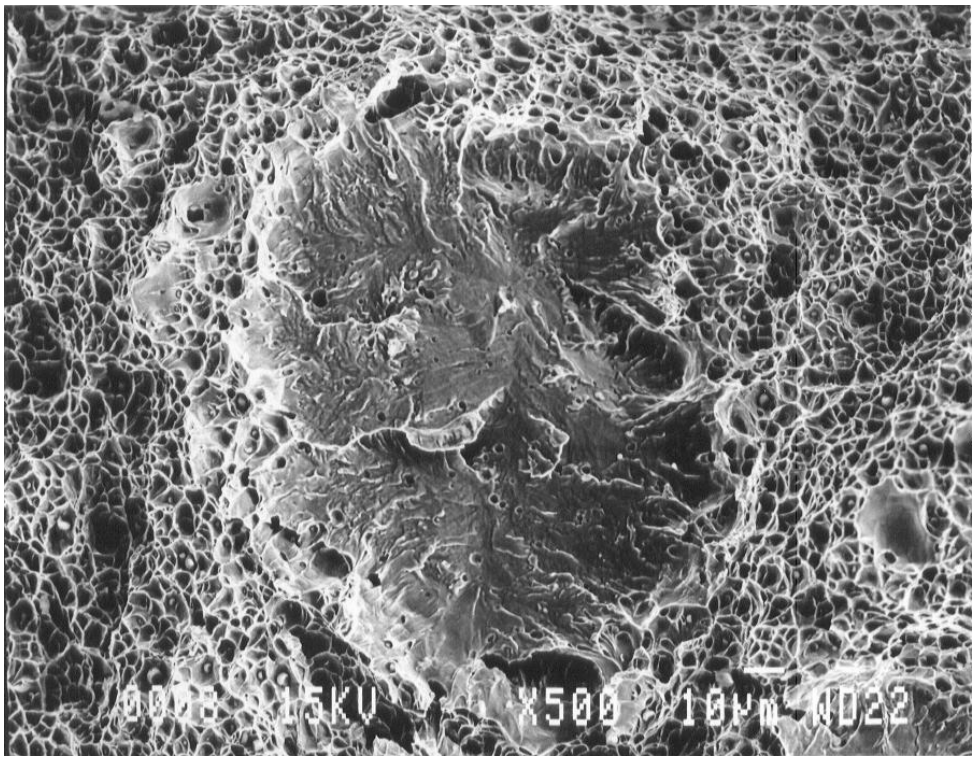

Figure 63: A possible micro-crack appearing on the fracture surface of a 3F3 Charpy bar.

confirm that the crack was present before the Charpy bar was broken. The absence of thermal grooving does not necessarily exclude the possibility that the crack was occurred during welding. Some micro-cracks may not have been reheated to a high enough temperature to exhibit thermal grooving.

Features such as the one shown in Figure 59 were not found on either of the two Charpy bars inspected. Such features were quite common on the bend-test fracture surface. In the case of the bend-test, the slower strain rate allowed micro-cracks to propagate initially by hydrogen induced cracking. In the case of the Charpy bar, the high strain rate prevented initial propagation by hydrogen embrittlement.

Based on inspection of fracture surfaces from the bend-test specimen and the Charpy bars, it appears that the micro-cracking may be one of the factors which limits the ductility of wet welds. Many features like the ones shown in Figures 59 and 61 were observed on the bend-test fracture surface, indicating that micro-cracks are one of the main fracture initiation points in a bend-test. Tensile tests are also performed at a low strain rate and may be similarly influenced by micro-cracks. Tensile elongation and bend ductility are among the parameters used to classify the quality of wet welds according to the AWS D3.6 Specification for Underwater Welding. Micro-cracking may be less influential to Charpy impact toughness results. Very few features were observed on the Charpy fracture surfaces which could be attributed to micro-cracking. The Charpy test is performed at a very high strain rate where hydrogen induced cracking cannot occur.

The results of a quantitative survey of micro-cracking are presented in Figures 64 and 64. The survey was performed by visually inspecting fields in the optical microscope at a magnification of 250x on a polished and etched metallographic specimen. The number of fields which contained cracks was divided by the total number of fields inspected to produce a cracking percentage. At least one hundred fields were examined on each of two cross-sections from each of the test welds inspected. Micro-cracking is plotted as a function of porosity content in Figure 64. The amount of micro-cracking decreased as the volume percent porosity increased. Diffusible hydrogen may

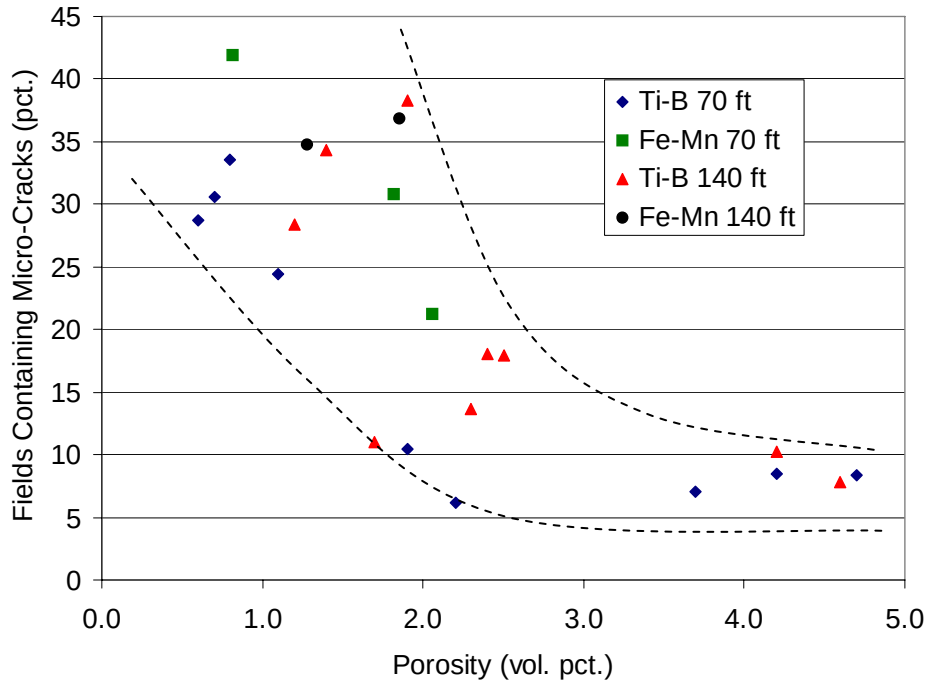

Figure 64: Percent of fields containing micro-cracks as a function of volume percent porosity.

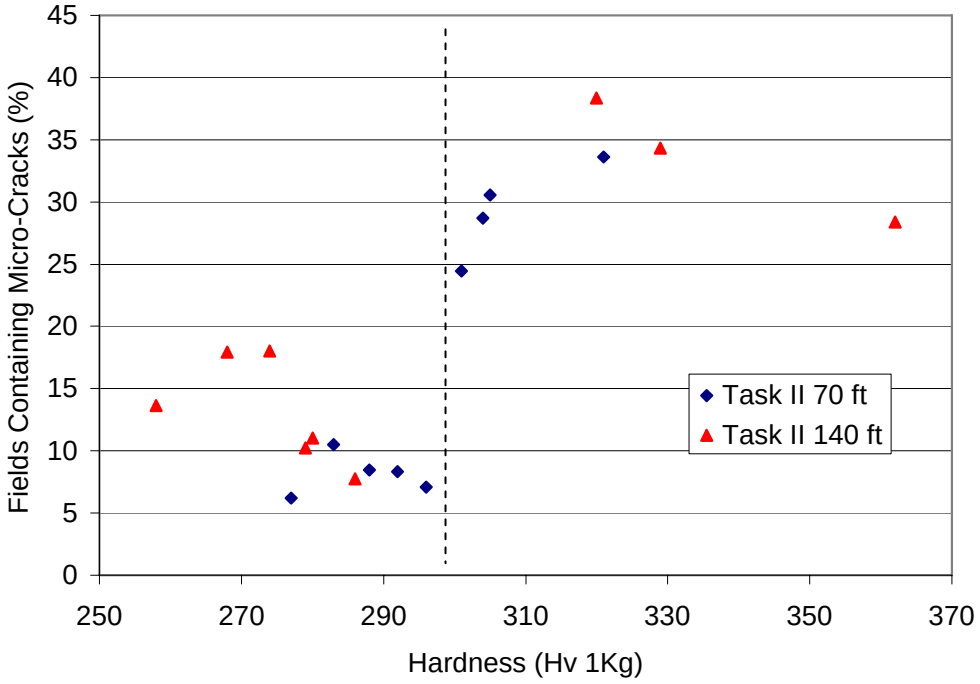

Figure 65: Percent of fields containing micro-cracks as a function of top bead hardness.

accumulate in pores, thereby reducing the diffusible hydrogen content and the occurrence of micro-cracking. The amount of micro-cracking is plotted as a function of as-deposited weld metal hardness in Figure 65. Occurrence of micro-cracking increases significantly when the as-deposited weld metal hardness exceeds approximately 300 HV. Hardness is limited to 325 HV for an AWS D3.6 Class A weld, which is meant to prevent gross hydrogen-induced cracking. It may be advantageous to limit hardness to below 300 HV to minimize micro-cracking. Further reductions in hardness below 300 HV do not completely eliminate micro-cracking, as seen in Figure 65. To eliminate micro-cracking it would be necessary to control the weld metal hydrogen content or control the cooling rate below the transformation temperatures. Reducing the cooling rate would allow more time for hydrogen to diffuse out of the weld metal before reaching temperatures at which hydrogen induced cracking can occur.

6.9 Radiography

Of the six V-groove welds which were produced in Task I with ferro-manganese additions, five were found acceptable to AWS D3.6 class B in terms of porosity by radiographic inspection. All of the V-groove welds produced in Task II with titanium-boron additions met the Class A requirements for radiographic inspection. Class A requirements are more stringent in terms of the number and size of pores which are allowed. The radiographic inspector indicated that Task II welds had less porosity density and fewer large pores than Task I welds. It was noted in section 6.3.2 that titanium-boron additions increased porosity. However, by selecting the lowest levels of titanium and boron necessary to produce the desired microstructure, it was possible to produce V-groove welds with low levels of porosity. The improved electrode performance with titanium-boron addition undoubtedly contributed to the ability of the diver/welders to produce a sound deposit. Radiography of the Task III V-groove welds with REM additions indicated higher levels of porosity than Task I or Task II welds,

which is consistent with the porosity measurements by metallography.

6.10 Mechanical Testing

The mechanical testing results are summarized in Tables 9, 12, and 15. The results are plotted in Figures 66-68 along with values for underwater wet welds reported in the literature. Each group of data points from the literature is from a specific electrode formulation. The data from Grubbs (1998) is from an electrode similar to the baseline electrode used in the present investigation with a low level of ferro-manganese addition and no additions of titanium, boron, or REM. A dashed line has been drawn through the Grubbs (1998) data to allow comparison of the present results to the baseline data.

Tensile strengths were in all cases higher for Task II welds with titanium-boron additions than for Task I welds with only ferro-manganese additions, as seen in Figure 66. Task II ultimate tensile strengths were brought up above 60 ksi at 200 and 300 feet, which is an improvement over the lower values from Task I. Tensile strengths of the Task II welds are comparable to the highest values reported in the literature. The increase in strength was due to a combination of grain refinement and solid solution strengthening, as discussed in section 6.5.3. Tensile strengths of the Task III welds with REM additions were lower than those of the Task II welds. The decrease in strength is due to an increase in reheated weld metal grain size and a reduction in solid solution strengthening compared to the Task II welds.

Tensile elongation for Task I welds at 70 and 140 ft (21 and 43 m) was greater than that of Task II or Task III welds. Task I welds had lower yield strengths than Task II and Task III welds at 70 and 140 ft. Steels with lower strength generally have greater ductility. In addition, the Task II weld at 70 ft had an average hardness approaching 300 HV and may have had more micro-cracking than the Task I weld at 70 ft. Low ductility in the Task III welds can be attributed to high levels of porosity in those welds at all depths. At 200 and 300 ft (61 and 91 m), Task II welds with titanium-boron additions

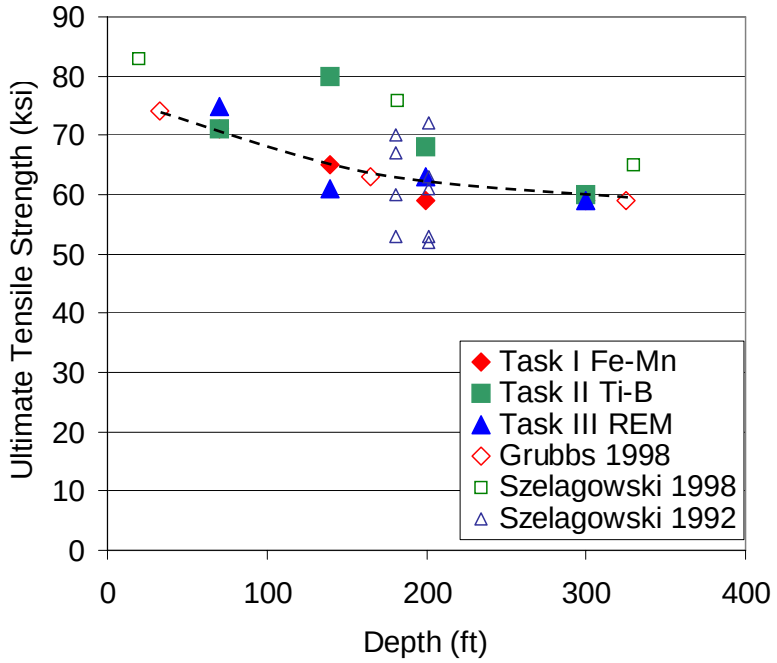

Figure 66: All-weld-metal tensile strength of Task IB and Task IIB steel welds plotted along with values from the literature for comparison.

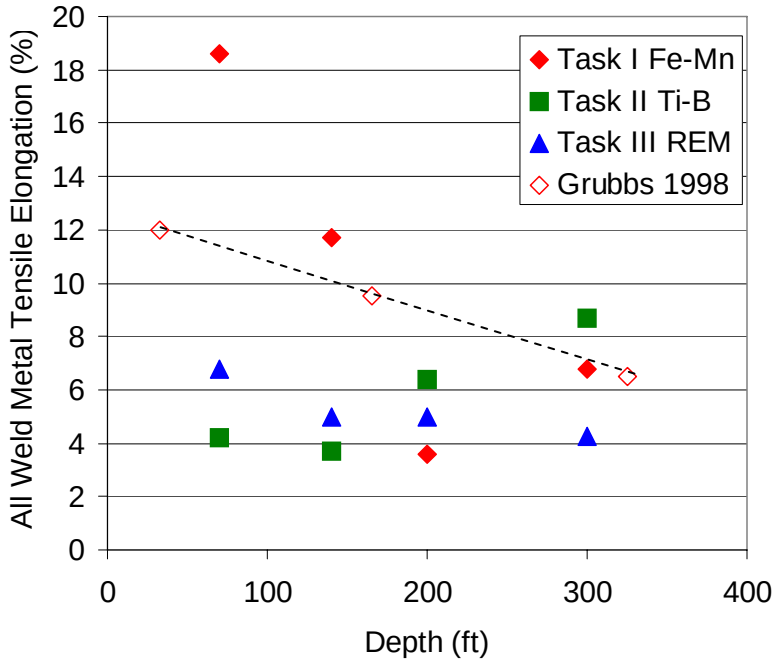

Figure 67: All-weld-metal tensile elongation of Task IB and Task IIB welds plotted along with values from the literature for comparison.

exhibited the greatest ductility. Low levels of porosity were indicated in those welds by radiographic inspection.

Task II Charpy impact toughness values were similar to Task I in most cases, but slightly less than Task I at 70 ft (21 m), as seen in Figure 68. The values from the present investigation are among the highest reported in the literature for a given depth. Fracture occurred by 90 to 100 pct. ductile void coalescence in all cases, indicating that the measured toughness values are on the upper shelf of the Charpy toughness vs. temperature curve.

Although significant microstructural refinement occurred in the Task II welds as a result of titanium-boron addition, little to no improvement in toughness was observed. Microstructural refinement is known to shift the ductile to brittle transition to lower temperatures, giving a greater margin of safety from brittle fracture. In the present investigation, impact toughness measurements were taken at one temperature; therefore, if any improvement in the transition temperature occurred, it would not be observed.

Upper shelf toughness is controlled by the concentration of defects, and is less sensitive to microstructure than the transition temperature. In surface welds, the upper shelf toughness is strongly influenced by the weld metal oxygen content, as indicated in Figure 13. The content of oxide inclusions in the weld metal increases with weld metal oxygen content, as indicated in Figure 3. Oxide inclusions act as sites for the initiation of ductile void coalescence. It is likely that the upper shelf toughness of underwater wet welds is limited by the high concentration of defects such as pores, oxide inclusions, and micro-cracks, and is not highly sensitive to microstructure. The low toughness values of the Task III welds can be attributed to high levels of porosity.

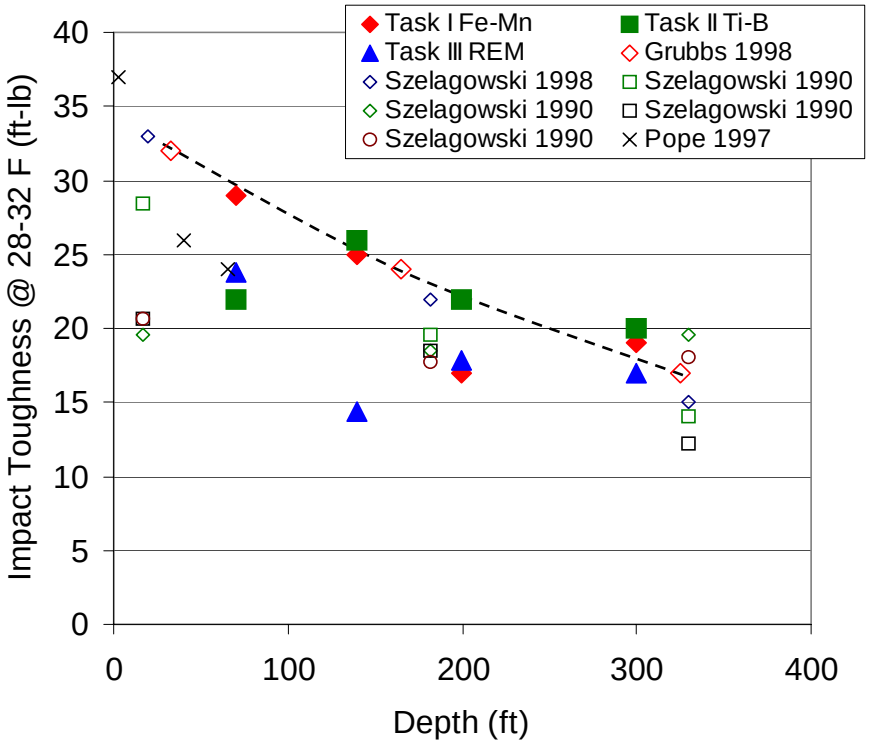

Figure 68: Charpy impact toughness of Task IB and Task IIB steel welds plotted along with values from the literature for comparison.

7 FINDINGS AND CONCLUSIONS

7.1 Findings

The following is a list of observations based on experiments with manganese, titanium, boron, and rare earth metal (REM) additions to underwater wet welding consumables.

1 High levels of ferro-manganese addition led to excessive slag fluidity and poor slag detachability. Addition of titanium and boron improved the behavior of consumables in terms of slag fluidity and detachability. Addition of rare earth metals (REM) did not significantly change the slag behavior and detachability. Poor slag behavior with high levels of ferro-manganese addition can be attributed to excessive quantities of manganese and iron oxide in the slag.

2 Addition of ferro-manganese alone failed to increase the weld metal manganese content due to the strongly oxidizing environment.

3 Increasing additions of ferro-titanium increased the recoveries of manganese and boron to the weld metal. It was possible to control the weld metal manganese content with addition of a stronger deoxidant, such as titanium, to the system.

4 Addition of REM reduced oxygen content and increased the recoveries of manganese and boron in preliminary tests at a depth of 1.5 ft (0.5 m), but high oxygen contents and low recoveries were observed at greater depths. Addition of REM increased the

exposure of the weld pool to oxygen and hydrogen at greater depths.

5 Formulations with titanium-boron additions produced the lowest levels of weld metal oxygen content. Titanium was more effective than manganese or REM as a deoxidant.

6 Switching from mechanical deposition to manual deposition of the test welds increased the recoveries of manganese and boron, decreased porosity, and reduced weld metal oxygen. The most likely explanation is decreased exposure of the weld pool to the water due to the ability of a skilled diver/welder to maintain a short arc length. It is possible that individual diver/welder skill may influence chemical composition and porosity in wet welds, particularly with micro-alloyed deposits.

7 Porosity decreased with increasing ferro-manganese addition, and increased with increasing additions of titanium, boron, and REM. One possible explanation is the effect of slag basicity on absorption of hydrogen into the weld pool, which determines the amount of hydrogen available to form porosity. Chemical analysis of selected slag samples revealed that porosity levels decreased with increasing slag basicity.

8 The proportion of acicular ferrite (AF) in the as-deposited microstructure was significantly increased through titanium-boron additions (60-80% AF) over welds with only ferro-manganese additions (10-20% AF). Microstructures high in acicular ferrite were also produced with formulations containing titanium, boron, and REM additions.

9 Significant microstructural refinement was observed in the reheated weld metal as a result of titanium-boron additions. A “memory effect” was observed, where additions which led to refinement of the as-deposited microstructure also led to refinement of

the reheated weld metal microstructure. Titanium-boron additions caused acicular ferrite to re-nucleate inside of the large prior-austenite grains in the coarse-grained heat affected zone. In the fine-grained heat affected zone, the finer as-deposited microstructure led to a finer reheated microstructure in welds containing titanium and boron. Welds with REM additions tended to have a more coarse microstructure in the reheated weld metal than those with titanium and boron alone due to decreased hardenability.

10 Yield strength exhibited a good correlation with the average ferrite grain size in the reheated weld metal, indicating that reheated weld metal microstructure has a significant influence on the mechanical properties of wet welds.

11 Radiographs of all four of the Task I V-groove welds with ferro-manganese additions met AWS D3.6 Class B requirements, while Task II V-groove welds with titanium-boron additions met the more stringent Class A requirements. Radiographic inspection revealed that Task II welds had less pore density and fewer large pores than the Task I welds. Task III welds with REM additions had the highest levels of porosity.

12 Ultimate tensile strength values were increased for the formulations with titanium-boron additions (60 to 80 ksi) over the Task I values (58 to 71 ksi) due to control over the manganese content.

13 Microstructural refinement due to titanium-boron additions did not significantly improve Charpy impact toughness values. Upper shelf toughness values for underwater wet welds are most likely determined by defect concentration rather than microstructure. Welds with REM additions exhibited low toughness values due to higher pore content.

7.2 Conclusions

The following is a list of general trends which were observed based on experiments with manganese, titanium, boron, and rare earth metal (REM) additions to underwater wet welding consumables.

1. The chemical composition of steel underwater wet welds can be controlled by addition a strong deoxidant, such as titanium, to the system.

2. Transfer of oxygen and hydrogen to the weld pool in underwater wet welds may be a function of the slag basicity. Neutral slags tend to have the lowest solubility for water vapor, and therefore, transfer the least amount of oxygen and hydrogen to the weld pool.

3. The proportion of acicular ferrite (AF) in the as-deposited microstructure was significantly increased through titanium-boron additions (60-80% AF) over welds with only ferro-manganese additions (10-20% AF) over the range of depths tested, 70 to 300 ft (21 to 91 m).

4. Additions of titanium and boron, which led to refinement of the as-deposited weld metal, also refined the ferrite grain size of the reheated weld metal through a memory effect.

5. Combined additions of titanium, boron, and manganese increased the tensile strength of the steel wet welds due to microstructural refinement and increased hardenability.

6. The degree of microstructural refinement and reduction in weld metal oxygen content produced by the titanium-boron additions did not significantly improve Charpy

impact toughness at 28 °F (-2 °C). Upper shelf toughness of wet welds is most likely controlled by the concentration of defects, such as pores, micro-cracks, and oxide inclusions.

8 RECOMMENDATIONS FOR FUTURE WORK

8.1 Effect of Slag Basicity on Porosity

Previous work by Pope (1995, 1996) and Medeiros (1997, 1998) along with other works discussed in section 2.1.2 indicate that slag composition, and specifically slag basicity, can influence the absorption of hydrogen into the weld pool. Based on the work of Ando and Asahina (1983) and Suga (1986) as well as present investigation, it can be concluded that porosity in underwater wet welds is caused by hydrogen. In the present investigation, the ferro-alloy additions influenced the amount of porosity in the weld metal. The effect may be due to changes in slag composition due to oxidation of the ferro-alloy additions and partitioning of those elements to the slag. Results of chemical analyses of slags presented in section 6.4 indicate that higher slag basicity is associated with lower levels of porosity. Further investigation is necessary to confirm this effect.

If it is possible to limit the solubility of water vapor in the slag by manipulating the slag basicity, then both the oxygen and hydrogen content of the weld metal can be reduced at the same time. There are many possible ways in which the slag basicity could be altered. One way would be to add magnesium as a deoxidant, as was done by Surian (1997) for dry welds. The magnesium would be oxidized and partition to the slag as MgO, which would increase slag basicity. Further investigation into the effects of slag basicity may lead to significant improvements in the quality of underwater wet welds through the development of consumables which minimize the transfer of oxygen and hydrogen to the weld pool.

8.2 Improving Electrode Performance for Wet Welding at Greater Depths

In the present investigation it was revealed that the manipulation of the electrode, such as mechanical versus manual deposition, can have a significant effect on the chemical composition and porosity content of the weld metal. As the pressure increases at greater depths underwater, it becomes more difficult for a diver/welder to produce a sound weld. If an addition to the coating causes the electrode to behave poorly in terms of arc stability or slag behavior, the weld pool will be exposed to greater amounts of oxygen and hydrogen which can overwhelm the intended positive effect of the addition on weld pool composition. The effects of electrode behavior on wet weld quality become more acute at greater depths. As an aside to the present investigation, fluorides were added to the electrode coating, as suggested by Medeiros (1997) in the "Future Work" section of his thesis. The electrode behavior was degraded to such an extent that it was not possible to produce a sound weld at depths greater than 30 ft (9.1 m).

An investigation which is specifically oriented toward improving arc stability and slag behavior of electrodes at greater depths has the potential to dramatically improve wet weld quality. With a greater understanding of what factors influence electrode performance, it may be possible to experiment with a wider variety of additions, such as fluorides.

REFERENCES

Ahlblom, B. 1982. Oxygen and its Role in Determining Weld Metal Microstructure and Toughness – A State of the Art Review. Doc. No. IX-1322-84. International Institute of Welding. Reprinted in ASM Handbook Vol. 6, ASM International.

Ando, S., Asahani, T. 1983. A Study on the Metallurgical Properties of Steel Welds with Underwater Gravity Welding. Underwater Welding: Proceedings of the International Conference held at Trondheim, Norway. International Institute of Welding, Pergamon Press.

AWS. 1989. ANSI/AWS D3.6-89 Specification for Underwater Welding. American Welding Society, Miami FL.

Bodsworth, C., Bell, H. B. 1972. Physical Chemistry of Iron and Steel Manufacture. Longman Group Ltd. London.

Blackledge, R. 1998. Case Studies: Underwater Welding Projects. Underwater. (Fall)

Couch, J. 1997. Platform Structural Upgrades Based on Wet Welding. Underwater. (Spring)

Cheveriat, P. F., Kim, G. S., Shah, S., Indacochea, J. E. 1987. Low Carbon Steel Weld Metal Microstructures: The Role of Oxygen and Manganese. Journal of materials Engineering. 9 (3): 253-267.

Childs, W. 1991. Underwater Wet Welding for Pressure Vessel Repairs. EPRI Journal. (December): 36-37.

Efimenko, N. G. 1980. The Use of Rare Earth Metals in the Coatings of Welding Electrodes. Welding Production. 27 (7): 47-49.

Efimenko, N. G., Kalin, N. A. 1978. The Deoxidizing Ability of Rare Earth Metals in Comparison With Deoxidizing Agents. Svar. Proiz. (10): 1-2

Evans, G. M. 1980. Effect of Manganese on the Microstructure and Properties of All-Weld-Metal Deposits. Welding Journal 69 (3): 67s-75s.

Evans, G. 1992. The Effect of Titanium in SMA C-Mn Steel, Multipass Deposits. Welding Journal 71 (12): 447s-454s.

Evans, G. 1993. The Effect of Titanium in Manganese-Containing SMA Weld Deposits. Welding Journal 72 (3): 123s-133s.

Evans, G. 1996. Microstructure and Properties of Ferritic Steel Welds Containing Ti and B. Welding Journal 72 (8): 251s-260s.

Grubbs, C. E., Reynolds, T. J. 1998. State-of-the-Art Underwater Wet Welding. World Oil. (July): 79-83.

Grubbs, C., Reynolds, T. 1999. Underwater Wet Welding: Research leading to improved Techniques. Underwater. (Winter): 52-55.

Ibarra, S., Grubbs, C., Olson, D. 1987. The Nature of metallurgical Reactions in Underwater Wet Welding. 19th Annual Offshore Technology Conference Report OTC5388. Houston.

IIW. 1988. Guide to Light Microscope Examination of Ferritic Steel Weld Metals. IIW Doc. No. IX-1533-88. International Institute of Welding, American Council. AWS, Miami, FL.

Koukabi, A. H., North, T. H., Bell, H. B. 1978. Flux Formulation, Sulphur, Oxygen, and Rare Earth Additions in Submerged Arc Welding. Proceedings, Trends in Steels and Consumables for Welding. London: 281-297.

Liu, S., Olson, D. L., Ibarra, S. 1994. Electrode Formulation to Reduce Weld Metal Hydrogen and Porosity. Proceedings: 13th Offshore Mechanics and Arctic Engineering Conference. Copenhagen, Denmark. American Society of Mechanical Engineers.

Medeiros, R. 1997 Effect of Oxidizing Electrodes and Polarity on Hydrogen Mitigation in Underwater Wet Welding. Thesis. Colorado School of Mines.

Medeiros, R., Liu, S. 1998. A Predictive Electrochemical Model for Weld Metal Hydrogen Pickup in Underwater Wet Welds. Journal of Offshore Mechanics and Arctic Engineering. 120 (4): 243-248.

Oh, D., Olson, D., Frost, R. 1990. Influence of Boron and Titanium on Low-Carbon Steel Weld Metal. Welding Journal 69 (4): 151s-158s.

Onsoien, M. I., Liu, S., Olson, D. L. 1996. Shielding Gas Oxygen Equivalent in Weld Metal Microstructure Optimization. Welding Journal 75 (7): 216s-224s.

Pope, A. M., Teixeira, C. G., Paes, M. P., dos Santos, V. R., Ros, D., Domingues, J. R., 1997. Influence of Water Depth on Microstructure and Mechanical Properties of Wet Welds. Proceedings: 16th Offshore Mechanics and Arctic Engineering Conference. American Society of Mechanical Engineers.

Pope, A. M. 1995. Oxygen and Hydrogen Control in Shielded Metal Underwater Wet Welding. Thesis. Colorado School of Mines.

Pope, A. M., Liu, S., 1996. Hydrogen Content of Underwater Wet Welds Deposited by Rutile and Oxidizing Electrodes. Proceedings: 15th Offshore Mechanics and Arctic Engineering Conference. American Society of Mechanical Engineers. Vol. III pp 85-92.

Pokhodnya, I. K., Korsun, A. O., Meshkov, Y. Y. 1986. Effects of the Segregation of Silicon and Manganese on the Formation of Acicular Ferrite in the Structure of a Weld. Automatic Welding. (September): 13-16.

Rissone, N., Bott, I., Jorge, J., Corvalan, P., Surian, C. 1997. ANSI/ AWS A5.1-91 E6013 Rutile Electrodes: The Effect of Wollastonite. Welding Journal. 76 (11): 498s-507s.

Sanchez-Osio, A. 1994. The Influence of Consumable Composition and Solidification on Inclusion Formation and Growth in Low Carbon Steel Underwater Wet Welds. Thesis. Colorado School of Mines.

Sanchez-Osio, A., Liu, S., Ibarra, S. 1995. Designing Shielded Metal Arc Consumables for Underwater Wet Welding in Offshore Applications. Journal of Offshore Mechanics and Arctic Engineering 117 (3): 212-20.

Shiliang, W., Weiping, H., Bogang, T. 1986. Improving the Toughness of Weld Metal by Adding Rare Earth Elements. Welding International. (3): 284-287.

Slutskaya, T. M., Asnis, A. E., Tyurin, A. Y. 1978. The Properties of Wire Alloyed With Crium and Yttrium Used for CO2 Welding. Automatic Welding. 31 (2): 54-56

Snyder, J. P., Pense, A. W. 1982 The Effects of Titanium on Submerged Arc Weld Metal. Welding Journal. 61 (7): 201s-211s.

Suga, Y., Hasui, A., 1986. On Formation of Porosity in Underwater Wet Weld Metal (The First Report). Transactions of the Japan Welding Society. 17 (1): 58-64.

Suga, Y. 1987. Blowhole Formation by Hydrogen. Transactions of the Japan Welding Society. 18 (1): 61-68.

Surian, E. 1997. ANSI/ AWS E7024 SMAW Electrodes: The Effect of Coating Magnesium Additions. Welding Journal. 76(10): 404s-411s.

Surian, E., Boniszewski, T. 1992. Effect of Manganese and Type of Current on the Properties and Microstructure of All Weld metal Deposited with E7016-1 Electrodes. Welding Journal 71 (9): 348s-363s.

Szelagowski, P. 1998. Wet Welding as a "Serious" Repair Procedure?. Journal of Offshore Mechanics and Arctic Engineering. 120(8): 191-196.

Szelagowski, P., Pachniuk, I., Stuhff, H. 1992. Wet Welding for Platform Repair. Proceedings of the Second International Offshore and Polar Engineering Conference. San Francisco. International Society of Offshore and Polar Engineers. 208-215.

Szelagowski, P., Stuhff, H., Schnafstall, H. G., Blight, J., Pachniuk, I. 1990. Developments in Manual Wet SMA Welding. Proceedings: 22nd Annual Offshore Technology Conference. Houston. 143-150.

Terashima, H., Tsuboi, J. 1982. Submerged Arc Flux for Low Oxygen and Hydrogen Weld Metal. Metal Construction. (December): 648-654.

Tsuboi, J., Terashima, H. 1983. Review of Strength and Toughness of Ti and Ti-B Microalloyed Deposits. Welding in the World 21 (11/12): 304-316.

Tuliani, S. S., Boniszewski, T., Eaton, N. F. 1969. Notch Toughness of Commercial Submerged Arc Weld Metal. Welding and Metal Fabrication. August: 327-339.

Turkdogan, E. T. 1983. Physiochemical Properties of Molten Slags and Glasses. The Metals Society. London.

Wood, B. J., Bruce, W. A., Boyles, L. G. 1990. Characteristics of an Underwater Wet Repair Weld Made at -560 ft. Proceedings: 22nd Annual Offshore Technology Conference. Houston, Texas pp151-159.

Zhang, Z., Farrar, R. A. 1997. Influence of Mn and Ni on the Microstructure and Toughness of C-Mn-Ni Weld Metals. Welding Journal. 76 (5): 183s-196s.